COPPE
Instituto Alberto Luiz Coimbra de Pós-Graduação e Pesquisa de Engenharia
UFRJ

CFD ANALYSIS OF A DIESEL PARTICULATE FILTER PERFORMANCE USING BIODIESEL

Felipe Féres Ferreira

Dissertação de Mestrado apresentada ao Programa de Pós-graduação em Engenharia Mecânica, COPPE, da Universidade Federal do Rio de Janeiro, como parte dos requisitos necessários à obtenção do título de Mestre em Engenharia Mecânica.

Orientador: Gustavo Rabello dos Anjos

Rio de Janeiro
Julho de 2023

CFD ANALYSIS OF A DIESEL PARTICULATE FILTER PERFORMANCE USING BIODIESEL

Felipe Féres Ferreira

DISSERTAÇÃO SUBMETIDA AO CORPO DOCENTE DO INSTITUTO ALBERTO LUIZ COIMBRA DE PÓS-GRADUAÇÃO E PESQUISA DE ENGENHARIA DA UNIVERSIDADE FEDERAL DO RIO DE JANEIRO COMO PARTE DOS REQUISITOS NECESSÁRIOS PARA A OBTENÇÃO DO GRAU DE MESTRE EM CIÊNCIAS EM ENGENHARIA MECÂNICA.

Orientador: Gustavo Rabello dos Anjos

Aprovada por: Prof. Gustavo Rabello dos Anjos
Prof. Daniel Onofre de Almeida Cruz
Prof. Tânia Suaiden Klein

RIO DE JANEIRO, RJ – BRASIL
JULHO DE 2023

Féres Ferreira, Felipe

CFD analysis of a Diesel Particulate Filter performance using Biodiesel/Felipe Féres Ferreira. – Rio de Janeiro: UFRJ/COPPE, 2023.

XIII, 79 p.: il.; 29, 7cm.

Orientador: Gustavo Rabello dos Anjos

Dissertação (mestrado) – UFRJ/COPPE/Programa de Engenharia Mecânica, 2023.

Referências Bibliográficas: p. 71 – 74.

1. CFD. 2. Diesel Particulate Filter. 3. Biodiesel. I. Rabello dos Anjos, Gustavo. II. Universidade Federal do Rio de Janeiro, COPPE, Programa de Engenharia Mecânica. III. Título.

Dedico este trabalho a minha filha Alicia.

Agradecimentos

Primeiramente, gostaria de agradecer ao Programa de Recursos Humanos da Agência Nacional do Petróleo, Gás Natural e Biocombustíveis - PRH/ANP pelo apoio financeiro fornecido a essa pesquisa.

Também gostaria de agradecer ao meu orientador Gustavo Rabello que sempre se mostrou disponível para me ajudar e guiar da melhor forma possível durante esta jornada, sendo essencial para que eu adquirisse a paixão por pesquisa que possuo hoje.

Por fim, gostaria de agradecer aos meus pais, Antônio Carlos e Andrea Maria, e minha irmã, Carolina, que sempre foram meu porto seguro. Além de agradecer meus amigos que também sempre estão presentes para mim, nos momentos bons ou ruins.

Resumo da Dissertação apresentada à COPPE/UFRJ como parte dos requisitos necessários para a obtenção do grau de Mestre em Ciências (M.Sc.)

ANÁLISE CFD DO DESEMPENHO DE UM FILTRO DE PARTICULADO DIESEL USANDO BIODIESEL

Felipe Féres Ferreira

Julho/2023

Orientador: Gustavo Rabello dos Anjos

Programa: Engenharia Mecânica

Atualmente, dois assuntos relacionados a veículos têm sido amplamente discutidos: o uso de biocombustíveis e a poluição do ar. No contexto específico de veículos com motores a diesel, a demanda por biodiesel vem aumentando, trazendo diversos benefícios ambientais. No entanto, apesar de o biodiesel causar menos poluição do ar do que o diesel tradicional, ele ainda polui o ar de uma maneira que não é aceita pelas leis atuais. Para lidar com esse problema, é utilizado um dispositivo chamado Diesel Particulate Filter, ou apenas DPF. Neste trabalho, tem-se como objetivo descrever o escoamento multifásico, composto por ar e partículas geradas pela combustão do biodiesel, dentro desse dispositivo. Assim, é apresentada uma metodologia capaz de simular numericamente esse tipo de escoamento. Essa metodologia utiliza uma abordagem Euleriana-Lagrangiana para descrever o escoamento multifásico e também utiliza a equação de Forchheimer para modelar o escoamento dentro de uma região porosa existente no interior do DPF. As equações que descrevem o escoamento de ar são resolvidas numericamente utilizando o Método dos Elementos Finitos, enquanto as equações de movimento das partículas são resolvidas pelo método Runge-Kutta de 4a ordem. Um código computacional baseado nessa metodologia foi desenvolvido e passou por um processo de verificação antes de ser usado para simular esse problema. Em seguida, o código foi utilizado para simular o escoamento no DPF, e os resultados foram comparados com aqueles encontrados na literatura, possibilitando verificar que a metodologia apresentada é realmente capaz de simular corretamente o escoamento de ar com partículas de biodiesel dentro de um DPF.

Abstract of Dissertation presented to COPPE/UFRJ as a partial fulfillment of the requirements for the degree of Master of Science (M.Sc.)

CFD ANALYSIS OF A DIESEL PARTICULATE FILTER PERFORMANCE USING BIODIESEL

Felipe Féres Ferreira

July/2023

Advisor: Gustavo Rabello dos Anjos

Department: Mechanical Engineering

Nowadays, two topics about vehicles that have been discussed a lot are the use of biofuels and the air pollution. In the specific context of vehicles with diesel engines, the biodiesel demand has been increasing, which brings a lot of environmental benefits. However, even though biodiesel causes less air pollution than traditional diesel, it still pollutes the air in a way that is not accepted by the current laws. Then, a device called Diesel Particulate Filter, or just DPF, is used to mitigate this problem. In this work, it is aimed to describe the multiphase flow, constituted by air and particles generated by biodiesel combustion, inside this device. Then, it is presented a methodology able to numerically simulate this type of flow. This methodology has used an Eulerian-Lagrangian approach to describe the multiphase flow and it also has used the Forchheimer equation to model the flow inside a porous region that exists inside the DPF. The equations that describe the air flow are numerically solved by using the Finite Element Method while the particulates' motion equations are solved by the 4th order Runge-Kutta method. A computational code based on this methodology was developed and a verification process was made on it before it was used to simulate this problem. After that, the code was used to simulate the flow in the DPF and the results were compared with the ones found in the literature, making it possible to verify that the presented methodology is really capable to simulate correctly the airflow with biodiesel particulates inside a DPF.

Contents

List of Figures **x**

List of Tables **xiii**

1 Introduction **1**

2 Literature Review **3**

2.1 Biodiesel 3

2.2 Diesel Particulate Filter 4

2.3 Porous Medium 5

2.4 Particle-Laden Flows 6

2.5 Numerical Methods 7

2.6 CFD applied to DPF 9

3 Mathematical Model **13**

3.1 Continuous Phase 13

3.2 Porous Region 14

3.3 Dispersed Phase 15

4 Numerical Methods **19**

4.1 Finite Element Method 19

4.1.1 Weak Form 19

4.1.2 Galerkin Method 22

4.1.3 Mesh Element 26

4.1.4 Semi-Lagrangian Method 28

4.2 Runge-Kutta Method 31

5 Code Verification **33**

5.1 Two-Dimensional 33

5.1.1 Plane Poiseuille Flow 33

5.1.2 Lid Driven Flow 34

5.1.3 Flow over Porous Region 37

5.2 Three-Dimensional . . . 39
5.2.1 Hagen-Poiseuille . . . 39
5.2.2 Square Duct with a Moving Top Wall . . . 40
5.2.3 Flow over Porous Region . . . 42

6 DPF Simulations **44**
6.1 Two Dimensional . . . 44
6.1.1 Case Set-Up . . . 44
6.1.2 Case 1: Air flow . . . 45
6.1.3 Case 2: Air with particulates . . . 50
6.2 Three Dimensional . . . 56
6.2.1 Case Set-Up . . . 56
6.2.2 Case 3: Airflow and channels with 50% of its original length . 57
6.2.3 Case 4: Airflow and channels with 20% of its original length . 63

7 Conclusions **69**

References **71**

A Other Figures **75**

List of Figures

2.1 Schematic representation of DPF's channels. 5

4.1 Elements' representation. 27
4.2 Schematic representation of the searching procedure used in the semi-Lagrangian method to find the element containing the departed node position. 30

5.1 Schematic representation of Plane Poiseuille Flow case. 34
5.2 Comparison between simulation and analytical results for Plane Poiseuille Flow case. 35
5.3 Schematic representation of Lid Driven Flow case. 35
5.4 Results obtained by simulations and literature for $Re = 10$ for the Lid Driven Flow case. 36
5.5 Results obtained by simulations and literature for $Re = 100$ for the Lid Driven Flow case. 36
5.6 Results obtained by simulations and literature for $Re = 1000$ for the Lid Driven Flow case. 37
5.7 Schematic representation of the flow over porous region problem. . . . 37
5.8 Results obtained by simulations and literature for the flow over porous region problem. 38
5.9 Schematic representation of the Hagen-Poiseuille case. 39
5.10 Comparison between simulation and analytical results for Hagen-Poiseuille case. 40
5.11 Schematic representation of the square duct with a moving top wall problem. 41
5.12 Comparison between simulation and reference results for the square duct with moving top wall problem. 42
5.13 Results obtained by simulations and literature for the three-dimensional flow over porous region problem. 43

6.1 Two-Dimensional DPF Model. 45
6.2 Mesh at the inlet of the DPF in Case 1. 46

6.3 Mesh at the outlet of the DPF in Case 1. 47
6.4 Horizontal velocity at DPF's inlet in Case 1. 47
6.5 Horizontal velocity at DPF's outlet in Case 1. 48
6.6 Pressure at DPF's inlet in Case 1. 48
6.7 Pressure at DPF's outlet in Case 1. 48
6.8 Axial velocity along the inlet and outlet channels at Case 1. 49
6.9 Wall Velocity along the channel at Case 1. 50
6.10 Mesh at the inlet of the DPF in Case 2. 51
6.11 Mesh at the outlet of the DPF in Case 2. 52
6.12 Horizontal velocity at DPF's inlet in Case 2. 52
6.13 Horizontal velocity at DPF's outlet in Case 2. 52
6.14 Pressure at DPF's inlet in Case 2. 53
6.15 Pressure at DPF's outlet in Case 2. 53
6.16 Normalized flowrate through the porous wall along the channel at Case 2. 54
6.17 Horizontal velocity at DPF's inlet and particulates trapped in the porous wall at Case 2. 54
6.18 Horizontal velocity at DPF's outlet with particulates trapped in the porous wall at Case 2. 55
6.19 Trapped particulates concentration along the channel at Case 2. . . . 55
6.20 Three-Dimensional DPF Model. 56
6.21 Horizontal velocity along the inlet and outlet channels results obtained using three different meshes. 58
6.22 Velocity in x_2 direction in the porous wall at different distances from the channels centers. 59
6.23 Velocity in x_3 direction in the porous wall at different x_2 values. . . . 60
6.24 Horizontal velocity field at the DPF's inlet plotted in the $x_1 - x_2$ plane. 61
6.25 Horizontal velocity field at the DPF's outlet plotted in the $x_1 - x_2$ plane. 61
6.26 Horizontal velocity field at the DPF's inlet plotted in the $x_1 - x_3$ plane. 61
6.27 Horizontal velocity field at the DPF's outlet plotted in the $x_1 - x_3$ plane. 62
6.28 Pressure field at the DPF's inlet plotted in the $x_1 - x_2$ plane. 62
6.29 Pressure field at the DPF's outlet plotted in the $x_1 - x_2$ plane. 62
6.30 Pressure field at the DPF's inlet plotted in the $x_1 - x_3$ plane. 63
6.31 Pressure field at the DPF's outlet plotted in the $x_1 - x_3$ plane. 63
6.32 Horizontal velocity along the inlet and outlet channels results obtained using three different meshes. 64

6.33 Velocity in x_2 direction in the porous wall at different distances from the channels centers. 66
6.34 Velocity in x_3 direction in the porous wall at different x_2 values. . . . 67
6.35 Horizontal velocity field plotted in the $x_1 - x_2$ plane. 67
6.36 Horizontal velocity field plotted in the $x_1 - x_3$ plane. 68
6.37 Pressure field plotted in the $x_1 - x_2$ plane. 68
6.38 Pressure field plotted in the $x_1 - x_3$ plane. 68

A.1 Horizontal velocity at DPF's inlet in Case 1 obtained with the quadratic mesh. 75
A.2 Horizontal velocity at DPF's outlet in Case 1 obtained with the quadratic mesh. 75
A.3 Pressure at DPF's inlet in Case 1 with the quadratic mesh. 76
A.4 Pressure at DPF's outlet in Case 1 with the quadratic mesh. 76
A.5 Horizontal velocity at DPF's inlet in Case 2 using quadratic mesh. . . 76
A.6 Horizontal velocity at DPF's outlet in Case 2 using quadratic mesh. . 77
A.7 Pressure at DPF's inlet in Case 2 using quadratic mesh. 77
A.8 Pressure at DPF's outlet in Case 2 using quadratic mesh. 77
A.9 Horizontal Velocity at DPF's inlet in Case 3 obtained with Mesh 1. . 77
A.10 Horizontal Velocity at DPF's outlet in Case 3 obtained with Mesh 1. 77
A.11 Pressure at DPF's inlet in Case 3 obtained with Mesh 1. 77
A.12 Pressure at DPF's outlet in Case 3 obtained with Mesh 1. 78
A.13 Horizontal Velocity at DPF's inlet in Case 3 obtained with Mesh 2. . 78
A.14 Horizontal Velocity at DPF's outlet in Case 3 obtained with Mesh 2. 78
A.15 Pressure at DPF's inlet in Case 3 obtained with Mesh 2. 79
A.16 Pressure at DPF's outlet in Case 3 obtained with Mesh 2. 79
A.17 Horizontal Velocity at DPF in Case 4 obtained with Mesh 1. 79
A.18 Pressure at DPF in Case 4 obtained with Mesh 1. 79
A.19 Horizontal Velocity at DPF in Case 4 obtained with Mesh 2. 79
A.20 Pressure at DPF in Case 4 obtained with Mesh 2. 79

List of Tables

5.1 Boundary Conditions of the Plane Poiseuille problem. 33
5.2 Boundary Conditions of the Lid Driven Flow problem. 35
5.3 Boundary Conditions of the flow over a porous region problem. 38
5.4 Boundary Conditions of the Hagen-Poiseuille problem. 39
5.5 Boundary Conditions of the Square Duct with a Moving Top Wall problem. 41

6.1 Boundary Conditions of the two-dimensional DPF model. 45
6.2 Parameters used in the simulation of Case 1. 46
6.3 Parameters used in the simulation of Case 2. 51
6.4 Boundary Conditions of the three-dimensional DPF model. 57
6.5 Details of the meshes used in Case 3. 57
6.6 Details of the meshes used in Case 4. 63

Chapter 1

Introduction

The transportation sector has been a very important area for humanity for some time now. In this scenario, internal combustion engines play a major role, as they are currently the main source of energy used in it. Then, it is possible to highlight the diesel engine, a combustion engine that is widely used by vehicles nowadays due to its advantages like efficiency and power output. However, one of its main problems is its air pollution emissions. This problem can be mitigated by the use of a device named Diesel Particulate Filter, or just DPF.

Moreover, another great problem related to the diesel engine is the high petroleum consumption problem, which has led to an increase in the demand for biofuels. In this specific diesel engine case, some efforts have been made for the partial or total replacement of traditional diesel by biodiesel. Therefore, since the DPF usually has been used along with diesel fueled engines, it is also important to study how it works with biodiesel.

Nowadays, since the computational capacity available has increased considerably in recent years, a very important tool for engineers is numerical simulation. These simulations have made it possible to solve complex cases that have no analytical solutions in an efficient way. There is an important branch of fluid mechanics that uses numerical simulations to solve fluid flows. This area is named Computational Fluid Dynamics, or just CFD.

Then, this work aims at developing a methodology to simulate numerically the multiphase flow inside the DPF, including the filter which is made of a porous material, and to use this methodology to develop a computational code to run some DPF cases. The DPF's flow simulation will make it possible to study it in more detail.

The structure of this thesis is organized as follows. After a brief introduction presented in this chapter, it is presented a literature review about biodiesel, DPF, numerical methods, and the physics present in this case. After that, it is shown the governing equations of this problem. Then, the numerical methods used in this

work are presented and applied to the governing equations.

After applying the numerical methods, the in-house developed code is used to run cases that are well established in the literature in order to ensure that this code is reliable. Therefore, it is used to simulate DPF flows cases. The results that were obtained for DPF cases are compared with those found in the literature to confirm the presented methodology's validity. Finally, some conclusions can be drawn and suggestions for future work can be made.

This research aims at presenting a valid methodology that can be used to study the flow inside a DPF used in vehicles that use biodiesel, making it possible to study in detail this flow and, then, make some further improvements to it. Moreover, it is expected that this methodology can be further used in different scenarios.

Chapter 2

Literature Review

2.1 Biodiesel

Biodiesel is a renewable fuel that is produced from vegetable oils, animal fats, or other materials consisting mainly of triacylglycerols. Chemically, biodiesel is a mono-alkyl ester, most commonly a methyl ester, and it is an alternative fuel that is used in compression-ignition engines [1].

Biodiesel was first used in 1893 when Rudolf Diesel, the compression-ignition engine's inventor, used peanut oil to fuel his engine. After that, vegetable oils were used as fuels until the 1920s when fossil-based diesel became more popular offering cheaper prices and higher availability [2].

So, the first feedstocks were vegetable oils. However, even though they still are the main feedstocks, nowadays many other materials are used to produce this fuel, like used cooking oils, grease, and animal fats [1].

This biofuel has properties similar to regular diesel which is made of petroleum. This fact makes it possible to use it with little or no engine modification. In addition, the biodiesel can be used in its pure form or blended in any proportion with regular diesel [3].

In order to increase its usage, many countries have made mandatory the use of biodiesel in commercial diesel [4]. In Brazil, for example, there is a law about that since 2008, when it was established that it should have 2% of biodiesel in the fuel. Since then, this percentage has increased [5].

There are some important disadvantages in its use that have been affecting its popularity. One of them is the high prices of the feedstock. Feedstock acquisition accounts for over 80% of the production cost, which makes it difficult to make it economically viable. A possible solution for that is the use of alternative feedstocks [6].

Another important problem of biodiesel is the higher NO_X exhaust emission that

occurs in some cases [6]. The NO_X emission is a big problem since it causes direct and indirect impacts on people's health [7]. This problem can be mitigated by an engine and/or fuel modifications [8].

There are also other disadvantages of biodiesel like inferior storage, inferior oxidative stability, inferior low-temperature operability, and lower volumetric energy content. These can be mitigated through cold flow improver, antioxidant additives, blending biodiesel with petrodiesel, and/or reducing storage time [6].

On the other hand, there are a lot of advantages to the use of this biofuel. The main advantages are environmental impact reduction since it derives from renewable and domestic feedstock, it is biodegradable and, despite the higher emission of NO_X, it has a lower overall exhaust emission. There are also advantages not related to environmental impact reduction like its inherent lubricity, low toxicity, and superior flash point [6].

2.2 Diesel Particulate Filter

Nowadays, because of the increasing pollution concerns, there are stringent emission regulations for diesel engine's vehicles. So, these emission regulations are making the use of Diesel Particulate Filters mandatory, since it is proven that until now this device is the only one able to control the particulate emissions in an effective way [9].

The Diesel Particulate Filter, also known as DPF, is a device used to mitigate the emissions of a diesel engine it has two functions: to trap and retain the particulate matter and to get safely rid of this particulate matter, avoiding problems in the engine operation [10].

There are different configurations for DPF available, but the most widely used configuration is the wall-flow type. This type of construction has a honeycomb shape with parallel channels which are plugged alternately at each end. Besides that, the walls are made of a porous filter where the particulates are retained [11].

Figure 2.1 presents a schematic figure of the structure of the channels inside the DPF. In this figure, it had been only shown a sample of nine channels for simplicity reasons. On the left, it is shown a front view of the device's channels while it is shown an inside view from them on the right.

In the wall-flow DPF, the exhausted air enters in the channel and, since this channel is closed by a plugged end, the air is forced to go through the porous walls, moving to another channel where the inlet is closed and the outlet is open, making it possible for the filtered air to escape to the atmosphere. This situation is also represented in the Figure 2.1.

As mentioned before, apart from the filtration function of this device, it has also

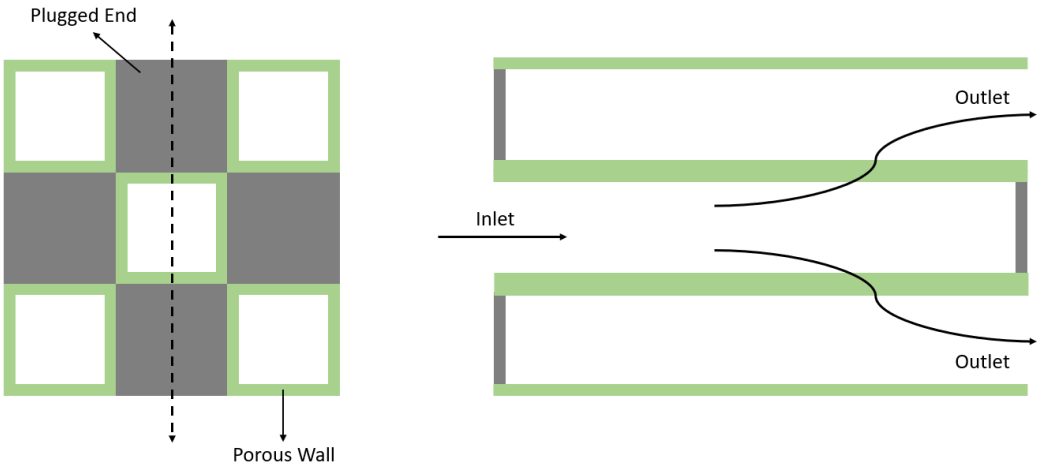

Figure 2.1: Schematic representation of DPF's channels.

the function of eliminating the particulates that have been trapped. So, to achieve this goal, a regeneration process is usually carried out.

Regeneration is performed by burning the particulates that are trapped in the filter. To burn them, it is necessary sufficient oxygen and a minimum heat quantity. The oxygen is not a problem because there is plenty of them in the exhausted air. However, the heat quantity can be a problem, being necessary to ensure that the device's temperature is at least a minimum value that makes possible to incinerate the particulates [10].

There are two ways to achieve regeneration: passive and active. Passive regeneration means that the burning process is achieved without any auxiliary system. On the other hand, active regeneration occurs when auxiliary means are needed to reach the minimum heat required for the process. A combination of these two types of regeneration is also used in many applications [10].

2.3 Porous Medium

The study of the flow behavior through a porous medium is an important field of fluids mechanics since there are many industrial processes related to that, like filtration and oil extraction through porous rock. To describe this flow, the usual Navier-Stokes equations can be used. However, to do that it would be necessary to describe correctly the geometry of the porous walls which are bounding the flow, but this description probably would be very difficult to do since these geometries usually are very complex [12].

Then, since it usually is very difficult to calculate directly the flow in the porous medium, it was necessary to model this region. The model with the simplest relation between velocity and pressure is the model known as Darcy Law. The Darcy Law

is summarized by the following Eq. 2.1 [13].

$$\mathbf{u_s} = -\frac{K}{\mu}\nabla P \tag{2.1}$$

where $\mathbf{u_p}$ is the superficial velocity vector, K is the permeability coefficient of the porous medium, μ is the dynamic viscosity and P is the pressure.

The Darcy Law provides good results for flows where the inertial effects are negligible. A way to evaluate the importance of the inertial effects in the flow is by the Reynolds number associated with the pores, which is defined by Eq. 2.2 [13].

$$Re_p = \frac{\rho U_c \delta}{\mu} \tag{2.2}$$

where Re_p refers to the Reynolds number associated with the pores, ρ to density, U_c to the characteristic velocity, δ to the characteristic porous size, and μ to the dynamic viscosity.

So, Darcy Law works well for Re_p lesser than 1. However, for other cases where the inertial effects are important, a new term is included to describe it. This new equation is called the Forchheimer equation and is presented by Eq. 2.3, where C_F refers to the inertial resistance coefficient [13].

$$\nabla P = -\frac{\mu}{K}\mathbf{u_s} - \frac{\rho C_F}{\sqrt{K}}|\mathbf{u_s}|\mathbf{u_s} \tag{2.3}$$

Even though Darcy's Law can model correctly the porous medium effects for low Re_p and the Forchheimer equation can be used accurately for high Re_p, still exist a transition regime between them. This regime occurs in the range of $1 < Re_p < 10$ and to describe it usually it is added an extra term to Eq. 2.1 which has a form of $|\mathbf{u}|^\alpha \mathbf{u}$, where $1 \leq \alpha \leq 2$ [13].

2.4 Particle-Laden Flows

Particle-Laden flows are a subclass of multiphase flows which consist in a two-phase fluid flow constituted by a continuous phase and a dispersed phase. The dispersed phase is a number of immiscible particles that are being carried by the continuous phase, which is a liquid or a gas and can also be referred to as the carrier phase.

Particle-Laden flows play a very important role since they are present in many different ways in people's daily lives. Some examples are the pollution particles in the air, the sand grains carried by the wind, and respiratory droplets released from a person containing COVID's virus.

Unlike the single-phase flows that have governing equations already well es-

tablished in the literature, the multiphase flows still have their correct governing equations discussed. Because of that, the study of multiphase flows, including the particle-laden flows, still is a challenging area [14].

Computational methods using Eulerian-Eulerian and Lagrangian-Eulerian approaches have been proving to be very useful to study this type of flow [15]. The most used ones are the equilibrium Eulerian approach, Eulerian approach, Lagrangian point particle approach, and the fully resolved approach [16]. A brief description of these methods is presented below, the description of the first two methods is based on BALACHANDAR AND EATON [15] while the description of the other two is based on TABAEIKAZEROONI [16].

An equilibrium Eulerian approach is an Eulerian-Eulerian approach that assumes that the particles are so small that their motion is only influenced by the surrounding fluid. Then, only the momentum and energy equations of the carrier phase must be solved, along with the particle concentration equation. The particle's velocity can be expressed as a function of the fluid velocity and the particle Stokes number.

The Eulerian approach is another method that uses the Eulerian-Eulerian approach. This method model the continuous and the dispersed phases as two interpenetrating fluid mediums. Then, unlike the previous approach, this one needs to solve the momentum and energy equations for both phases, taking into account in these equations the momentum and energy exchange between phases.

The advantage of this approach over the equilibrium Eulerian approach is that this one applies to larger particles. On the other hand, the disadvantage is that, since it is necessary to solve more equations, this one is more computationally expensive.

The Lagrangian point particle approach is a method that uses a Eulerian-Lagrangian approach and it is probably the most used method since it has a low computational cost. In this method, the carrier phase is represented in a fixed Eulerian frame while the dispersed phase is treated in a Lagrangian way. Moreover, the interaction between them and the surrounding fluid is modeled.

The fully resolved approach is another method based on the Eulerian-Lagrangian approach which solves the Navier-Stokes equations for all flow scales. To do that, the particle's geometry is represented in the physical domain with no-slip and no-penetration conditions being imposed on their surfaces to represent correctly the interaction between the particles and the fluid, not using any model.

2.5 Numerical Methods

Nowadays, computers have an important role in the science field, being necessary for solving a lot of problems. Thus, there is an engineering field that uses computational effort to apply numerical methods to solve fluid mechanics problems. This

field is known as CFD, which is short for Computational Fluid Dynamics. In this field, many numerical methods are used, but the most important ones are: Finite Difference, Finite Volume, and Finite Element [17].

The Finite Difference Method is the oldest and also the easiest method to use in simple geometry cases. This method consists of the discretization of the physical domain in a grid and the approximation of the equation derivative terms by Taylor series expansion or polynomial fitting at each grid node. After that, a linear system is obtained, which must be solved.

The main advantages of the Finite Difference Method are its simplicity and effectiveness for simple geometries. However, it is very difficult to use this method on more complex geometries, making it not useful for many problems. Another important disadvantage is that this method does not enforce the conservation principle [17].

In the Finite Volume Method, the physical domain is subdivided into a finite number of control volumes. Then, using an integral form of the conservation equations, these equations are applied to each control volume aiming to calculate the variable values for its centroid. Finally, an algebraic equation is obtained for each control volume centroid making a linear system that must be solved.

Unlike the Finite Difference Method, the Finite Volume Method is suitable for complex geometries and enforces fluid mechanics conservation principles. Another important advantage of this method is that it is simple to understand since all terms that need to be approximated have physical meaning [17].

In the Finite Element Method, the physical domain is also subdivided into a finite number of sub-regions which are usually called elements. Then, the governing equations are multiplied by a weight function and integrated over the entire domain. So, to discretize the equations for each computational node, the integral is approximated by shape functions [17].

According to LEWIS AND NITHIARASU AND SEETHARAMU [18], the solution process using the Finite Element Method can be summarized by the following steps:

1. Discretize the domain: The physical domain must be subdivided into elements, creating a computational mesh. In this method, it is possible to use a variety of element shapes, making the method applicable to complex geometries, which is one of its advantages.

2. Select shape functions: the shape function is responsible for representing the variation of the variables over an element. An element is constituted by nodes which at each one is stored the variable value and the shape function is responsible to set the relation between these values.

3. Form element equations: Using the shape functions, the governing equations can be approximated to a linear system for each element. So, a matrix and a vector load are obtained to represent this equation for each element

4. Assemble the element equations to obtain a global linear system: Since it was already obtained a linear system for each element, it is necessary to assemble this linear system, forming a global one. To do that, the element matrix and element vector load are used to form a global matrix and a global vector load.

5. Solve the linear system: After the assemblage step, it is necessary to solve the linear system. So, since there are a matrix and a load vector, it is possible to calculate the variable vector using one of the many solving methods that are available.

6. Calculate the secondary quantities: This last step is not always needed, just for some cases. The calculation of secondary quantities is necessary when there are more quantities of interest, despite the variables calculated. These quantities can be calculated through the values of the variables that were already obtained.

One of the main advantages of this method is the already mentioned ability to deal with complex geometries, which are the ones usually found in practical problems. Another important advantage is that this method is relatively easy to analyze in a mathematical way.

In general, the Finite Volume Method and the Finite Elements Method are both suitable methods for CFD simulations and none of them has a big advantage over the other. Then, it was adopted the Finite Element Method in this work due to the expertise that our research group has with this method.

2.6 CFD applied to DPF

Since CFD is an important methodology used to solve problems of fluid flow, it has been used to study the flow inside DPF. This usage is very important to ensure the high efficiency of the device and to improve it.

SAMEI [19] has made a 3D model of a specific DPF type and simulated the flow inside it. In order to simulate the flow, it was used the mass, momentum, and energy conservation equations along with the turbulence model $\kappa - \epsilon$ to calculate the turbulence effects and the Forchheimer equation to predict the flow in the porous medium. The particle behavior wasn't simulated in this work.

Moreover, the permeability was adjusted in order to represent the pressure drop on the filter in different situations, like clean and dirty filter situations. It also

carried out experiments with the modeled DPF, making it possible to compare the results between experimental and computational results, achieving a good agreement between them.

PISCAGLIA *et al* [20] developed a code that solves the conservation equations with the Darcy and Forchheimer terms included for the porous region and also is configured to track Lagrangian particles which represent the soot particles. The code is also capable to predict the sticking of these particles on the porous surface and to evaluate the increasing resistance on the device due to their accumulation.

JANISZEWSKI AND TEODORCZYK [21] used the commercial software FLUENT to simulate the regeneration process in a DPF. The DPF was modeled as 2D, consisting of a half inlet channel, a half outlet channel, a porous wall, and a soot layer deposited on the porous wall. Besides that, the porous wall and the soot layer were modeled as a porous medium.

It was used in the inlet and outlet channels conservation equations to calculate the flow behavior whereas the porous wall and soot layer used similar equations but took into account the porosity and added the Darcy term. It was used these equations to calculate the temperature, velocity, pressure fields, and mass fraction. After that, the soot mass depletion was calculated by an outsourcing procedure and then the energy equation was solved. Finally, the temperature, velocity, pressure, and mass fraction can be calculated and this process is done again until it reaches the stop time.

DEUSCHLE *et al* [22] also used the commercial software FLUENT to predict the filtration, regeneration, and deposit rearrangement processes in the Diesel Particulate Filter. They used as computational domain a 2D model consisting of half of an inlet channel and half of an outlet channel.

The commercial code uses the continuity and Navier-Stokes equations to calculate the fluid flow while the particle tracks of the solid phase were determined using an Euler-Lagrange method. To compute the particle's trajectory it is made integration of the forces acting in each particle. After all these calculations, user-defined subroutines are used to predict the mass deposition, regeneration, and rearrangement processes in the filter. Finally, all these calculations are done iteratively, until it reaches a predefined final time.

PISCAGLIA *et al* [23] have developed at OpenFOAM, an open source software, a new solver for reacting and compressible flow through a porous medium and used it to study the flow inside DPF. This solver uses the usual conservation equations with the addition of the Darcy and Forchheimer terms in the momentum conservation equation.

In their work, they have used this new solver to predict the hydrodynamic characteristics of a 3D multi-channel DPF model. So, they could make a comparison

between simulation and experimental results, reaching a good agreement between them and concluding that the code was reliable.

PISCAGLIA *et al* [24] used an open-source code to simulate a three-dimensional flow containing solid particles inside a DPF. To simulate the gas phase, it was used conservation equations with spray source terms included to represent the solid-gas interaction and Darcy and Forchheimer terms included in the momentum equation to represent the porous media effects.

In their work, it was also calculated the solid particles' behavior through a Lagrangian approach. To simulate this behavior was used a technique to model sprays, which consist of representing a certain number of droplets that have an equal location, size, temperature, and velocity as a particle. So, the droplets have the same trajectory as their respective particle and the particles exchanges mass, momentum, and energy with the gas phase. This exchange between particles and gas is mathematically represented in the equations by the spray source terms.

The particle motion was calculated as a function of the relative velocity between the particle and the gas, and of the drag. Finally, it is possible to estimate the solid mass that is retained in the filter by tracking the particles. To do that, it is evaluated the particles that are in the filter region and an estimation is made about the percentage of the particle mass that will be retained. This estimation is made using the device filtration efficiency.

KONSTANDOPOULOS *et al* [25] used a 1D analytical model and 3D CFD simulations to study the behavior of the flow inside a DPF with a continuously regenerating trap. The 3D CFD simulations were carried out using the commercial software FLUENT, which uses the Navier-Stokes equations with the addition of the Darcy and Forchheimer terms in the porous medium. Moreover, they also obtained experimental results and made a comparison between their results with the analytical and CFD results. It was noted a good agreement between them.

Since the DPF which was studied in their work had a continuous regeneration process going on, the device was modeled as if its filter was clean or lightly loaded. Finally, the 1D model was used to obtain a DPF design that would result in the least pressure drop inside the device.

SOUZA [26] and SOUZA AND ANJOS [27] developed a computational code in Python using an Euler-Lagrange approach to study DPF flow. The continuous phase was simulated using the conservation equations for incompressible fluids while the solid particles were simulated by applying Newton's second law and taking into account that the forces applied to the particles were gravity, buoyancy, and drag forces. Besides that, it was also added the Darcy and Forchheimer terms in the momentum equations to model the porous medium effects. Finally, it was used the Finite Element Method (FEM) to solve the differential equations.

SBRIZZAI *et al* [28] used a three-dimensional approach to simulate the diesel soot particles inside a DPF. To calculate the continuous phase, it was used the Navier-Stokes equations with the Darcy equation being used along with them in the porous domain. Moreover, the commercial software Star-CD was used to solve these equations through the finite volume method.

After that, it was also simulated the solid phase, which was constituted by the particulate matter. In this work, it was taken into account that the particles were in the PM2.5 range, which means that the particles have diameters smaller than 2.5 μm. At this size range, there are particles having dimensions smaller than the mean free path of the molecules of the gas which constitutes the continuous phase. So, it was necessary to include rarefied gas hypotheses to study their behavior.

The particle's trajectory was calculated using a Lagrangian approach by integrating over time the motion equation. They were modeled as non-interacting and non-deformable solid spheres and the interaction between them and the continuous phase was modeled by a one-way coupling momentum transfer between them.

Finally, it was also modeled the interaction between particles and the porous wall. The model used was based on impact kinetic energy loss, relating the velocities before and after the interaction through a coefficient of restitution which was also modeled. This coefficient of restitution model is such that for particles with a velocity lower than 2 m/s, it has a value near zero, making it possible to assume that these particles were captured by the porous wall.

BENSAID *et al* [29] studied the multi-phase flow inside DPF using an Eulerian-Eulerian approach. The continuous phase was calculated using continuity and momentum balance equations. In these equations, it was taken into account the volume fraction of the gas and the inter-phase interaction due to drag.

The deposition rate of soot into the filter was calculated by a transport equation that takes into account the local particle velocity, the volume fraction of the particles, the particle density, and the filter properties. Moreover, the accumulation of soot in the filter changes the filter characteristics, making it to be an iterative process.

After seeing all these works that simulated the flow inside a DPF, it is possible to see that there are many different approaches being used for similar cases with no approach being considered the most suitable. Then, this work aims to study and develop an approach suitable for the specific case of flow inside the DPF with biodiesel particles.

Chapter 3

Mathematical Model

3.1 Continuous Phase

The continuous phase behavior can be modeled by the conservation equations of mass, momentum, and energy. Accordingly to BATCHELOR [30], the mass conservation equation for an incompressible case is presented by Eq. 3.1, where **u** represents the velocity vector.

$$\nabla \cdot \mathbf{u} = 0 \tag{3.1}$$

The momentum equation conservation for a case where, in addition to the incompressible flow hypotheses, it is also possible to consider that the fluid density and viscosity are constant, is given by Eq. 3.2 [30].

$$\rho \frac{D\mathbf{u}}{Dt} = -\nabla P + \mu \nabla^2 \mathbf{u} + \rho \mathbf{g} \tag{3.2}$$

where ρ is the fluid density, **u** is the velocity vector, P is the pressure, μ is the dynamic viscosity and **g** is the gravity vector. Then, adopting the already mentioned hypothesis of incompressible flow, density, and viscosity constants, Eq. 3.1 and Eq. 3.2 are used to model the hydrodynamic characteristics of the flow, i. e., they are used to calculate the velocity and pressure fields. It is also possible to calculate the temperature field through the energy conservation equation.

However, only these equations are not enough to solve the velocity and pressure of the flow, it is also necessary to apply boundary conditions in the problem. In this work, it was used the boundary conditions of the inlet with constant velocity, the outlet with null pressure, the wall condition, and the symmetry condition which will be later explained in detail.

An important way to represent the governing equations of a problem is by using the dimensionless form of the equations. This form has important advantages, since it is very revealing, making it possible to obtain results that will be the same for

different cases if they are dynamically similar. The principle of dynamical similarity is very important and used widely in experiments since it makes it possible to estimate the real conditions by experimenting with different parameters which are easier to reproduce in a laboratory [30].

Then, introducing L_c as a characteristic length and U_c as a characteristic velocity, it is possible to express the variables in a dimensionless form:

$$\mathbf{x}' = \frac{\mathbf{x}}{L_c}, \quad \mathbf{u}' = \frac{\mathbf{u}}{U_c}, \quad t' = t\frac{U_c}{L_c}, \quad P' = \frac{P}{\rho U_c^2}, \quad \mathbf{g}' = \frac{\mathbf{g}}{|\mathbf{g}|} \tag{3.3}$$

where $\mathbf{x}$ refers to the position vector, $\mathbf{u}$ to the velocity vector, t to time, P to pressure, ρ to density, $\mathbf{g}$ to gravity vector and the $'$ symbol is used to refer to the dimensionless form.

So, rearranging the conservation of mass and momentum equations (Eq. 3.1 and Eq. 3.2) to their dimensionless form, the following equations are obtained, respectively:

$$\nabla \cdot \mathbf{u}' = 0 \tag{3.4}$$

$$\frac{D\mathbf{u}'}{Dt} = -\nabla P' + \frac{1}{Re}\nabla^2 \mathbf{u}' + \frac{1}{Fr^2}\mathbf{g}' \tag{3.5}$$

where Re is the Reynolds number and Fr is the Froude number. Both numbers are presented by the following equations, respectively:

$$Re = \frac{\rho U_c L_c}{\mu} \tag{3.6}$$

$$Fr = \frac{U_c}{\sqrt{|\mathbf{g}| L_c}} \tag{3.7}$$

3.2 Porous Region

Since a direct simulation of the flow inside the porous would be a very complex problem to solve, the porous region will be modeled in this work. Then, an approach based on the Forchheimer equation, presented by Eq. 2.3, will be used.

An approach that could be used to solve this problem is the use of Forchheimer equation (Eq. 2.3) along with the continuity equation (Eq. 3.1) to describe the flow behavior. Then, it would need to be set coupling conditions between the porous region and the other regions across their interfaces. However, this approach can be complex to use because of the difference in the nature between the equations used in the different regions [13].

So, what can be done to mitigate the problem of the last approach is to use another one called the penalization approach. It consists of modifying the momentum conservation equation (Eq. 3.2) by adding two penalization terms related to the Forchheimer equation (Eq. 2.3) to represent the porous medium effects on the flow with the superficial velocity being approximated as the velocity of the flow in this region. The modified momentum conservation equation is presented by Eq. 3.8 [13].

$$\rho\frac{D\mathbf{u}}{Dt} = -\nabla P + \mu\nabla^2\mathbf{u} + \rho\mathbf{g} - \left(\frac{\mu}{K}\mathbf{u} + \frac{\rho C_F}{\sqrt{K}}|\mathbf{u}|\mathbf{u}\right)\varepsilon \tag{3.8}$$

where ρ is the fluid density, $\mathbf{u}$ is the velocity vector, P is the pressure, μ is the dynamic viscosity, $\mathbf{g}$ is the gravity vector, K is the permeability coefficient, C_F is the inertial resistance coefficient and ε is the penalty coefficient which values are $\varepsilon = 0$ for the fluid region and $\varepsilon = 1$ for the porous region.

As mentioned before, the dimensionless form of equations is an important representation form. So, using again the dimensionless variables, presented by Eq. 3.3, it can be obtained the dimensionless form of the modified momentum conservation equation (Eq. 3.8) presented by Eq. 3.9.

$$\frac{D\mathbf{u}'}{Dt} = -\nabla P' + \frac{1}{Re}\nabla^2\mathbf{u}' + \frac{1}{Fr^2}\mathbf{g}' - (Di_1\mathbf{u}' + Di_2|\mathbf{u}'|\mathbf{u}')\varepsilon \tag{3.9}$$

where $\mathbf{u}'$ is the dimensionless velocity vector, P' is the dimensionless pressure, $\mathbf{g}'$ is the dimensionless gravity vector, Re is the Reynolds number (Eq. 3.6), Fr is the Froude number (Eq. 3.7). Di_1 and Di_2 are dimensionless groups defined according to Eq. 3.10 and Eq. 3.11.

$$Di_1 = \frac{\mu L_c}{\rho K U_c} \tag{3.10}$$

$$Di_2 = \frac{L_c C_F}{\sqrt{K}} \tag{3.11}$$

3.3 Dispersed Phase

In this work, it is going to be used the point particle approach to model the behavior of the dispersed phase. This model was adopted due to its low computational effort, simplicity, and ability to handle well cases with a great number of particles. The method consists of modeling each particle as a point source of mass, momentum, and energy. Then, in this case, where it is possible to assume that there is no mass or energy exchange, the particle motion equation can be obtained in a Lagrangian view using Newton's second law [31].

The dispersed phase is constituted by the particulate matter exhausted by the

engine due to biodiesel combustion and it is going to be modeled as non-deformable spherical particles. The diameter of these particles is about 100 ηm accordingly to SOUZA [26].

In order to model the particles' behavior, it is necessary to understand their interactions with the surroundings. According to ELGHOBASHI [32], for turbulent particle-laden flows with very small values of volume fraction particles, values less than 10^{-6}, the collision between particles and the effect of the particles on the flow can be neglected, only taking into account the influence of the fluid on the particles. This coupling between the particles and their surrounding is called one-way coupling. In this work, the particle volume fraction is going to be also very small and, because of that, the one-way coupling is going to be adopted here.

The particle motion in a one-way coupling condition is governed by the forces exerted by the carrier phase. For a particle immersed in a fluid, the main forces acting on it are drag, lift, buoyancy, added mass, and history forces. However, usually, in gas-solid particle-laden flows the lift, buoyancy, added mass, and history forces can be neglected due to the great particle density value in comparison with the gas density value [31].

Moreover, for particles in the submicrometer range, the Brownian diffusion effects become important and must be also taken into account to compute their behavior [33]. Then, in this work, we consider that the forces acting on the particles are gravity, drag, and Brownian forces. Therefore, Eq. 3.12 presents the particle motion equation.

$$m_p \frac{d\mathbf{v}}{dt} = m_p \mathbf{g} + \mathbf{F_D} + \mathbf{F_B} \tag{3.12}$$

where m_p is the particle mass, $\mathbf{v}$ is the particle velocity, t is the time, $\mathbf{g}$ is the gravity vector, $\mathbf{F_D}$ is the drag force and $\mathbf{F_B}$ is the Brownian force.

The drag force for spherical particles in the submicrometer range can be expressed by Stokes' law corrected by a correction factor [33]. Then, the drag force for this work's case is presented by Eq. 3.13

$$\mathbf{F_D} = \frac{3\pi\mu d}{C_c}(\mathbf{u} - \mathbf{v}) \tag{3.13}$$

where $\mathbf{F_D}$ is the drag force, μ is the dynamic viscosity, d is the particle diameter, C_c is the Cunningham factor, $\mathbf{u}$ is the fluid velocity vector and $\mathbf{v}$ is the particle velocity vector.

The Cunningham factor is presented by Eq. 3.14, where λ is the molecular mean free path of the gas.

$$C_c = 1 + \frac{2\lambda}{d}\left[1.257 + 0.4e^{-1.1\left(\frac{d}{2\lambda}\right)}\right] \tag{3.14}$$

The Brownian motion is a random motion caused by the collisions of molecules with particles [14]. Then, the Brownian force is the force exerted on the particles due to Brownian motion. Moreover, the Brownian force can be modeled as a white noise Gaussian random process, and, for this case, the Brownian force is going to be modeled as presented by Eq. 3.15 [33].

$$\mathbf{F_B} = m_p \mathbf{G} \sqrt{\frac{\pi S_0}{\Delta t}} \tag{3.15}$$

where $\mathbf{F_B}$ is the Brownian force, m_p is the particle mass, $\mathbf{G}$ is a vector containing a zero-mean independent Gaussian random number of unit variance for each flow direction, S_0 is the spectral intensity of the noise and Δt is the time difference between time steps.

The spectral intensity of the noise is given by Eq. 3.16, where ν is the kinematic viscosity, k is the Boltzmann constant, T is the absolute temperature of the fluid, ρ is the fluid density, d is the particle diameter, ρ_p is the particle density and C_c is the Cunningham factor.

$$S_0 = \frac{216 \nu k T \rho}{\pi d^5 \rho_p^2 C_c} \tag{3.16}$$

Then, substituting Eq. 3.13 and Eq. 3.15 into Eq. 3.12 and simplifying the equation, knowing that the particle mass m_p is equal to the product of the particle density and its volume, it is possible to get the equation that represents the particle motion in this work's cases, presented by Eq. 3.17.

$$\frac{d\mathbf{v}}{dt} = \mathbf{g} + \frac{18\mu}{d^2 C_c \rho_p}(\mathbf{u} - \mathbf{v}) + \mathbf{G}\sqrt{\frac{\pi S_0}{\Delta t}} \tag{3.17}$$

Where $\mathbf{v}$ is the particle velocity vector, $\mathbf{g}$ is the gravity vector, μ is the dynamic viscosity, d is the particle diameter, C_c is the Cunningham factor, $\mathbf{u}$ is the fluid velocity, $\mathbf{G}$ is a vector containing a zero-mean independent Gaussian random number of unit variance for each flow direction, S_0 is the spectral intensity of the noise and Δt is the time difference between time steps.

It was used for the dispersed phase the initial condition of particulates randomly displaced along the domain's inlet, far before they have reached the DPF. Besides that, it was used the boundary conditions of totally elastic collision when the particles reach the plug. Lastly, it was considered that if one particle leaves the computational domain through the symmetry boundary, another similar particle is going to enter the domain symmetrically to the first one due to the problem's symmetry. This last condition is mathematically equal to the totally elastic condition.

Finally, it is necessary to get the dimensionless form of Eq. 3.17 in the same way that was done to get Eq. 3.4, Eq. 3.5 and 3.9. So, the dimensionless form of the

particle motion equation is presented by Eq. 3.18.

$$\frac{d\mathbf{v}'}{dt'} = \frac{1}{Fr^2}\mathbf{g}' + \frac{18\mu L_c}{d^2 C_c \rho_p U_c}(\mathbf{u}' - \mathbf{v}') + \frac{\mathbf{G}}{U_c}\sqrt{\frac{L_c \pi S_0}{U_c \Delta t'}} \tag{3.18}$$

Where t', $\mathbf{g}'$, $\mathbf{u}'$ are dimensionless variables presented by Eq. 3.3, $\mathbf{v}'$ is the dimensionless form of the particle velocity, Fr is the Froude number presented by Eq. 3.7, μ is the dynamic viscosity, L_c is the characteristic length, U_c is the characteristic velocity, d is the particle diameter, C_c is the Cunningham factor, ρ_p is the particle density, $\mathbf{G}$ is a vector containing a zero-mean independent Gaussian random number of unit variance for each flow direction, S_0 is the spectral intensity of the noise and $\Delta t'$ is the dimensionless time difference between time steps.

The dimensionless form of the particle velocity is defined as presented by Eq. 3.19.

$$\mathbf{v}' = \frac{\mathbf{v}}{U_c} \tag{3.19}$$

Chapter 4

Numerical Methods

In this work, it is necessary to solve a multiphase flow case that has two phases, gas and solid. The phases will be treated as uncoupled, solving firstly the fluid phase and, after that, solving the solid phase using the results that were get for the fluid phase. So, different numerical methods will be used to solve the equations of each phase. The fluid phase will be solved using the Finite Element Method while the solid phase equations will be solved using the Runge-Kutta method.

4.1 Finite Element Method

4.1.1 Weak Form

The main parts of the Finite Element Method are establishing the weak form of the problem and obtaining an approximated solution for this weak form by using some special functions [34]. So, firstly, it is necessary to obtain the weak formulation of the governing equations of the problem.

In order to establish the weak formulation, two classes of function are necessary. The first one is constituted by trial solutions, which are functions that satisfy boundary conditions and that have square-integrable derivatives [34]. The velocity vector $\mathbf{u}$ and the pressure P are trial solutions in this work.

The other class of function is the weighting function class. The weighting functions also must have derivatives that are square-integrable. However, unlike the trial solutions, the weighting functions must be equal to zero on the problem boundary [34].

It is necessary to obtain the weak form of the governing equations. So, since the governing equations are presented by Eq. 3.4 and Eq. 3.9, it is necessary to operate them with weighting functions and to integrate them over the domain. Then, if q and $\mathbf{w}$ are weighting functions, the following equations are obtained by this operation:

$$\int_{\Omega} q(\nabla \cdot \mathbf{u}')d\Omega = 0 \tag{4.1}$$

$$\begin{aligned}\int_{\Omega} \mathbf{w} \cdot \frac{D\mathbf{u}'}{Dt} d\Omega = &- \int_{\Omega} \mathbf{w} \cdot \nabla P' d\Omega + \frac{1}{Re} \int_{\Omega} \mathbf{w} \cdot \nabla^2 \mathbf{u}' d\Omega + \frac{1}{Fr^2} \int_{\Omega} \mathbf{w} \cdot \mathbf{g}' d\Omega \\ &- \int_{\Omega} \mathbf{w} \cdot (Di_1 \mathbf{u}' + Di_2 |\mathbf{u}'| \mathbf{u}') \varepsilon d\Omega\end{aligned} \tag{4.2}$$

Where q and $\mathbf{w}$ are the weighting functions and Ω is the domain of the problem. Also, $\mathbf{u}'$ is the dimensionless velocity vector, P' is the dimensionless pressure, Re is the Reynolds number, Fr is the Froude number, $\mathbf{g}'$ is the dimensionless gravity vector, Di_1 and Di_2 are dimensionless groups defined by Eq. 3.10 and Eq. 3.11 and ε is a penalty coefficient.

Looking at the last term of Eq. 4.2, the term related to the porous medium, there is a penalty coefficient whose function is to make this term disappear in the fluid region. This fluid region can be understood as a subdomain of the problem. Moreover, the problem can be divided into two subdomains: a fluid domain and a porous domain. So, since the porous related term disappears in the fluid domain, this term can be rewritten as follows:

$$\int_{\Omega} \mathbf{w} \cdot (Di_1 \mathbf{u}' + Di_2 |\mathbf{u}'| \mathbf{u}') \varepsilon d\Omega = \int_{\Omega_p} \mathbf{w} \cdot (Di_1 \mathbf{u}' + Di_2 |\mathbf{u}'| \mathbf{u}') d\Omega_p \tag{4.3}$$

Where Ω refers to the entire domain while Ω_p refers to the porous domain.

Still looking to Eq. 4.2, integrating by parts the pressure and laplacian terms and also using the divergence theorem, the following relations are obtained:

$$\int_{\Omega} \mathbf{w} \cdot \nabla P' d\Omega = - \int_{\Omega} P' (\nabla \cdot \mathbf{w}) d\Omega + \int_{\Gamma} P' \mathbf{w} \cdot \mathbf{n} d\Gamma \tag{4.4}$$

$$\int_{\Omega} \mathbf{w} \cdot \nabla^2 \mathbf{u}' d\Omega = - \int_{\Omega} \nabla \mathbf{w}^T : \nabla \mathbf{u}' d\Omega + \int_{\Gamma} \mathbf{w} \cdot \nabla \mathbf{u}' \cdot \mathbf{n} d\Gamma \tag{4.5}$$

Where Γ is the boundary surface of the problem domain Ω and $\mathbf{n}$ is the normal vector to the boundary surface Γ.

Substituting Eq. 4.3, Eq. 4.4 and Eq. 4.5 into the Eq. 4.2, the following one is obtained:

$$\int_\Omega \mathbf{w}\cdot\frac{D\mathbf{u}'}{Dt'}d\Omega = \int_\Omega P'(\nabla\cdot\mathbf{w})d\Omega - \int_\Gamma P'\mathbf{w}\cdot\mathbf{n}d\Gamma + \frac{1}{Re}\left(-\int_\Omega \nabla\mathbf{w}^T : \nabla\mathbf{u}'d\Omega + \right.$$
$$\left. + \int_\Gamma \mathbf{w}\cdot\nabla\mathbf{u}'\cdot\mathbf{n}d\Gamma\right) + \frac{1}{Fr^2}\int_\Omega \mathbf{w}\cdot\mathbf{g}'d\Omega - \int_{\Omega_p}\mathbf{w}\cdot(Di_1\mathbf{u}' + Di_2|\mathbf{u}'|\mathbf{u}')d\Omega_p \tag{4.6}$$

So, Eq. 4.1 and Eq. 4.6 are, respectively, the weak form of Eq. 3.4 and Eq. 3.9, which are the governing equations of the problem. However, in this work, the only types of boundary conditions that are going to be used are Dirichlet and Neumann homogeneous, and for these types, the boundary terms, represented by an integral over Γ, are going to be equal to zero. So, these terms will be neglected in this work.

$$\int_\Omega \mathbf{w}\cdot\frac{D\mathbf{u}'}{Dt'}d\Omega = \int_\Omega P'(\nabla\cdot\mathbf{w})d\Omega - \frac{1}{Re}\int_\Omega \nabla\mathbf{w}^T : \nabla\mathbf{u}'d\Omega + \frac{1}{Fr^2}\int_\Omega \mathbf{w}\cdot\mathbf{g}'d\Omega$$
$$- \int_{\Omega_p}(Di_1 + Di_2|\mathbf{u}'|)(\mathbf{w}\cdot\mathbf{u}')d\Omega_p \tag{4.7}$$

Then, Eq. 4.1 and Eq. 4.7 are the equations that are going to be discretized by the Finite Element Method. But, before applying the discretization process, it is interesting to rewrite Eq. 4.1 and Eq. 4.7 for clarity reasons. The equations can be rewritten as functions of the vectors components, that is $\mathbf{u}' = [u_1' \;\; u_2' \;\; u_3']^T$, $\mathbf{g}' = [g_1' \;\; g_2' \;\; g_3']^T$ and $\mathbf{w} = [w_1 \;\; w_2 \;\; w_3]^T$, as presented by the following equations.

$$\int_\Omega q\frac{\partial u_1'}{\partial x_1'}d\Omega + \int_\Omega q\frac{\partial u_2'}{\partial x_2'}d\Omega + \int_\Omega q\frac{\partial u_3'}{\partial x_3'}d\Omega = 0 \tag{4.8}$$

$$\int_\Omega \left(w_1\frac{Du_1'}{Dt'} + w_2\frac{Du_2'}{Dt'} + w_3\frac{Du_3'}{Dt'}\right)d\Omega = \int_\Omega P'\left(\frac{\partial w_1}{\partial x_1'} + \frac{\partial w_2}{\partial x_2'} + \frac{\partial w_3}{\partial x_3'}\right)d\Omega$$
$$-\frac{1}{Re}\int_\Omega\left(\frac{\partial w_1}{\partial x_1'}\frac{\partial u_1'}{\partial x_1'} + \frac{\partial w_1}{\partial x_2'}\frac{\partial u_1'}{\partial x_2'} + \frac{\partial w_1}{\partial x_3'}\frac{\partial u_1'}{\partial x_3'} + \frac{\partial w_2}{\partial x_1'}\frac{\partial u_2'}{\partial x_1'} + \frac{\partial w_2}{\partial x_2'}\frac{\partial u_2'}{\partial x_2'} + \right.$$
$$\left.\frac{\partial w_2}{\partial x_3'}\frac{\partial u_2'}{\partial x_3'} + \frac{\partial w_3}{\partial x_1'}\frac{\partial u_3'}{\partial x_1'} + \frac{\partial w_3}{\partial x_2'}\frac{\partial u_3'}{\partial x_2'} + \frac{\partial w_3}{\partial x_3'}\frac{\partial u_3'}{\partial x_3'}\right)d\Omega + \frac{1}{Fr^2}\int_\Omega(w_1g_1' +$$
$$w_2g_2' + w_3g_3')d\Omega - \int_{\Omega_p}(Di_1 + Di_2|\mathbf{u}'|)(w_1u_1' + w_2u_2' + w_3u_3')d\Omega_p \tag{4.9}$$

Furthermore, it is possible to note that, if Eq. 4.10, Eq. 4.11, and 4.12 were satisfied, Eq. 4.9 will also be satisfied. So, it is possible to solve Eq. 4.9 by splitting it into the directions x_1, x_2, and x_3, presented by, respectively, Eq. 4.10, Eq. 4.11, and 4.12

$$\int_\Omega w_1 \frac{Du_1'}{Dt'} d\Omega = \int_\Omega P' \frac{\partial w_1}{\partial x_1'} d\Omega - \frac{1}{Re} \int_\Omega \left(\frac{\partial w_1}{\partial x_1'} \frac{\partial u_1'}{\partial x_1'} + \frac{\partial w_1}{\partial x_2'} \frac{\partial u_1'}{\partial x_2'} + \frac{\partial w_1}{\partial x_3'} \frac{\partial u_1'}{\partial x_3'} \right) d\Omega + \frac{1}{Fr^2} \int_\Omega w_1 g_1' d\Omega - \int_{\Omega_p} (Di_1 + Di_2 |\mathbf{u}'|) w_1 u_1' d\Omega_p \tag{4.10}$$

$$\int_\Omega w_2 \frac{Du_2'}{Dt'} d\Omega = \int_\Omega P' \frac{\partial w_2}{\partial x_2'} d\Omega - \frac{1}{Re} \int_\Omega \left(\frac{\partial w_2}{\partial x_1'} \frac{\partial u_2'}{\partial x_1'} + \frac{\partial w_2}{\partial x_2'} \frac{\partial u_2'}{\partial x_2'} + \frac{\partial w_2}{\partial x_3'} \frac{\partial u_2'}{\partial x_3'} \right) d\Omega + \frac{1}{Fr^2} \int_\Omega w_2 g_2' d\Omega - \int_{\Omega_p} (Di_1 + Di_2 |\mathbf{u}'|) w_2 u_2' d\Omega_p \tag{4.11}$$

$$\int_\Omega w_3 \frac{Du_3'}{Dt'} d\Omega = \int_\Omega P' \frac{\partial w_3}{\partial x_3'} d\Omega - \frac{1}{Re} \int_\Omega \left(\frac{\partial w_3}{\partial x_1'} \frac{\partial u_3'}{\partial x_1'} + \frac{\partial w_3}{\partial x_2'} \frac{\partial u_3'}{\partial x_2'} + \frac{\partial w_3}{\partial x_3'} \frac{\partial u_3'}{\partial x_3'} \right) d\Omega + \frac{1}{Fr^2} \int_\Omega w_3 g_3' d\Omega - \int_{\Omega_p} (Di_1 + Di_2 |\mathbf{u}'|) w_3 u_3' d\Omega_p \tag{4.12}$$

4.1.2 Galerkin Method

After the definition of the weak formulation of the problem, it is necessary a method to obtain an approximate solution for it. The method that is going to be used is the Galerkin Method.

This method is only going to be used in the spatial domain while the temporal term is going to be discretized by another method that will be discussed later. So, because of that, the temporal term will remain a continuous variable for now.

Accordingly to HUGHES [34], the first step is to discretize the continuous domain in a finite number of elements. So, the weak form of the problem, presented by Eq. 4.8, Eq. 4.10, Eq. 4.11, and Eq. 4.12, must be solved for each element. This transformation is represented by the following equations:

$$\sum_e^{NE} \left(\int_{\Omega^e} q \frac{\partial u_1'}{\partial x_1'} d\Omega + \int_{\Omega^e} q \frac{\partial u_2'}{\partial x_2'} d\Omega + \int_{\Omega^e} q \frac{\partial u_3'}{\partial x_3'} d\Omega \right) = 0 \tag{4.13}$$

$$\sum_e^{NE} \int_{\Omega^e} w_1 \frac{Du_1'}{Dt'} d\Omega = \sum_e^{NE} \int_{\Omega^e} P' \frac{\partial w_1}{\partial x_1'} d\Omega - \frac{1}{Re} \sum_e^{NE} \int_{\Omega^e} \left(\frac{\partial w_1}{\partial x_1'} \frac{\partial u_1'}{\partial x_1'} + \frac{\partial w_1}{\partial x_2'} \frac{\partial u_1'}{\partial x_2'} + \frac{\partial w_1}{\partial x_3'} \frac{\partial u_1'}{\partial x_3'} \right) d\Omega + \frac{1}{Fr^2} \sum_e^{NE} \int_{\Omega^e} w_1 g_1' d\Omega - \sum_e^{NE} \int_{\Omega_p^e} (Di_1 + Di_2 |\mathbf{u}'|) w_1 u_1' d\Omega_p \tag{4.14}$$

$$\sum_{e}^{NE}\int_{\Omega^e} w_2\frac{Du_2'}{Dt'}d\Omega = \sum_{e}^{NE}\int_{\Omega^e} P'\frac{\partial w_2}{\partial x_2'}d\Omega - \frac{1}{Re}\sum_{e}^{NE}\int_{\Omega^e}\left(\frac{\partial w_2}{\partial x_1'}\frac{\partial u_2'}{\partial x_1'}+\right.$$
$$\left.\frac{\partial w_2}{\partial x_2'}\frac{\partial u_2'}{\partial x_2'}+\frac{\partial w_2}{\partial x_3'}\frac{\partial u_2'}{\partial x_3'}\right)d\Omega + \frac{1}{Fr^2}\sum_{e}^{NE}\int_{\Omega^e} w_2 g_2' d\Omega - \tag{4.15}$$
$$\sum_{e}^{NE}\int_{\Omega_p^e}(Di_1 + Di_2|\mathbf{u}'|)w_2 u_2' d\Omega_p$$

$$\sum_{e}^{NE}\int_{\Omega^e} w_3\frac{Du_3'}{Dt'}d\Omega = \sum_{e}^{NE}\int_{\Omega^e} P'\frac{\partial w_3}{\partial x_3'}d\Omega - \frac{1}{Re}\sum_{e}^{NE}\int_{\Omega^e}\left(\frac{\partial w_3}{\partial x_1'}\frac{\partial u_3'}{\partial x_1'}+\right.$$
$$\left.\frac{\partial w_3}{\partial x_2'}\frac{\partial u_3'}{\partial x_2'}+\frac{\partial w_3}{\partial x_3'}\frac{\partial u_3'}{\partial x_3'}\right)d\Omega + \frac{1}{Fr^2}\sum_{e}^{NE}\int_{\Omega^e} w_3 g_3' d\Omega - \tag{4.16}$$
$$\sum_{e}^{NE}\int_{\Omega_p^e}(Di_1 + Di_2|\mathbf{u}'|)w_3 u_3' d\Omega_p$$

Where e refers to the element, NE to the total number of elements, Ω^e to the element domain, and Ω_p^e to the domain of the elements which are in the porous region.

After that, it is necessary to get a discrete approximation for the variables. To achieve that, it is used interpolation functions, or shape functions, represent the value of the variables along the element. The problem variables discretized are presented by the following equation.

$$\begin{aligned} u_1 &= \sum_{i}^{NV} N_i u_{1i}, \quad u_2 = \sum_{i}^{NV} N_i u_{2i}, \quad u_3 = \sum_{i}^{NV} N_i u_{3i}, \quad P = \sum_{i}^{NP} L_i P_i, \\ w_1 &= \sum_{i}^{NV} N_i w_{1i}, \quad w_2 = \sum_{i}^{NV} N_i w_{2i}, \quad w_3 = \sum_{i}^{NV} N_i w_{3i}, \quad q = \sum_{i}^{NP} L_i q_i \end{aligned} \tag{4.17}$$

Where NV is the number of velocity nodes, NP is the number of pressure nodes, and N_i and L_i are interpolation functions.

Then, substituting Eq. 4.17 in Eq. 4.13, Eq. 4.14, Eq. 4.15, and Eq. 4.16, it is obtained a linear system, presented by Eq. 4.18, Eq. 4.19, Eq. 4.20 and Eq. 4.21. It is important to note that q_i, w_{1i}, w_{2i}, and w_{3i} were eliminated since they would be multiplying every term of Eq. 4.18, Eq. 4.19, Eq. 4.20 and Eq. 4.21, respectively.

$$\sum_{e}^{NE}\left(\int_{\Omega^e}\sum_{i}^{NP}\sum_{j}^{NV}L_i\frac{\partial N_j}{\partial x_1'}u_{1j}d\Omega+\int_{\Omega^e}\sum_{i}^{NP}\sum_{j}^{NV}L_i\frac{\partial N_j}{\partial x_2'}u_{2j}d\Omega+\int_{\Omega^e}\sum_{i}^{NP}\sum_{j}^{NV}L_i\frac{\partial N_j}{\partial x_3'}u_{3j}d\Omega\right)=0 \tag{4.18}$$

$$\sum_{e}^{NE}\left(\int_{\Omega^e}\sum_{i}^{NV}\sum_{j}^{NV}N_iN_j\frac{Du_{1j}}{Dt'}d\Omega+\frac{1}{Re}\int_{\Omega^e}\sum_{i}^{NV}\sum_{j}^{NV}\left(\frac{\partial N_i}{\partial x_1'}\frac{\partial N_j}{\partial x_1'}+\frac{\partial N_i}{\partial x_2'}\frac{\partial N_j}{\partial x_2'}+\frac{\partial N_i}{\partial x_3'}\frac{\partial N_j}{\partial x_3'}\right)u_{1j}d\Omega+\int_{\Omega_p^e}\sum_{i}^{NV}\sum_{j}^{NV}(Di_1+Di_2|\mathbf{u}'|)N_iN_ju_{1j}d\Omega_p-\int_{\Omega^e}\sum_{i}^{NV}\sum_{j}^{NP}\frac{\partial N_i}{\partial x_1'}L_jP_jd\Omega\right)=\sum_{e}^{NE}\frac{1}{Fr^2}\int_{\Omega^e}\sum_{i}^{NV}\sum_{j}^{NV}N_iN_jg_{1j}d\Omega \tag{4.19}$$

$$\sum_{e}^{NE}\left(\int_{\Omega^e}\sum_{i}^{NV}\sum_{j}^{NV}N_iN_j\frac{Du_{2j}}{Dt'}d\Omega+\frac{1}{Re}\int_{\Omega^e}\sum_{i}^{NV}\sum_{j}^{NV}\left(\frac{\partial N_i}{\partial x_1'}\frac{\partial N_j}{\partial x_1'}+\frac{\partial N_i}{\partial x_2'}\frac{\partial N_j}{\partial x_2'}+\frac{\partial N_i}{\partial x_3'}\frac{\partial N_j}{\partial x_3'}\right)u_{2j}d\Omega+\int_{\Omega_p^e}\sum_{i}^{NV}\sum_{j}^{NV}(Di_1+Di_2|\mathbf{u}'|)N_iN_ju_{2j}d\Omega_p-\int_{\Omega^e}\sum_{i}^{NV}\sum_{j}^{NP}\frac{\partial N_i}{\partial x_2'}L_jP_jd\Omega\right)=\sum_{e}^{NE}\frac{1}{Fr^2}\int_{\Omega^e}\sum_{i}^{NV}\sum_{j}^{NV}N_iN_jg_{2j}d\Omega \tag{4.20}$$

$$\sum_{e}^{NE}\left(\int_{\Omega^e}\sum_{i}^{NV}\sum_{j}^{NV}N_iN_j\frac{Du_{3j}}{Dt'}d\Omega+\frac{1}{Re}\int_{\Omega^e}\sum_{i}^{NV}\sum_{j}^{NV}\left(\frac{\partial N_i}{\partial x_1'}\frac{\partial N_j}{\partial x_1'}+\frac{\partial N_i}{\partial x_2'}\frac{\partial N_j}{\partial x_2'}+\frac{\partial N_i}{\partial x_3'}\frac{\partial N_j}{\partial x_3'}\right)u_{3j}d\Omega+\int_{\Omega_p^e}\sum_{i}^{NV}\sum_{j}^{NV}(Di_1+Di_2|\mathbf{u}'|)N_iN_ju_{3j}d\Omega_p-\int_{\Omega^e}\sum_{i}^{NV}\sum_{j}^{NP}\frac{\partial N_i}{\partial x_3'}L_jP_jd\Omega\right)=\sum_{e}^{NE}\frac{1}{Fr^2}\int_{\Omega^e}\sum_{i}^{NV}\sum_{j}^{NV}N_iN_jg_{3j}d\Omega \tag{4.21}$$

The previous linear system can be presented in a matrix form, as presented by the following equations:

$$[D_x]\{u_1\}+[D_y]\{u_2\}+[D_z]\{u_3\}=0 \tag{4.22}$$

$$[M]\frac{D\{u_1\}}{Dt'}+\frac{1}{Re}[K]\{u_1\}+(Di_1+Di_2[U])[M_p]\{u_1\}-[G_x]\{p\}=\frac{1}{Fr^2}[M]\{g_1\} \tag{4.23}$$

$$[M]\frac{D\{u_2\}}{Dt'}+\frac{1}{Re}[K]\{u_2\}+(Di_1+Di_2[U])[M_p]\{u_2\}-[G_y]\{p\}=\frac{1}{Fr^2}[M]\{g_2\} \quad (4.24)$$

$$[M]\frac{D\{u_3\}}{Dt'}+\frac{1}{Re}[K]\{u_3\}+(Di_1+Di_2[U])[M_p]\{u_3\}-[G_z]\{p\}=\frac{1}{Fr^2}[M]\{g_3\} \quad (4.25)$$

Where $\{u_1\}$ is a column vector containing the value for velocity in x_1 direction for all velocity nodes, $\{u_2\}$ contain value of velocity in x_2 direction, $\{u_3\}$ contain value of velocity in x_3 direction, $\{g_1\}$, $\{g_2\}$, and $\{g_3\}$ contains all values of the gravity vector in direction x_1, x_2, and x_3, respectively, and $\{p\}$ contains pressure value for all pressure nodes.

$[M]$ is the mass matrix, $[K]$ is the stiffness matrix, $[G_x]$, $[G_y]$, and $[G_z]$ are part of the gradient matrix related to, respectively, x_1, x_2, and x_3 direction. Moreover, there are the matrices $[D_x]$, $[D_y]$, and $[D_z]$ which are defined as $[D_x] = [G_x]^T$, $[D_y] = [G_y]^T$, and $[D_z] = [G_z]^T$. There is also $[U]$, a diagonal matrix containing the velocity module value.

Finally, there is the $[M_p]$ which is the mass matrix relative only to the porous region. In other words, this means that the $[M_p]$ terms relative to the elements that are in the porous domain are equal to their related terms in $[M]$, while the terms relative to the elements outside the porous domain are going to be equal zero, unlike the related terms in $[M]$.

The matrices $[M]$, $[K]$, $[G_x]$, $[G_y]$, and $[G_z]$ are, respectively, assembles of the elementary sub-matrices $[m^e]$, $[k^e]$, $[g_x^e]$, $[g_y^e]$, and $[g_z^e]$, which are presented by the following equations.

$$[m^e] = \int_{\Omega^e} \sum_i^{NV} \sum_j^{NV} N_i N_j d\Omega, \quad (4.26)$$

$$[k^e] = \int_{\Omega^e} \sum_i^{NV} \sum_j^{NV} \left(\frac{\partial N_i}{\partial x_1'} \frac{\partial N_j}{\partial x_1'} + \frac{\partial N_i}{\partial x_2'} \frac{\partial N_j}{\partial x_2'} \right) d\Omega \quad (4.27)$$

$$[g_x^e] = \int_{\Omega^e} \sum_i^{NV} \sum_j^{NP} \frac{\partial N_i}{\partial x_1'} L_j d\Omega \quad (4.28)$$

$$[g_y^e] = \int_{\Omega^e} \sum_i^{NV} \sum_j^{NP} \frac{\partial N_i}{\partial x_2'} L_j d\Omega \quad (4.29)$$

$$[g_z^e] = \int_{\Omega^e} \sum_i^{NV} \sum_j^{NP} \frac{\partial N_i}{\partial x_3'} L_j d\Omega \quad (4.30)$$

Moreover, the matrix $[M_p]$ is an assembly of the sub-matrix $[m^e]$ for all e that belong to the porous region. Then, $[M_p]$ is defined as an assemble of the sub-matrix $[m_p^e]$ presented in Eq. 4.31.

$$[m_p^e] = \int_{\Omega_p^e} \sum_i^{NV} \sum_j^{NV} N_i N_j d\Omega, \tag{4.31}$$

4.1.3 Mesh Element

As already seen, in the Finite Element Method the domain is discretized in sub-regions called elements, and it is in these elements where the differential equations are approximated by shape functions. Therefore, the elements approximation can be classified by the element shape and by the order of the approximation [35].

The proper choice of the elements has great importance in CFD since it is responsible for the coupling of velocity and pressure and it also must satisfy the *Ladyzhenskaya-Babouska-Brezzi*, or just LBB, stability condition [36]. Therefore, in this work, it will be used the MINI and quadratic triangular elements for the two-dimensional cases and the tetrahedron MINI element for the three-dimensional cases, since all these elements satisfy the LBB condition.

The triangle MINI element is composed of 3 pressure nodes, which are located at the triangle vertices, and 4 velocity nodes, located at the triangle vertices and its centroid. The triangle quadratic element has 3 pressure nodes located at the vertices and 6 velocity nodes located in the vertices and in the edges mid-points. Finally, the tetrahedron MINI element has 4 pressure nodes located at its vertices and 5 velocity nodes located at the vertices and at its centroid. All these elements are presented schematically in Figure 4.1.

The functions L_i and N_i are responsible for interpolating the pressure and velocity, respectively, along the element. In the triangular elements, the L_i functions are the triangle barycentric coordinates concerning its vertices $i = 1, 2, 3$. For the triangle MINI element, the N_i is defined as presented by Eq. 4.32.

$$\begin{aligned} N_i &= L_i - 9L_1L_2L_3, \text{ for } i = 1, 2, 3 \\ N_4 &= 27L_1L_2L_3 \end{aligned} \tag{4.32}$$

For the triangle quadratic element, these functions are defined as presented by Eq. 4.33.

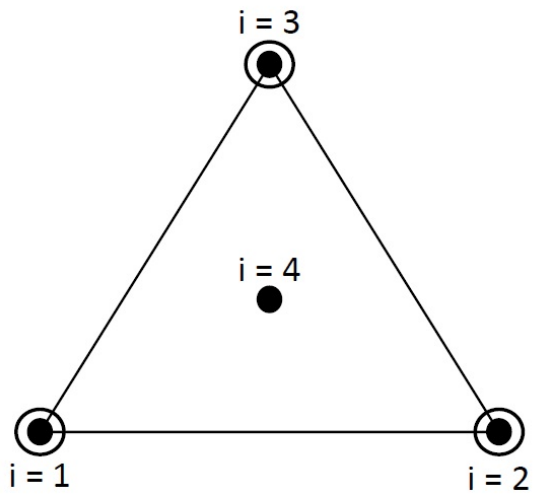

(a) Triangle MINI used 2D cases.

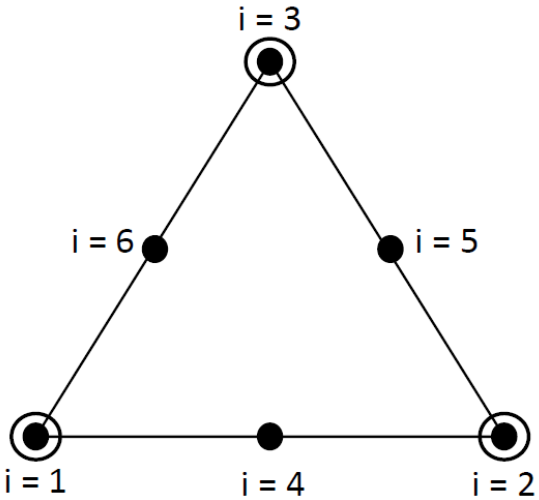

(b) Triangle Quadratic used in 2D cases.

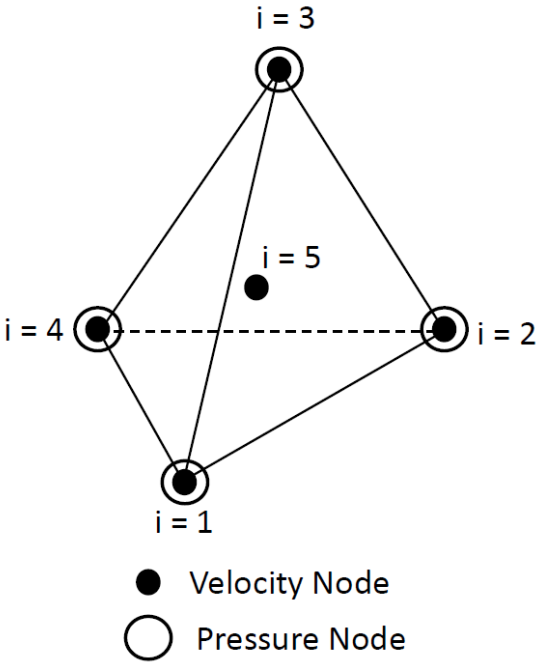

(c) Tetraedron MINI used in 3D cases.

Figure 4.1: Elements' representation.

$$
\begin{aligned}
N_i = (2L_i - 1)L_i, \text{ for } i = 1, 2, 3 \\
N_4 = 4L_1L_2 \\
N_5 = 4L_2L_3 \\
N_6 = 4L_1L_3
\end{aligned}
\tag{4.33}
$$

For three-dimensional simulations, the tetrahedron MINI element, the L_i functions are the tetrahedron barycentric coordinates and the N_i functions are based on them and presented by Eq. 4.34.

$$
\begin{aligned}
N_i = L_i - 64L_1L_2L_3L_4, \text{ for } i = 1, 2, 3, 4 \\
N_5 = 256L_1L_2L_3L_4
\end{aligned}
\tag{4.34}
$$

Finally, equations 4.26 to 4.30 were solved analytically for the triangle and tetrahedron MINI elements while they were solved numerically for the triangle quadratic element by using the Gaussian quadrature.

4.1.4 Semi-Lagrangian Method

After the application of the Galerkin method, the spatial terms are already discretized while the temporal term remains continuous. The temporal term, which is the term with material derivative, can be discretized by using the semi-Lagrangian method.

The semi-Lagrangian method is based on the Lagrangian coordinates, a system of coordinates that describe the fluid flow by following the fluid particles along its trajectory. Therefore, it would be possible to simulate the flow using these pure Lagrangian coordinates by updating the mesh at each time step accordingly to the particle trajectory. However, this approach could be very problematic since the particle's trajectory may be chaotic even for low Reynolds flow [36].

Then, to avoid this problem, the semi-Lagrangian method calculates the computational nodes' previous position in Lagrangian coordinates using the current time step velocity field and, after that, re-initializes the mesh at the next time step, recovering the original mesh. So, this method consists in approximating the material derivative of some variable using its values at the current and previous time steps and considering the different nodes' position at each time step. This approximation can be done by using an implicit first-order scheme as presented by Eq. 4.35 [36].

$$
\frac{D\alpha}{Dt} = \frac{\alpha^{n+1} - \alpha_d^n}{\Delta t} \tag{4.35}
$$

Where α is some random variable, Δt is the time between each time step, the superscripts $n+1$ and n refer to the next time step and current time step, respectively,

and the subscript d refers to the position from which the computational nodes have departed.

Moreover, the position of the departed nodes can be calculated by Eq. 4.36, where $\mathbf{x_d^n}$ is the position of the departed nodes, $\mathbf{x^{n+1}}$ is the current mesh nodes position and $\mathbf{u^n}$ the current velocity.

$$\mathbf{x_d^n} = \mathbf{x^{n+1}} - \mathbf{u^n}\Delta t \tag{4.36}$$

After calculating the departed node position $\mathbf{x_d^n}$, it is necessary to calculate the variable value at this position α_d^n. This calculation is made by interpolating the α^n values at the nodes of the element which contains $\mathbf{x_d^n}$. So, first is necessary to find the element where the departed position is located.

In order to find this element, a search procedure is carried out. This procedure works firstly by locating the elements which contain the position of the current node $\mathbf{x^{n+1}}$. After that, it is calculated which of these elements is closest to $\mathbf{x_d^n}$ by using area coordinates. Then, if the found element does not contain $\mathbf{x_d^n}$, its neighboring elements are located and it is calculated the one which is closest to $\mathbf{x_d^n}$. Furthermore, this process is carried out repeatedly until it is found the element containing $\mathbf{x_d^n}$.

There is a special case for this method that occurs when the departed node position is out of the problem domain. In this situation there is no element containing the departed node position, making it impossible to use the presented approach to calculate the variable value at the departure position. So, in this situation, the departure position variable value is adopted to be such as the one defined by the boundary condition of the closest boundary to the departure position.

Figure 4.2 presents a schematic representation of this procedure. In the figure, it is shown the current node position $\mathbf{x^{n+1}}$ and the departed node position $\mathbf{x_d^n}$ with a red arrow representing the node displacement calculated by $-\mathbf{u^n}\Delta t$. Besides that, the grey elements are the elements that the searching procedure needs to pass through until found the element containing the departed node is. Therefore, it is possible to realize that only a few elements need to be tracked to find the aimed one, reducing the computational effort.

Finally, it is possible to apply the semi-Lagrangian method to discretize the remaining temporal term in the governing equations. Then, after applying the method on Eq. 4.23, Eq. 4.24, and 4.25, the following discretized equations are obtained and can be used to solve the problem:

$$\left(\frac{[M]}{\Delta t'} + \frac{[K]}{Re} + (Di_1 + Di_2[U])[M]\right)\{u_1^{n+1}\} - [G_x]\{p\} = \frac{[M]}{\Delta t'}\{u_{1d}^n\} + \frac{1}{Fr^2}[M]\{g_1\} \tag{4.37}$$

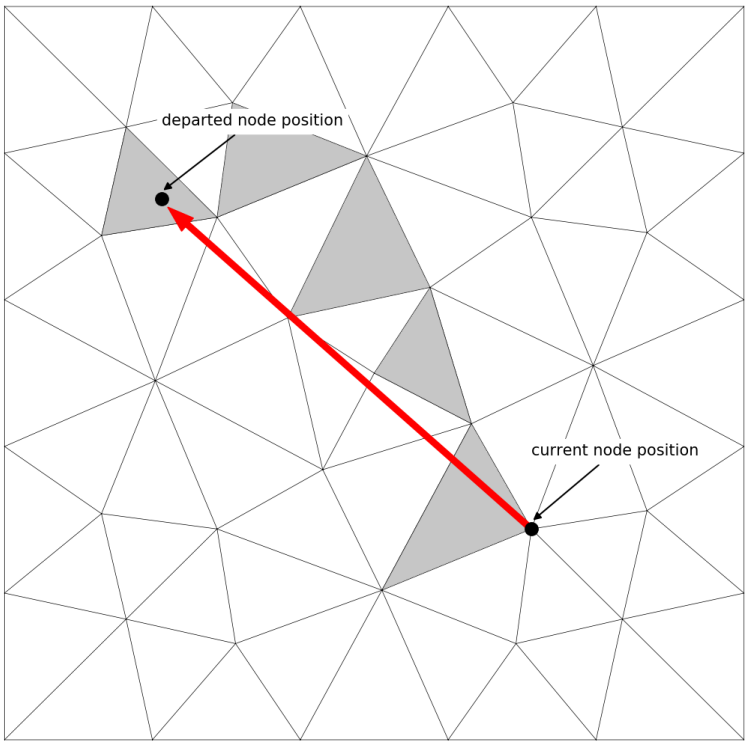

Figure 4.2: Schematic representation of the searching procedure used in the semi-Lagrangian method to find the element containing the departed node position.

$$\left(\frac{[M]}{\Delta t'} + \frac{[K]}{Re} + (Di_1 + Di_2[U])[M]\right)\{u_2^{n+1}\} - [G_y]\{p\} = \frac{[M]}{\Delta t'}\{u_{2d}^{n}\} + \frac{1}{Fr^2}[M]\{g_2\} \tag{4.38}$$

$$\left(\frac{[M]}{\Delta t'} + \frac{[K]}{Re} + (Di_1 + Di_2[U])[M]\right)\{u_3^{n+1}\} - [G_z]\{p\} = \frac{[M]}{\Delta t'}\{u_{3d}^{n}\} + \frac{1}{Fr^2}[M]\{g_3\} \tag{4.39}$$

Where $[M]$ is the mass matrix, $[K]$ is the stiffness matrix, $[U]$ is a diagonal matrix containing the velocity module value at time step n, $[G_x]$, $[G_y]$, and $[G_z]$ are part of the gradient matrix related to, respectively, x_1, x_2, and x_3 direction. Moreover, $\{u_1^{n+1}\}$, $\{u_2^{n+1}\}$, and $\{u_3^{n+1}\}$ are the vectors of velocity at x_1, x_2, and x_3 direction, respectively, at time step $n+1$, $\{u_{1d}^{n+1}\}$, $\{u_{2d}^{n+1}\}$, and $\{u_{3d}^{n+1}\}$ are the vector of velocity at x_1, x_2, and x_3 direction, respectively, at the departed node position in the time step n, $\{p\}$ is the pressure vector and $\{g_1\}$, $\{g_2\}$, and $\{g_3\}$ are the gravity vectors at x_1, x_2, and x_3 direction, respectively. Finally, $\Delta t'$ is the dimensionless time variation, Re is the Reynolds number, Di_1 and Di_2 are two dimensionless groups defined by Eq. 3.10 and Eq. 3.11, respectively, and Fr is the Freud number.

4.2 Runge-Kutta Method

Runge-Kutta methods are a family of numerical methods used to solve ordinary differential equations that have the form of $\frac{dy}{dx} = f(x, y)$. This method is based on Taylor series, but with no need for higher derivatives calculation. The most popular of these methods is the Fourth-Order Runge-Kutta, which will be the one used in this work [37].

The most common form of the Fourth-Order Runge-Kutta, which is the one used in this work, is presented by Eq. 4.40, where y and x are related to the ordinary differential equations form mentioned in the previous paragraph, h is the difference between steps and the subscript i refers to the steps.

$$\begin{aligned} y_{i+1} &= y_i + \frac{h}{6}(k_1 + 2k_2 + 2k_3 + k_4) \\ k_1 &= f(x_i, y_i) \\ k_2 &= f\left(x_i + \frac{h}{2}, y_i + \frac{h}{2}k_1\right) \\ k_3 &= f\left(x_i + \frac{h}{2}, y_i + \frac{h}{2}k_2\right) \\ k_4 &= f(x_i + h, y_i + k_3 h) \end{aligned} \tag{4.40}$$

Then, it is possible to apply the Fourth-Order Runge-Kutta in the particle motion equation, presented by Eq. 3.18, and the new equation that will be solved after the method application, is presented by Eq. 4.41.

$$\begin{aligned} v'^{n+1}_i &= v'^{n}_i + \frac{\Delta t'}{6}(k_1 + 2k_2 + 2k_3 + k_4) \\ k_1 &= \frac{18\mu L}{d^2 C_c \rho_p U_c}(u'^{n}_i - v'^{n}_i) + \frac{G_i}{U_c}\sqrt{\frac{L\pi S_0}{U_c \Delta t'}} + \frac{g'_i}{Fr^2} \\ k_2 &= \frac{18\mu L}{d^2 C_c \rho_p U_c}\left(u'^{n}_i - v'^{n}_i - \frac{\Delta t'}{2}k_1\right) + \frac{G_i}{U_c}\sqrt{\frac{L\pi S_0}{U_c \Delta t'}} + \frac{g'_i}{Fr^2} \\ k_3 &= \frac{18\mu L}{d^2 C_c \rho_p U_c}\left(u'^{n}_i - v'^{n}_i - \frac{\Delta t'}{2}k_2\right) + \frac{G_i}{U_c}\sqrt{\frac{L\pi S_0}{U_c \Delta t'}} + \frac{g'_i}{Fr^2} \\ k_4 &= \frac{18\mu L}{d^2 C_c \rho_p U_c}(u'^{n}_i - v'^{n}_i - \Delta t' k_3) + \frac{G_i}{U_c}\sqrt{\frac{L\pi S_0}{U \Delta t'}} + \frac{g'_i}{Fr^2} \end{aligned} \tag{4.41}$$

Moreover, the most important particle feature, in this case, is its position. Therefore, after the calculation of the particle velocity, it is necessary to calculate its position through Eq. 4.42, where x'_p is the particle position in its dimensionless form and subscript i refers to the main directions of the problem.

$$\frac{dx'_{p_i}}{dt'} = v'_i \tag{4.42}$$

Then, it applies Fourth-Order Runge-Kutta again in Eq. 4.42, and Eq. 4.43 is obtained to solve approximately the particle position based on its velocity that was already calculated.

$$x'^{\,n+1}_{p_i} = x'^{\,n}_{p_i} + \Delta t' \left(\frac{v'^{n+1}_i - v'^{n}_i}{2} \right) \tag{4.43}$$

Chapter 5

Code Verification

Since it has been used in-house codes to run the simulations in this work, it is necessary to verify them to guarantee that the results provided are reliable. In order to do that, they were used to run some cases found in the literature and the results obtained in this work and in the literature were compared.

Firstly, it was carried out simulations for problems that only have a fluid domain, ensuring that the code is capable to solve the classical Navier-Stokes equations. After that, it was simulated a case that also comprises a porous domain, verifying the code for a problem with both regions. This verification process was made for two-dimensional and three-dimensional problems.

5.1 Two-Dimensional

5.1.1 Plane Poiseuille Flow

The plane Poiseuille flow may be one of the simplest and most famous fluids mechanics cases. This case consists of a flow between two parallel flat plates where the inlet velocity is constant and parallel to the plates. This problem is presented schematically in Figure 5.1 and its boundary conditions are constant velocity at the inlet of the domain's left, null velocity condition at the top and bottom plates, and null pressure condition in the outlet located on the right. The boundaries are indicated in the figure and their respective conditions are mathematically defined in Table 5.1.

Boundary	Horizontal Velocity	Vertical Velocity	Pressure
Inlet	$u_1 = 1$	$u_2 = 0$	$\nabla P \cdot \mathbf{n} = 0$
Wall	$u_1 = 0$	$u_2 = 0$	$\nabla P \cdot \mathbf{n} = 0$
Outlet	$\nabla u_1 \cdot \mathbf{n} = 0$	$\nabla u_2 \cdot \mathbf{n} = 0$	$P = 0$

Table 5.1: Boundary Conditions of the Plane Poiseuille problem.

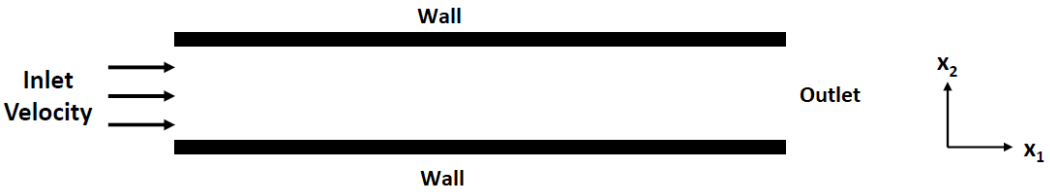

Figure 5.1: Schematic representation of Plane Poiseuille Flow case.

Simulations were carried out for a plane Poiseuille flow case with $Re = 1000$ and the gravity term neglected. It was run simulations using the MINI and the quadratic elements (see Sec 4.1.3 for more details). For the MINI's case, it was used a mesh with 31110 triangle elements, 16176 pressure nodes, and 47286 velocity nodes, while for the quadratic case, it was used 20888 triangle elements, 10865 pressure nodes, and 42617 velocity nodes.

Then, the horizontal velocity in the fully developed region results obtained for each case was plotted along with the analytical solution, which can be found at the work of BATCHELOR [30]. These results are shown in Figure 5.2, where it is possible to see that both simulation results are close to the analytical solution and that the quadratic element had provided results even closer to the analytical solution, despite using a mesh with a smaller amount of elements and nodes.

Since this is a simple case to simulate, it would be expected that the simulation results were closer to the analytical solution in such a way that the graphic curves should be overlapping each other. However, this agreement was not reached due to the boundary conditions imposed in the inlet. The constant velocity condition was imposed in the domain's inlet but with the interception points of the inlet and the plates having a wall condition applied to them. Then, the simulated cases hadn't the same mass influx than it was considered in the analytical solution, which lead to the error that can be observed in the figure.

5.1.2 Lid Driven Flow

The lid driven case consists in a square cavity where the top surface moves with a constant velocity while the other surfaces remain stationary. This problem is presented schematically in Figure 5.3 and its boundary conditions are constant velocity on the top surface and wall condition on the other surfaces. Moreover, a boundary condition of null pressure in the bottom right corner was also used in the simulations. The boundaries are indicated in the figure and their respective conditions are mathematically defined in Table 5.2.

This case was simulated for $Re = 10$, $Re = 100$, and $Re = 1000$ with the gravity term neglected using triangle MINI and quadratic elements. Then, the results obtained by these simulations were compared with the results provided by

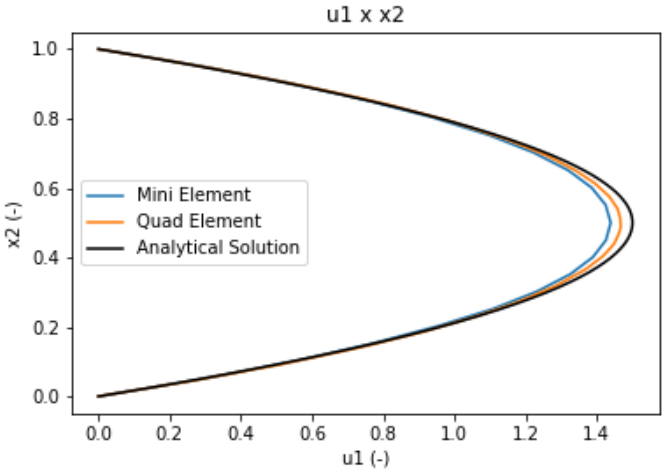

Figure 5.2: Comparison between simulation and analytical results for Plane Poiseuille Flow case.

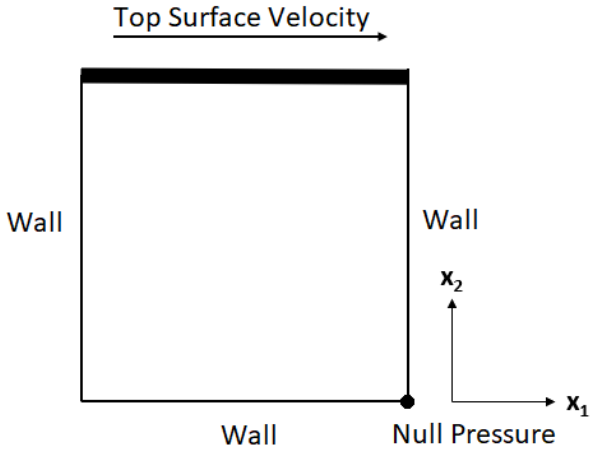

Figure 5.3: Schematic representation of Lid Driven Flow case.

Boundary	Horizontal Velocity	Vertical Velocity	Pressure
Top Surface	$u_1 = 1$	$u_2 = 0$	$\nabla P \cdot \mathbf{n} = 0$
Wall	$u_1 = 0$	$u_2 = 0$	$\nabla P \cdot \mathbf{n} = 0$
Null Pressure	$\nabla u_1 \cdot \mathbf{n} = 0$	$\nabla u_2 \cdot \mathbf{n} = 0$	$P = 0$

Table 5.2: Boundary Conditions of the Lid Driven Flow problem.

the work of MARCHI *et al* [38].

Firstly, for the $Re = 10$ case, the mesh with MINI elements had 6624 triangle elements, 3413 pressure nodes, and 10037 velocity nodes, while the mesh with quadratic elements had the same amount of triangle elements and pressure nodes, but with 13449 velocity nodes since edge nodes are present in such a high-order element. The results of both simulations in comparison with the reference results are presented in Figure 5.4 where it is possible to see that they are in good agreement. Moreover, it is also possible to see that the quadratic mesh has provided results closer to the reference than the MINI mesh using the same amount of elements, but with more velocity nodes, which means more computational effort.

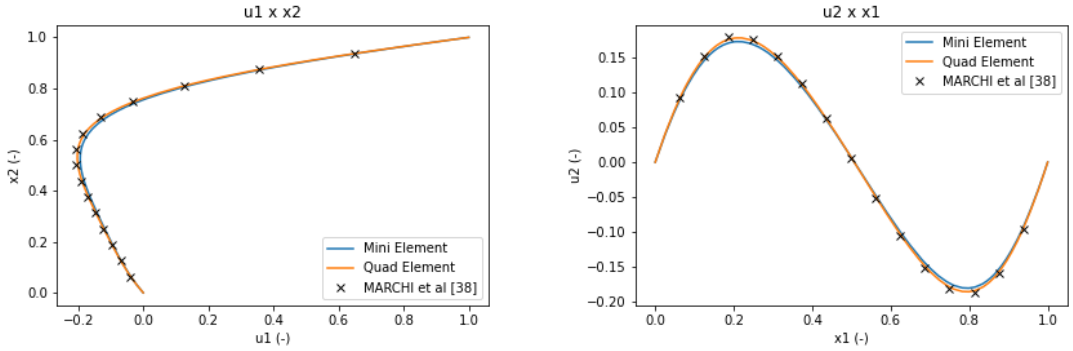

(a) u_1 along x_2 for $x_1 = 0.5$.

(b) u_2 along x_1 for $x_2 = 0.5$.

Figure 5.4: Results obtained by simulations and literature for $Re = 10$ for the Lid Driven Flow case.

Then, for the $Re = 100$ case, it was used the same meshes that were used for $Re = 10$. The results are presented in Figure 5.5 and once more time it is possible to see a good agreement between them with the quadratic element providing results closer to the reference.

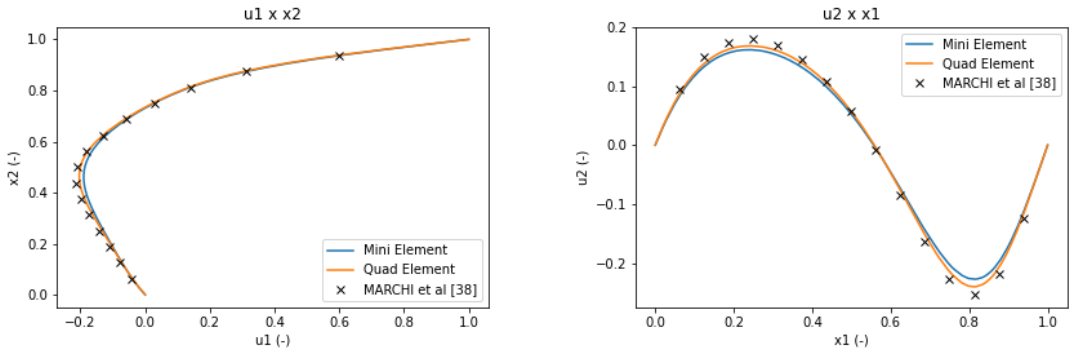

(a) u_1 along x_2 for $x_1 = 0.5$.

(b) u_2 along x_1 for $x_2 = 0.5$.

Figure 5.5: Results obtained by simulations and literature for $Re = 100$ for the Lid Driven Flow case.

Finally, for the $Re = 1000$ case, it was used a mesh with MINI elements containing 105584 elements, 53193 pressure nodes, and 158777 velocity nodes, and a mesh with quadratic elements containing 26426 elements, 13414 pressure nodes, and 53253 velocity nodes. The results are presented in Figure 5.6, where it is possible to see that the MINI elements mesh provided results that deviate from the literature in some regions while the quadratic elements mesh does not. Besides that, the quadratic elements mesh has fewer elements and nodes than the MINI elements mesh. So, for this case, the quadratic element provides more accurate results with a lower computational effort.

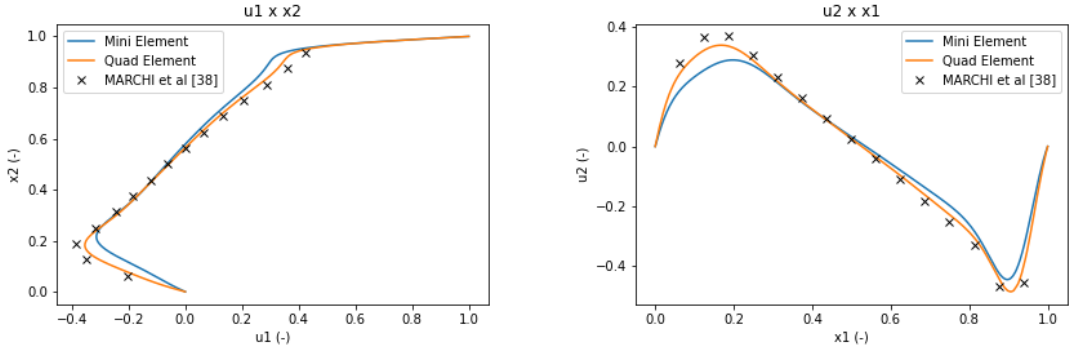

(a) u_1 along x_2 for $x_1 = 0.5$.

(b) u_2 along x_1 for $x_2 = 0.5$.

Figure 5.6: Results obtained by simulations and literature for $Re = 1000$ for the Lid Driven Flow case.

5.1.3 Flow over Porous Region

This case consists of a flow entering a fluid region that is located upon a porous medium and, then, it exits at both the fluid region and porous medium. Figure 5.7 presents schematically this problem while Table 5.3 shows the boundary conditions of each domain's boundary, which are indicated in the figure.

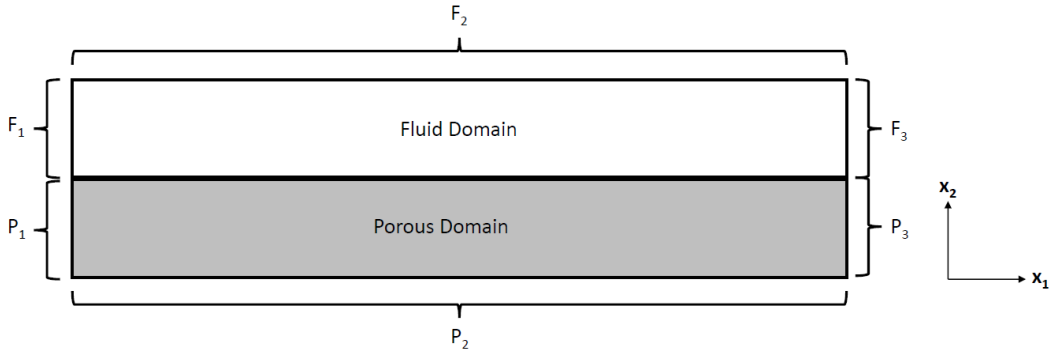

Figure 5.7: Schematic representation of the flow over porous region problem.

Boundary	Horizontal Velocity	Vertical Velocity	Pressure
F_1	$u_1 = y(4-y)$	$\nabla u_2 \cdot \mathbf{n} = 0$	$\nabla P \cdot \mathbf{n} = 0$
F_2	$u_1 = 0$	$u_2 = 0$	$\nabla P \cdot \mathbf{n} = 0$
F_3	$\nabla u_1 \cdot \mathbf{n} = 0$	$\nabla u_2 \cdot \mathbf{n} = 0$	$P = 0$
P_1	$u_1 = 0$	$\nabla u_2 \cdot \mathbf{n} = 0$	$\nabla P \cdot \mathbf{n} = 0$
P_2	$\nabla u_1 \cdot \mathbf{n} = 0$	$u_2 = 0$	$\nabla P \cdot \mathbf{n} = 0$
P_3	$\nabla u_1 \cdot \mathbf{n} = 0$	$\nabla u_2 \cdot \mathbf{n} = 0$	$P = 0$

Table 5.3: Boundary Conditions of the flow over a porous region problem.

The simulations were carried out for $Re = 6.38$, $Fr = 10^2$, $Di_1 = 0.42$ and $Di_2 = 0.82$ using MINI and quadratic elements. The mesh with MINI elements has 92418 elements, 46780 pressure nodes, and 139198 velocity nodes, while the quadratic mesh has 22834 elements, 11703 pressure nodes, and 46239 velocity nodes. Finally, it was possible to compare the simulation results with the results of CIMOLIN AND DISCACCIATI [13].

Figure 5.8 presents the results of simulations and the reference work for the horizontal velocity at the problem's outlet and the vertical velocity along the interface between the fluid and porous regions. Looking at the figure, firstly, it is possible to see that the results of simulations with both element types are in good agreement with the literature for horizontal velocity. However, it is possible to see a disagreement between the simulation results and the reference for the vertical velocity in the entry region of the domain. This disagreement can be explained by the fact that the interface is usually a complicated region which can bring some numerical errors.

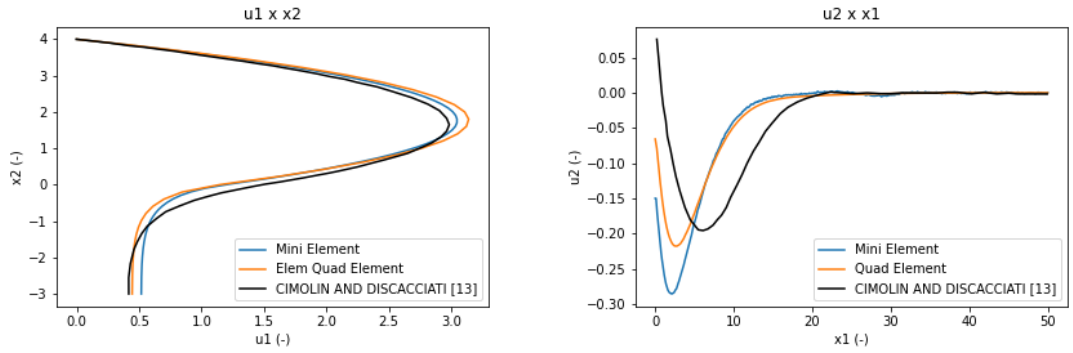

(a) u_1 along x_2 at the outlet.

(b) u_2 along x_1 at the interface.

Figure 5.8: Results obtained by simulations and literature for the flow over porous region problem.

Then, it is possible to conclude that, despite the errors in the interface of the problem, the code provides accurate results. However, an investigation of some improvements that can be done in the code to achieve a better solution for the interface region would be interesting to be done in the future. Another important

adjustment that can be done is to make some refinements in the mesh in the interface.

5.2 Three-Dimensional

5.2.1 Hagen-Poiseuille

The Hagen-Poiseuille case is another fluid mechanic's classic problem, which consists of a flow inside a long tube with a circular section. This case is presented in Figure 5.9 and its boundary conditions are constant velocity at the inlet, null pressure at the outlet, and no-slip and non-penetrating condition on the wall. The boundaries are indicated in the figure and their respective conditions are mathematically defined in Table 5.4.

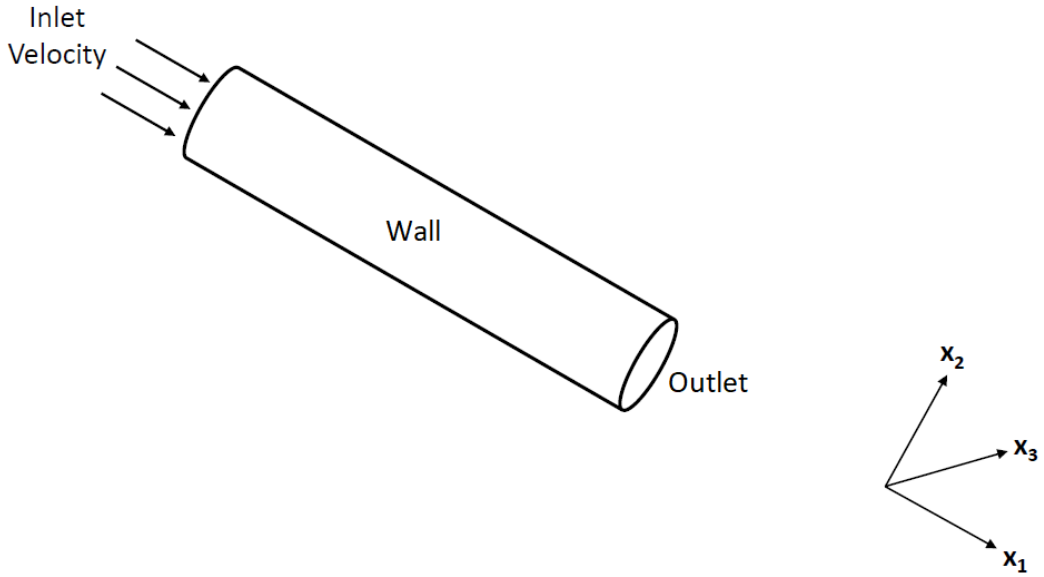

Figure 5.9: Schematic representation of the Hagen-Poiseuille case.

Boundary	u_1	u_2	u_3	P
Inlet	$u_1 = 1$	$u_2 = 0$	$u_3 = 0$	$\nabla P \cdot \mathbf{n} = 0$
Wall	$u_1 = 0$	$u_2 = 0$	$u_3 = 0$	$\nabla P \cdot \mathbf{n} = 0$
Outlet	$\nabla u_1 \cdot \mathbf{n} = 0$	$\nabla u_2 \cdot \mathbf{n} = 0$	$\nabla u_3 \cdot \mathbf{n} = 0$	$P = 0$

Table 5.4: Boundary Conditions of the Hagen-Poiseuille problem.

A simulation was carried out for this case for $Re = 10$ and with the gravity term neglected. The mesh used for this simulation was made by tetrahedron MINI elements and had 482488 tetrahedron elements, 88188 pressure nodes, and 570676 velocity nodes.

Then, the results obtained in this simulation for the axial velocity in the fully developed region are plotted along with the analytical solution, which can be found at the work of BATCHELOR [30], in Figure 5.10. In this figure, it is possible to see that both results are in good agreement. Moreover, it is possible to see that there is a undershoot of the simulation results in comparison with the analytical solution.

This error can be explained in the same way that was done for the Plane Poiseuille case. The constant velocity condition was applied at the entire problem's inlet except for the inlet's contour, where there is an interception between the inlet and the wall of the domain and where it was applied the null velocity condition. Then, the mass influx of the simulated case is not exactly the same that the one considered in the analytical solution.

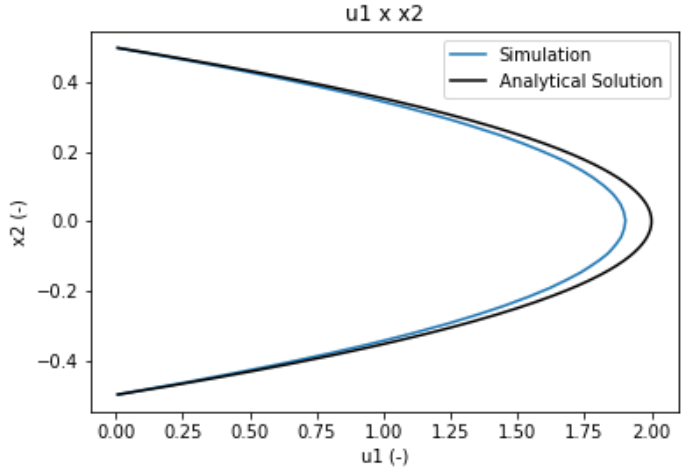

Figure 5.10: Comparison between simulation and analytical results for Hagen-Poiseuille case.

5.2.2 Square Duct with a Moving Top Wall

This case consists of a duct with a square cross-section and with its top wall moving at a constant velocity. Figure 5.11 shows schematically this problem with its boundary conditions of constant velocity in the inlet, null pressure in the outlet, constant velocity in the top surface with the same value as the inlet velocity, and wall condition in the remaining surfaces. The boundaries are indicated in the figure and their respective conditions are mathematically defined in Table 5.5.

A case with the gravity term neglected and $Re = 10$ was simulated with a mesh made by tetrahedron MINI elements. This mesh has 343630 elements, 64331 pressure nodes, and 407961 velocity nodes.

Figure 5.12 shows the isolines of the velocity at the x_1 direction in the fully developed region that was provided by the simulation in comparison with the ones

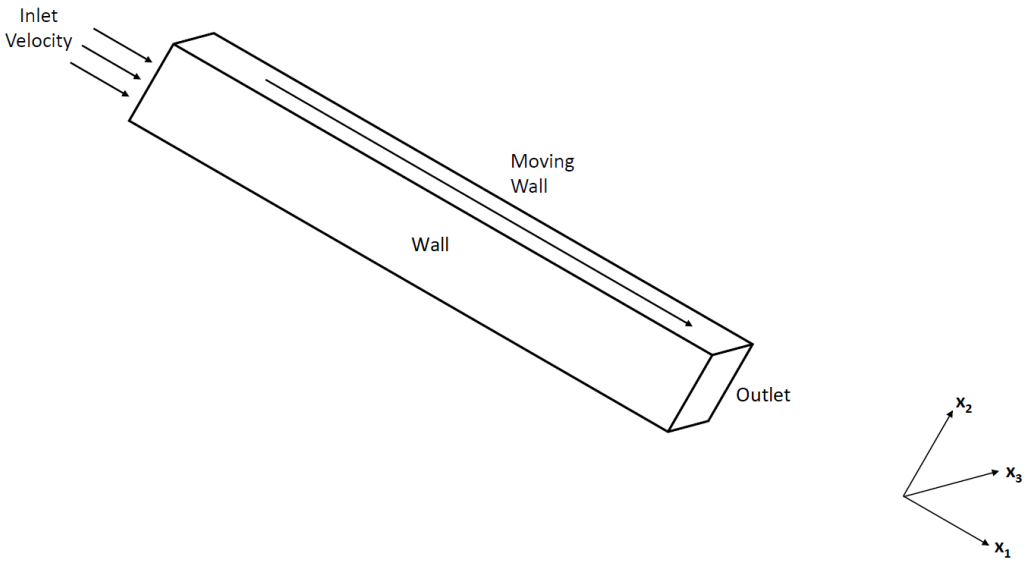

Figure 5.11: Schematic representation of the square duct with a moving top wall problem.

Boundary	u_1	u_2	u_3	P
Inlet	$u_1 = 1$	$u_2 = 0$	$u_3 = 0$	$\nabla P \cdot \mathbf{n} = 0$
Moving Wall	$u_1 = 1$	$u_2 = 0$	$u_3 = 0$	$\nabla P \cdot \mathbf{n} = 0$
Wall	$u_1 = 0$	$u_2 = 0$	$u_3 = 0$	$\nabla P \cdot \mathbf{n} = 0$
Outlet	$\nabla u_1 \cdot \mathbf{n} = 0$	$\nabla u_2 \cdot \mathbf{n} = 0$	$\nabla u_3 \cdot \mathbf{n} = 0$	$P = 0$

Table 5.5: Boundary Conditions of the Square Duct with a Moving Top Wall problem.

found in the work of OWOLABI [39]. In the figure, the results are presented for a velocity range of 0.3 to 1.5 with increments of 0.3. Moreover, the X marks represent the simulation results while the lines represent the results of the reference work. Then, it is possible to see that the results are in good agreement.

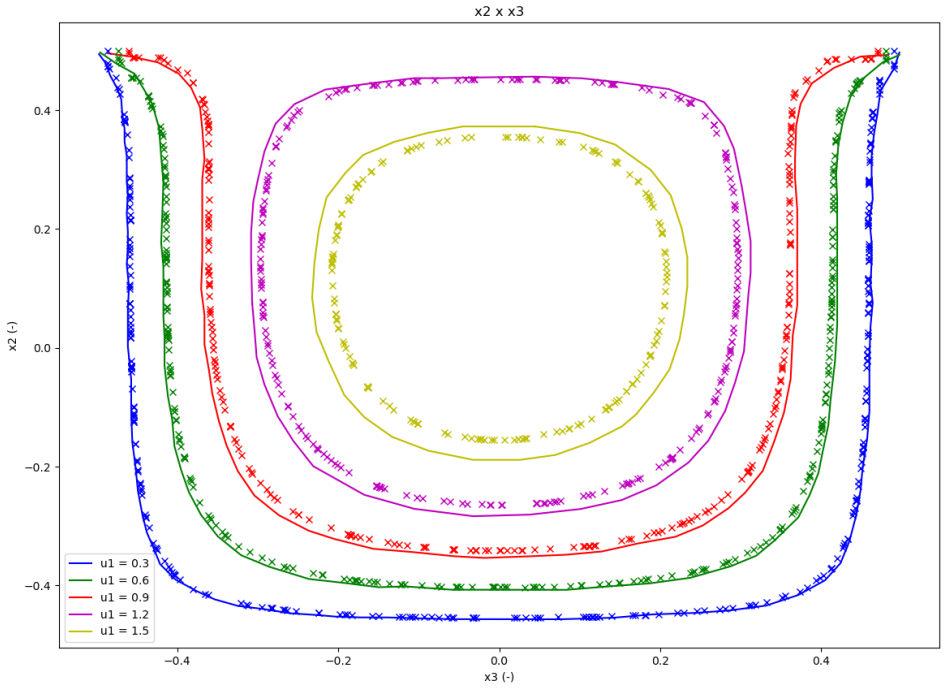

Figure 5.12: Comparison between simulation and reference results for the square duct with moving top wall problem.

5.2.3 Flow over Porous Region

This case consists of an adaptation of the problem with the same name in the two-dimensional section for a three-dimensional case. Then, the problem is equal to the other one, with extrusion of the original domain in the x_3 direction and with boundary conditions of symmetry in the surfaces in this direction.

The simulations were carried out for the same parameters as the two-dimensional case ($Re = 6.38$, $Fr = 10^2$, $Di_1 = 0.42$, and $Di_2 = 0.82$) using a mesh with tetrahedron MINI elements. The mesh has 2368597 elements, 437319 pressure nodes, and 2805916 velocity nodes.

Figure 5.8 presents the results of simulations and the reference work, which is the same one that was used in the two-dimensional case, for the horizontal velocity at the problem's outlet and the vertical velocity along the interface between the fluid and porous regions at the center of the domain in the x_3 direction. It is possible to

see that the results are in good agreement with the literature for horizontal velocity, while there is some disagreement between the results for the vertical velocity in the interface in the same way that also had in the two-dimensional case. This difference can be once again explained by the fact that the interface is a region that causes numerical errors. It would be interesting to search for other methods that can mitigate this problem in the future.

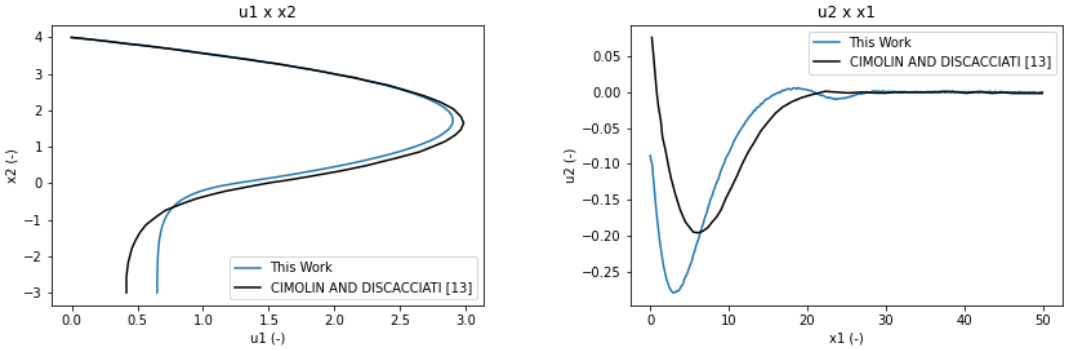

(a) u_1 along x_2 at the outlet.

(b) u_2 along x_1 at the interface.

Figure 5.13: Results obtained by simulations and literature for the three-dimensional flow over porous region problem.

Chapter 6

DPF Simulations

After the computational code has been verified, it is possible to use it to simulate the flow inside a DPF, which is this work's main goal. Then, in this chapter, it will be shown the model used and the results that were obtained for these simulations. This information will be presented separately for the two-dimensional and three-dimensional cases.

6.1 Two Dimensional

6.1.1 Case Set-Up

The DPF consists of many channels disposed of in a regularly spaced arrangement and, because of that, it is possible to model this device taking only into account two halves of channels. This simplification can be made due to the symmetry of the problem, which can be imposed in these two channels by applying symmetry conditions on the boundaries.

Then, the model which will be simulated is formed by half of a channel where the air enters, which is located at the top, half of a channel where the air goes out, which is located at the bottom, and the porous wall that separates these channels. The top channel is going to be called the inlet channel while the bottom channel will be called the outlet channel.

Moreover, it is necessary to model not only the DPF itself but also two other regions along with it, which are going to be called the inlet zone and outlet zone. The addition of these zones is necessary since it would be difficult to set the boundary conditions at the inlet and outlet of the device. Then, after this inclusion, it is possible to set the constant velocity condition far before the DPF and the null pressure condition far after it.

Figure 6.1 presents schematically the model used to simulate the DPF in two dimensions. In this figure, it is indicated the porous domain, which is constituted

by the porous wall located between two adjacent channels, and the fluid domain, where there is no porous material. Besides that, it is also indicated which model part is related to the device itself and which parts are the inlet and outlet zones. The plugs are also presented in the figure. Finally, the greek letter delta indicates the boundaries of the model.

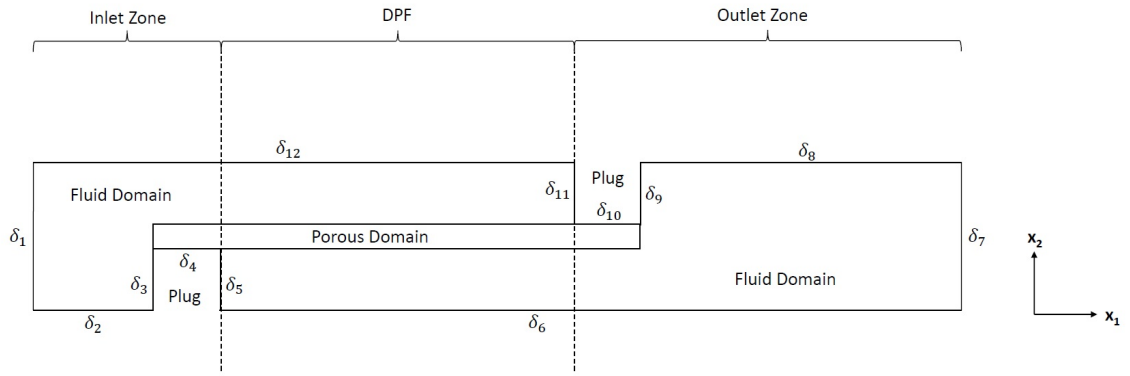

Figure 6.1: Two-Dimensional DPF Model.

Table 6.1 presents the boundary conditions applied to the problem. It is presented in this table the type of the boundary condition and its mathematical definition for each boundary indicated in Figure 6.1.

Type	Boundaries	u_1	u_2	P
Inlet	δ_1	$u_1 = 1$	$u_2 = 0$	$\nabla P \cdot \mathbf{n} = 0$
Symmetry	δ_2, δ_6, δ_8, δ_{12}	$\nabla u_1 \cdot \mathbf{n} = 0$	$u_2 = 0$	$\nabla P \cdot \mathbf{n} = 0$
Wall	δ_3, δ_4, δ_5, δ_9, δ_{10}, δ_{11}	$u_1 = 0$	$u_2 = 0$	$\nabla P \cdot \mathbf{n} = 0$
Outlet	δ_7	$\nabla u_1 \cdot \mathbf{n} = 0$	$\nabla u_2 \cdot \mathbf{n} = 0$	$P = 0$

Table 6.1: Boundary Conditions of the two-dimensional DPF model.

6.1.2 Case 1: Air flow

The first DPF case that was simulated was based on the work of KONSTANDOPOULOS *et al* [25], which had simulated only the air flow using the Navier-Stokes equations along with the Darcy and Forchheimer terms. In this case, it was only taken into account the air flow inside the device, not considering the particulates. Then, the parameters that were adopted for this simulation are presented in Table 6.2

After looking at the parameters of the problem, it is important to define the characteristic length and velocity. In this case, the characteristic velocity is going to be the inlet velocity while the characteristic length is the channel width. Therefore, this problem has $Re \approx 951$, confirming that the flow is laminar. Besides that, the problem also has $Fr \approx 172$.

Parameter	Value
Inlet Velocity (m/s)	24.8
Density (kg/m^3)	0.54
Dynamic Viscosity (Pa.s)	2.97 x 10^{-5}
Permeability (m^2)	2 x 10^{-13}
Inertial Resistance Coefficient (-)	223.1
Channel Width (mm)	2.11
Channel Length (mm)	304.8
Porous Wall Thickness (mm)	0.432

Table 6.2: Parameters used in the simulation of Case 1.

After the definition of the parameters, it is necessary to set the computational mesh. The mesh was obtained using Gmsh, which is an open-source software that generates finite element meshes.

Since it was carried out simulations using the MINI and quadratic triangle elements, it was used two different meshes. In this case, both meshes used the same elements with a difference in the number of nodes for velocity, with one extra node for velocity in the centroids of the elements for the MINI mesh and three extra nodes for velocity in the elements midpoints for the quadratic mesh. Then, both meshes have 296434 elements and 154501 nodes for pressure. However, while the mesh with MINI elements has 450935 nodes for velocity, the mesh with quadratic elements has 605435.

The problem domain is very long and, because of that, it would be difficult to present the mesh in detail along all of it. Then, Figure 6.2 shows in detail the mesh used for the simulations at the DPF's inlet. This mesh is the same for MINI and quadratic elements, with the difference of the nodes located at the centroid or at the midpoints, which are not presented in the figure.

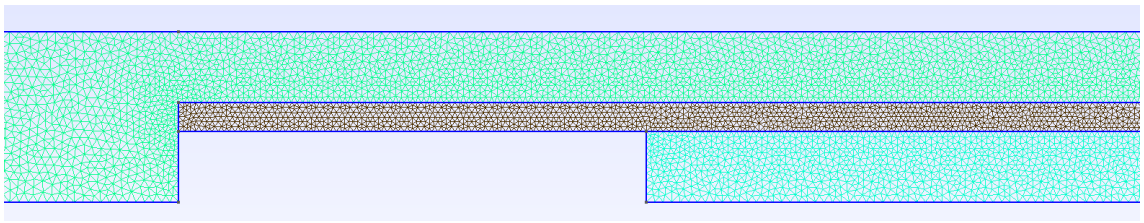

Figure 6.2: Mesh at the inlet of the DPF in Case 1.

Figure 6.3 presents in detail the mesh at the DPF's outlet. It is important to say again that this mesh is the same for MINI and quadratic elements, with the difference in the velocity nodes that not appears.

In two-dimensional CFD simulations, it is a common practice to use rectangular elements in the boundary layer regions. Then, in this case, it would be interesting to use these elements near the plugs and in the porous wall. However, the use

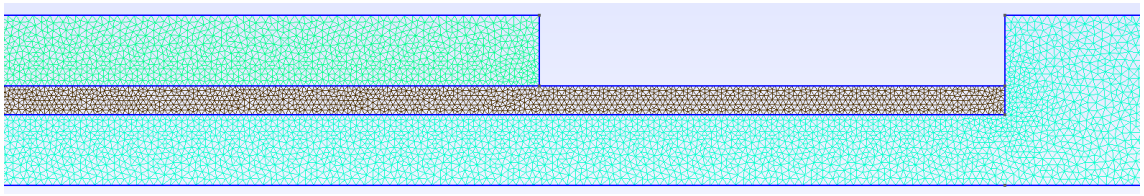

Figure 6.3: Mesh at the outlet of the DPF in Case 1.

of rectangle elements along with the triangle elements would add complexity to the code and, in this work, it was chosen to use only triangle elements to avoid this problem knowing that they are also able to provide good results even though it would probably need a more refined mesh in comparison with a mesh with rectangles and triangles to get converged results.

After the mesh definition, it was possible to run the simulations and get some results. Since the DPF is very long, the results will be presented in detail at the device's inlet and outlet. Moreover, since the results that were obtained for both meshes are qualitatively similar, it is shown only one of them, the results obtained with the MINI mesh. The results obtained with the quadratic mesh are presented in the appendix. It was used Paraview, an open-source post-processing software, to visualize the simulation results.

Figure 6.4 presents the results for the horizontal velocity, which is the velocity in the x_1 direction, at the inlet region. In this figure, it is possible to see that the horizontal velocity at the inlet channel decreases along the channel while the velocity at the outlet channel, which is zero next to the plug, increases. This situation occurs because the air is going from the inlet to the outlet channel through the porous wall.

Figure 6.4: Horizontal velocity at DPF's inlet in Case 1.

Figure 6.5 presents the results for the horizontal velocity at the DPF's outlet. In this figure, it is possible to see that the velocity had decreased a lot in comparison with the velocity observed at the device's inlet, presented in Figure 6.4, reaching zero next to the plug. The explanation for that is the airflow through the porous wall. Besides that, it is also possible to see that the velocity at the outlet channel has increased due to the same reason.

Figure 6.6 presents the results for pressure at the DPF's inlet. It is possible to see that the pressure at the inlet channel is much higher than the pressure at the outlet channel. This happens because it occurs a great pressure loss when the air

Figure 6.5: Horizontal velocity at DPF's outlet in Case 1.

goes through the porous wall.

Figure 6.6: Pressure at DPF's inlet in Case 1.

Figure 6.7 presents the results for pressure at the DPF's outlet. It is possible to see the difference between the pressure at both channels that was mentioned before. Besides that, it is also possible to note that the pressure at the inlet channel has increased while it has decreased at the outlet channel in comparison with the pressure at DPF's inlet, presented in Figure 6.6.

Figure 6.7: Pressure at DPF's outlet in Case 1.

In order to validate the results that were obtained, they were compared with the results of the reference work for the axial velocity and wall velocity. The axial velocity consists of the velocity in the horizontal direction at the channel center while the wall velocity is the velocity in the transversal direction inside the porous wall.

Figure 6.8 shows the results for the dimensionless axial velocity along the inlet and outlet channels that were obtained in this work using meshes with MINI and quadratic elements and the ones obtained in the reference work. It is important to know that the dimensionless axial velocity is the axial velocity divided by the axial velocity at the DPF's entry while the dimensionless channel length is the length divided by the device's total length.

Then, it is possible to see that, despite a difference between the results, all of them have a linear behavior. This fact may make it possible to think that the simulation

is working fine but need a more refined mesh to be more accurate. The fact that the meshes with MINI and quadratic elements had close results may indicate a convergence of results, but it would be interesting to use more refined meshes in the future to verify that.

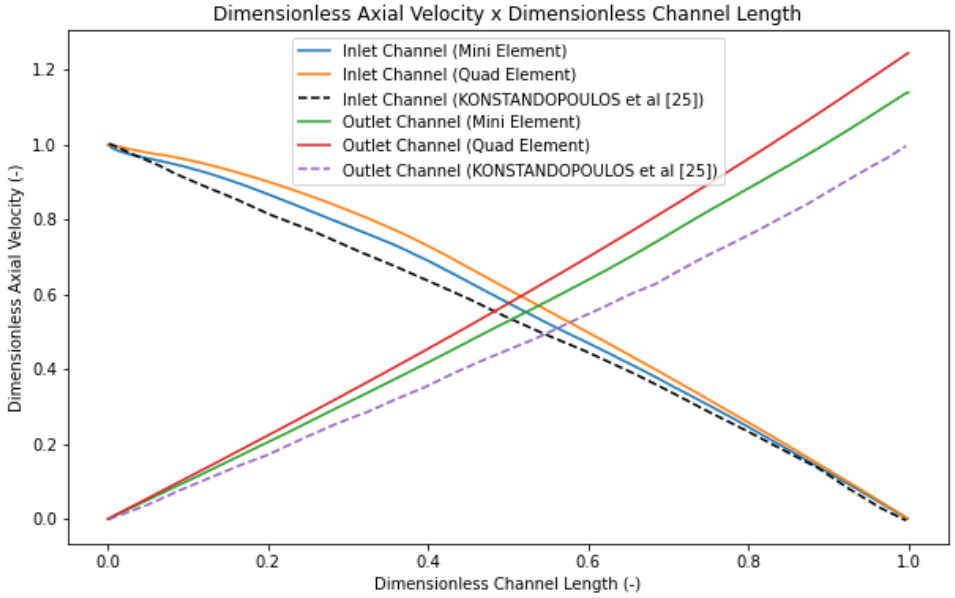

Figure 6.8: Axial velocity along the inlet and outlet channels at Case 1.

Figure 6.9 shows the results that were obtained for the dimensionless wall velocity along the channel in this work, using two different meshes, and in the reference work. The dimensionless wall velocity is defined according to KONSTANDOPOULOS *et al* [25] as presented by Eq. 6.1, where u'_w is the dimensionless wall velocity, L is the DPF's total length, U_{in} is the velocity at DPF's entry, W is the channel width and u_w is the wall velocity, which consists of the vertical velocity inside the porous wall.

$$u'_w = \frac{4L}{U_{in}W}|u_w| \tag{6.1}$$

Looking at Figure 6.9 it is possible, firstly, to see that the simulations carried out in this work had results with a good agreement between the two meshes used, which may indicate that the results are converging. Besides that, it is also possible to see that the wall velocity obtained in this work has a similar profile to the one obtained in the reference work, despite the higher values of this work velocity, which may indicate that the applied method works fine but need more refined meshes.

The higher values that this work results have in comparison with the literature ones can also be explained by the three-dimensional effects that were only taken into account in the reference work, by the gravitational effects that were only taken into account in this work, or just by numerical errors. Another possible explanation

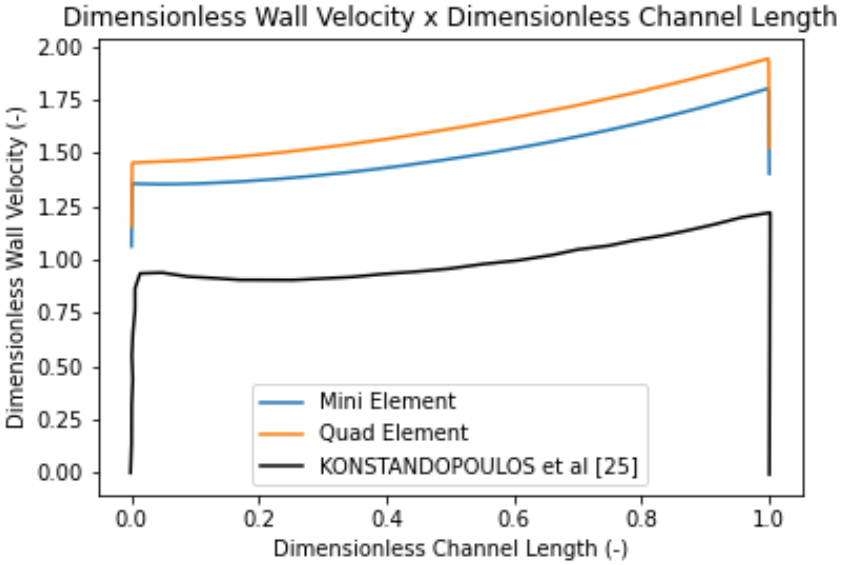

Figure 6.9: Wall Velocity along the channel at Case 1.

is the fact that the reference work does not use the same methodology than the one used here.

6.1.3 Case 2: Air with particulates

After the simulation of a DPF case considering only the airflow, it was also simulated the air along with the particulates. This case was based on the work of SBRIZZAI *et al* [28] which has numerically simulated the problem using the Navier-Stokes equations for the fluid flow and Darcy's law for the porous medium.

The parameters adopted are presented in Table 6.3, where the inlet velocity, air temperature, free mean path of the air, the particulates parameters, and the DPF geometry information are all presented at the reference work, while the others fluid properties at this temperature, which are presented in this table, were obtained at the work of ÇENGEL AND GHAJAR [40]. Finally, the permeability and the inertial resistance coefficient values were obtained by an adjustment procedure in the same way that was done in the reference work.

The characteristic velocity of this problem is the inlet velocity while the characteristic length is the channel width. Then, this problem has $Re \approx 88$, which shows that the flow is laminar, and $Fr \approx 26$.

It is important to highlight that the diameter value of the particulate used in this simulation is close to the diameter value of the biodiesel particulates presented by SOUZA [26]. Then, to get results using the developed code that agrees with the reference results means that this code is reliable to be used for cases where the DPF is working with biodiesel particulates.

Parameter	Value
Inlet Velocity (m/s)	3
Air Density (kg/m^3)	0.6158
Air Dynamic Viscosity (Pa.s)	2.934 x 10^{-5}
Air Temperature (K)	600
Mean free path of gas molecules (nm)	104
Particulates Density (kg/m^3)	1000
Particulates Diameter (nm)	200
Permeability (m^2)	5 x 10^{-12}
Inertial Resistance Coefficient (-)	223.1
Channel Width (mm)	1.4
Channel Length (mm)	253.4
Porous Wall Thickness (mm)	0.38

Table 6.3: Parameters used in the simulation of Case 2.

In this case, we were interested in the flow steady state. Then, since this case is a one-way coupling problem, it was, firstly, calculated the steady state of the airflow and, then, these results were used to calculate the particulates' trajectory without the need for further calculations for the continuous phase. This approach brings a reduction in the computational effort.

In the same way that was done in Case 1, it was also used two meshes, one with MINI elements and the other with quadratic elements, where both meshes have the same number of elements and nodes for pressure. Then, both meshes have 297504 elements and 152540 pressure nodes, but the mesh with MINI elements has 450044 velocity nodes while the mesh with quadratic elements has 602583 velocity nodes.

Figure 6.10 presents the mesh at DPF's inlet in detail. This mesh is the same for both meshes used in this work, the difference between them is the extra nodes that are located at the element centroid for MINI elements and at the element midpoints for quadratic elements. These extra nodes are not presented in the figure.

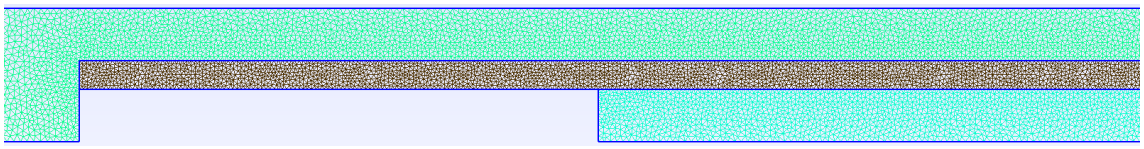

Figure 6.10: Mesh at the inlet of the DPF in Case 2.

Figure 6.11 presents the mesh at DPF's outlet in detail for both meshes used in this work. Since the DPF is very long, to present all the mesh in the same figure would not be interesting and, because of that, it presented the mesh at the device's inlet and outlet.

Simulations were carried out and results qualitatively similar were obtained for both meshes. Then, presenting the results obtained with each mesh is unnecessary

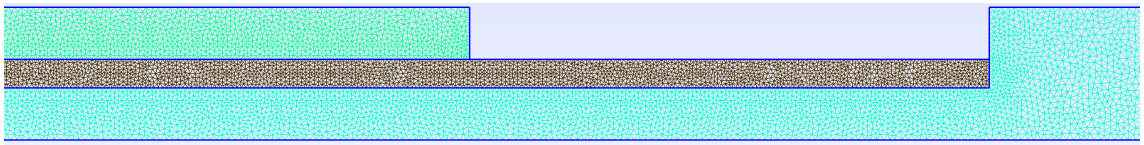

Figure 6.11: Mesh at the outlet of the DPF in Case 2.

and, because of that, it was only presented the results obtained with the MINI mesh. The quadratic mesh results are presented in the appendix.

Figure 6.12 presents the results for the horizontal velocity at the DPF's inlet. It is possible to see that the horizontal velocity at the inlet channel decreases along the channel while the velocity at the outlet channel increases due to the airflow going from the inlet to the outlet channel.

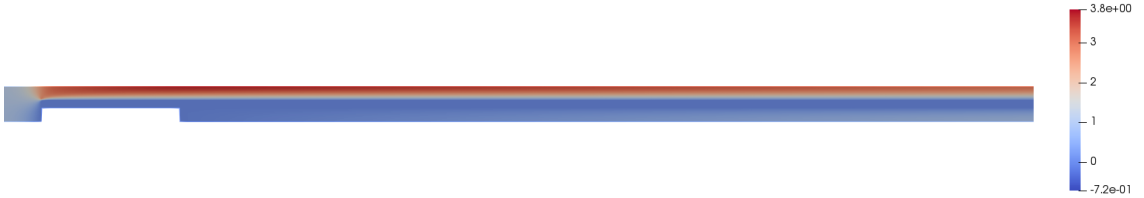

Figure 6.12: Horizontal velocity at DPF's inlet in Case 2.

Figure 6.13 presents the results for the horizontal velocity at the device's outlet. It can be seen how the velocity at the inlet channel has decreased until reaches zero value in the plug while at the outlet channel the velocity has increased.

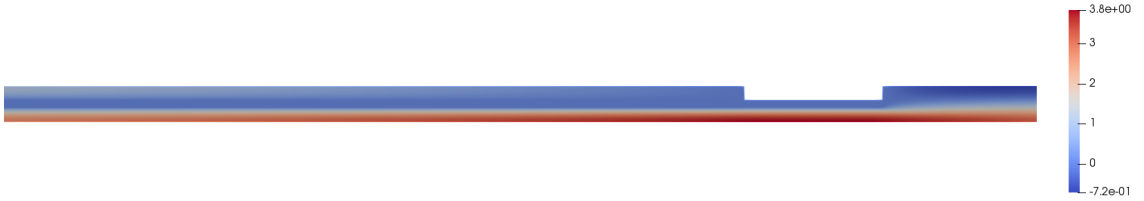

Figure 6.13: Horizontal velocity at DPF's outlet in Case 2.

Figure 6.14 presents the results for pressure at the DPF's inlet. It is possible to see how the pressure at the inlet channel is higher than the pressure at the outlet channel due to the pressure loss in the porous wall.

Figure 6.15 presents the results for pressure at the DPF's outlet. In this case, the pressure has decreased in both channels in comparison with the device's inlet, presented by Figure 6.14.

The results that were get in this work were compared with the reference results to validate them. Then, since the gas and solid phases are decoupled, first, this process was done only for the continuous phase.

Figure 6.16 presents the results for the normalized flow rate across the porous along the DPF. The normalized flow rate consists of the local flow divided by the

Figure 6.14: Pressure at DPF's inlet in Case 2.

Figure 6.15: Pressure at DPF's outlet in Case 2.

total flow. Then, it is possible to see, firstly, that the results that were get with both meshes are similar, indicating that the results may be converged.

However, it is possible to see a significant difference between this work's results and the reference work's results, which can be explained by the different methodologies used by these works, the three-dimensional effects that were only considered in the reference work, the gravitational effects that were only taken into account in this work or also just by numerical errors, since this values are small and can be significantly affected by these errors. Another cause that could be investigated are the used meshes.

After getting the results for the continuous phase, it is necessary to calculate the dispersed phase behavior. The particulates' behavior was calculated based on the continuous phase behavior. In this case, it was randomly displaced 10^4 particles in the domain's inlet and, after that, calculated the particle position through time until all particles had been trapped at the porous wall. It was adopted as the difference between time steps the value of $\Delta t' = 10^{-3}$.

Another important factor is the interaction between the particulates and the porous wall. In this work, it was used the same criterion that was used in the reference work, which assumes that, for this specific case, all particles that have a velocity less than 2 m/s at the porous wall are captured. Then, in both works, all particles were captured.

Figure 6.17 shows a view of the DPF's inlet with the horizontal velocity field and the particulates trapped by the porous wall, which are represented as white spheres. It is possible to see how the number of trapped particulates increases far from the entry.

Figure 6.18 shows a view of the DPF's outlet with the horizontal velocity field and the particulates trapped by the porous wall. In this figure, it can be seen

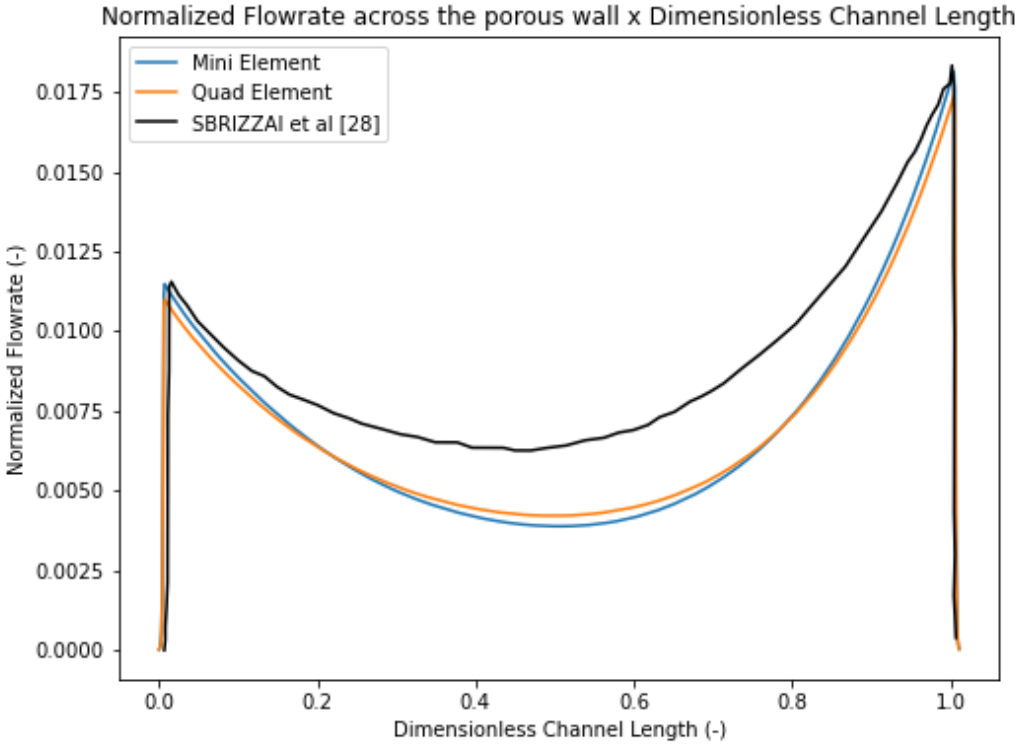

Figure 6.16: Normalized flowrate through the porous wall along the channel at Case 2.

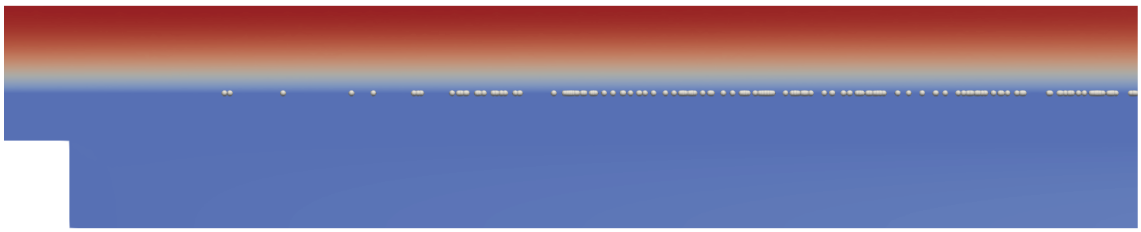

Figure 6.17: Horizontal velocity at DPF's inlet and particulates trapped in the porous wall at Case 2.

that there are many more particles trapped in comparison with the device's inlet, presented in Figure 6.17.

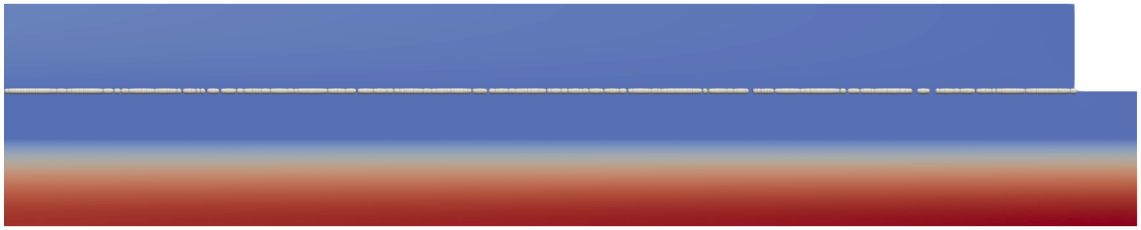

Figure 6.18: Horizontal velocity at DPF's outlet with particulates trapped in the porous wall at Case 2.

Figure 6.19 shows a comparison between the concentration of the particulate along the DPF that was obtained in this work and the reference work. The particulates concentration is the number of particulates trapped in some part of the porous wall divided by the total of particulates. In this work, a greater number of particulates have been trapped next to the channel's inlet. This difference can be explained by the gravity effects taken into account only in this work for the dispersed phase or by the difference presented in the continuous phase which possible explanations were already presented.

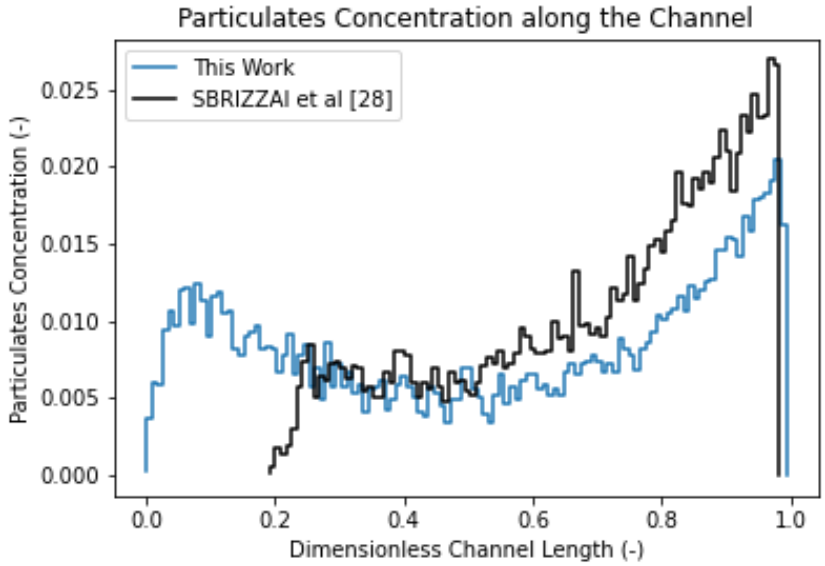

Figure 6.19: Trapped particulates concentration along the channel at Case 2.

6.2 Three Dimensional

6.2.1 Case Set-Up

In the same way that was done in the two-dimensional case, the symmetry conditions are going to be applied to reduce the computational effort of the simulation. However, in this case, there are symmetry conditions not only in the x_2 direction but also in the x_3 direction. Then, it was modeled four quarters of channels, each channel was split in half twice, once for each of these directions.

Figure 6.20 presents the three-dimensional model used in this work to simulate the DPF. The plugs were represented by grey squares while the porous wall was represented by green lines in the device's inlet and outlet. The porous wall was not presented in all of its extension, but it must be understood that the porous wall goes from the DPF's inlet to its outlet. The boundary surfaces of the model are indicated in the figure as top, left, bottom, right, inlet, outlet, and plug.

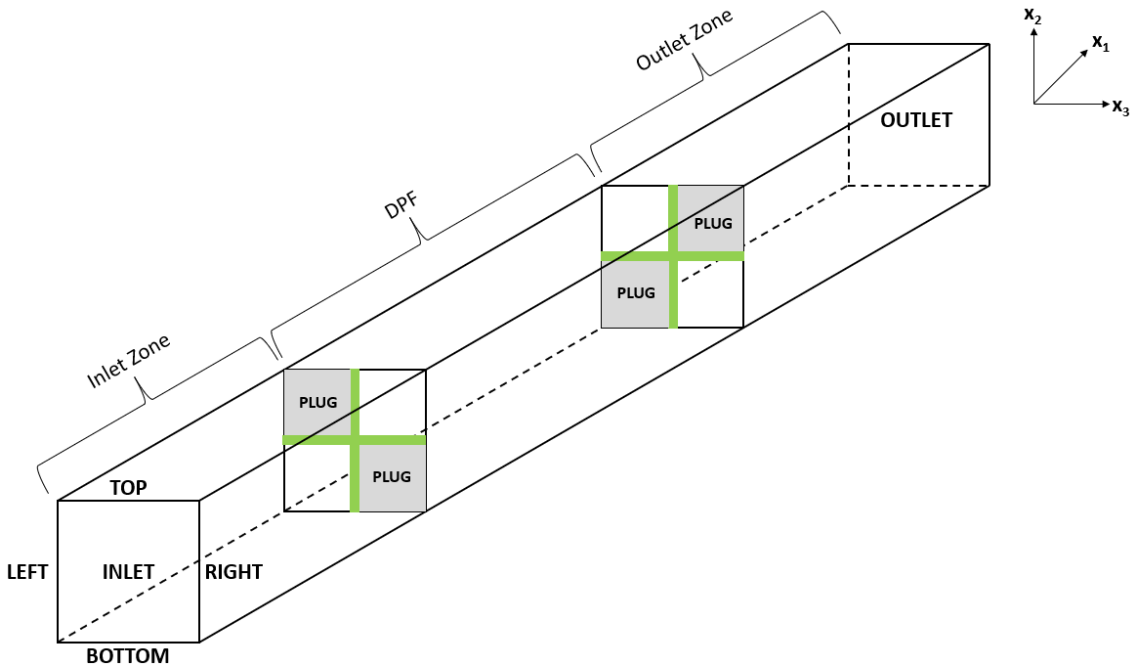

Figure 6.20: Three-Dimensional DPF Model.

Table 6.4 presents the boundary conditions applied to the three-dimensional case. It is presented in this table the type of boundary condition and its mathematical definition applied at each of the boundary surfaces indicated in Figure 6.20.

Type	Boundaries	u_1	u_2	u_3	P
Inlet	Inlet	$u_1 = 1$	$u_2 = 0$	$u_3 = 0$	$\nabla P \cdot \mathbf{n} = 0$
Symmetry	Top, bottom	$\nabla u_1 \cdot \mathbf{n} = 0$	$u_2 = 0$	$\nabla u_3 \cdot \mathbf{n} = 0$	$\nabla P \cdot \mathbf{n} = 0$
Symmetry	Right, left	$\nabla u_1 \cdot \mathbf{n} = 0$	$\nabla u_2 \cdot \mathbf{n} = 0$	$u_3 = 0$	$\nabla P \cdot \mathbf{n} = 0$
Wall	Plug	$u_1 = 0$	$u_2 = 0$	$u_3 = 0$	$\nabla P \cdot \mathbf{n} = 0$
Outlet	Outlet	$\nabla u_1 \cdot \mathbf{n} = 0$	$\nabla u_2 \cdot \mathbf{n} = 0$	$\nabla u_3 \cdot \mathbf{n} = 0$	$P = 0$

Table 6.4: Boundary Conditions of the three-dimensional DPF model.

6.2.2 Case 3: Airflow and channels with 50% of its original length

Firstly, it was intended to simulate a case similar to Case 1 using a three-dimensional model. However, since the three-dimensional model requires much more computational effort, we did not have enough computational resources available to run a case with the same geometry that was used in Case 1. Then, this case was simulated using the same parameters as Case 1, presented by Table 6.2, but considering only half of the channel length to reduce the computational effort. So, this case has channels with a length equal to 152.4 mm.

In order to check the convergence of the results, it was run simulations with three different meshes. All three meshes were formed by tetrahedron MINI elements and were obtained using Gmsh. The number of elements, pressure nodes, and velocity nodes of each mesh is presented in Table 6.5. Finally, it is important to say that Mesh 3 used almost all the computational memory that we have available, making the use of more refined meshes not possible.

Mesh	Elements	Pressure Nodes	Velocity Nodes
Mesh 1	3078653	579548	3658201
Mesh 2	4042608	743974	4786582
Mesh 3	5373464	967712	6341176

Table 6.5: Details of the meshes used in Case 3.

Then, the simulations had been run until they reached a steady state of the flow. Figure 6.21 presents the results obtained using the three presented meshes for the horizontal velocity along a channel with a plug in its exit, an inlet channel, and a channel with a plug in its entry, an outlet channel. Firstly, it is possible to see some instabilities in the results, which may indicate that the meshes were not refined enough to provide accurate results.

Moreover, it is also possible to see in the figure that the velocity at the inlet channel has a great decrease at the end of the channel while the velocity in the outlet channel has a great increase at the same region. This fact does not agree with Case 1 and with KONSTANDOPOULOS *et al* [25] results where it was observed

an almost linear behavior for the velocity in both channels. This difference may be another proof that the results are not in convergence.

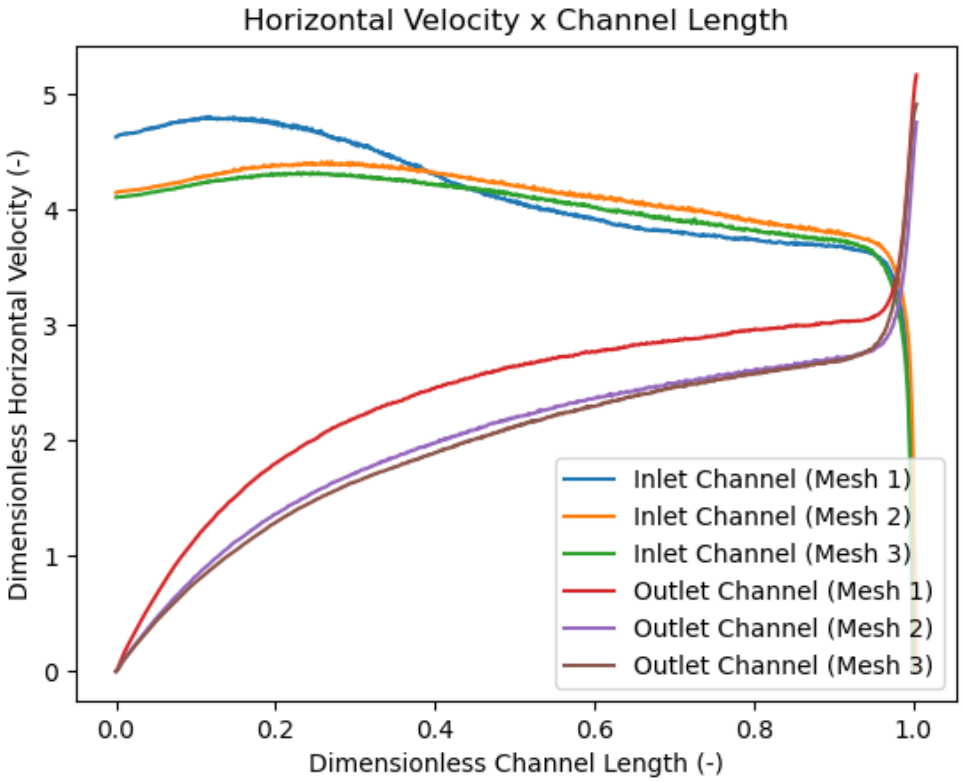

Figure 6.21: Horizontal velocity along the inlet and outlet channels results obtained using three different meshes.

Figure 6.22 presents the results of the velocity in the x_2 direction in the porous wall between the top right and bottom right channels along the channels for different positions. The positions were taken into account according to the distance from the center of these channels in the x_3 directions.

Firstly, it is possible to see that the velocity values are decreasing as it moves away from the center. This may be explained by the flow in the x_3 direction which must become stronger far from the center. Another important observation is the velocity fluctuations that may indicate numerical errors.

Figure 6.23 presents the results of the velocity in the x_3 direction in the porous wall between the top right and top left channels along them for different positions. The positions were taken into account according to the distance from the center of these channels in the x_2 directions. In this figure, it is observed the same things that were mentioned for Figure 6.22.

It was possible to visualize these results using the Paraview. In Paraview the directions X, Y, and Z, refer, respectively, to the directions x_1, x_2, and x_3. Then, since the results do not seem to be converged, it is presented here the ones got with

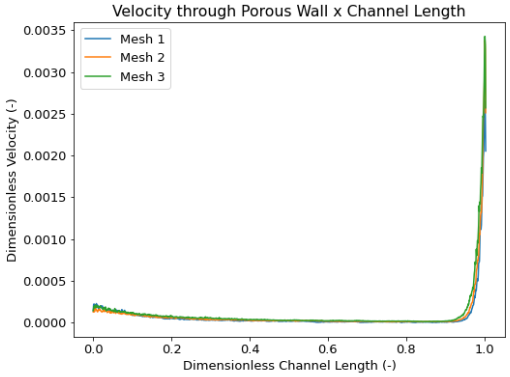

(a) $x_3 = 0.0$

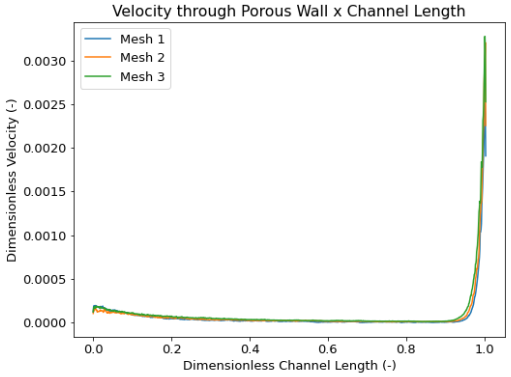

(b) $x_3 = 0.1$

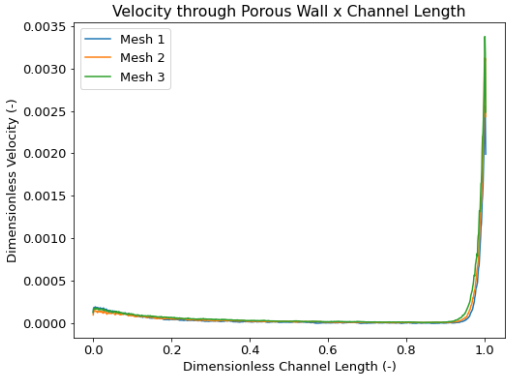

(c) $x_3 = 0.2$

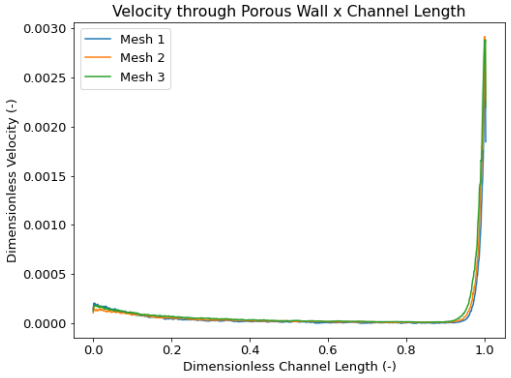

(d) $x_3 = 0.3$

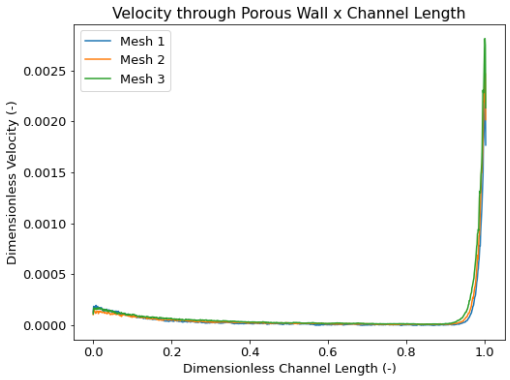

(e) $x_3 = 0.4$

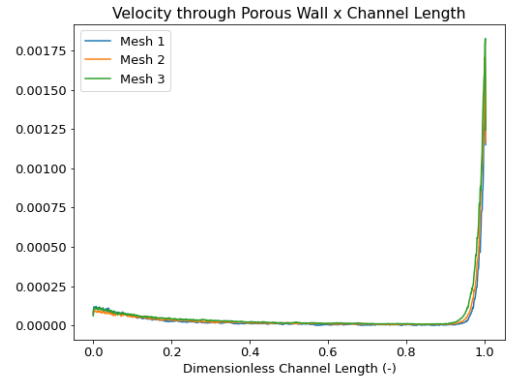

(f) $x_3 = 0.5$

Figure 6.22: Velocity in x_2 direction in the porous wall at different distances from the channels centers.

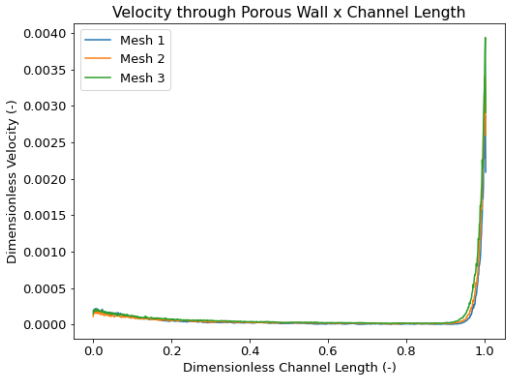

(a) $x_2 = 0.0$

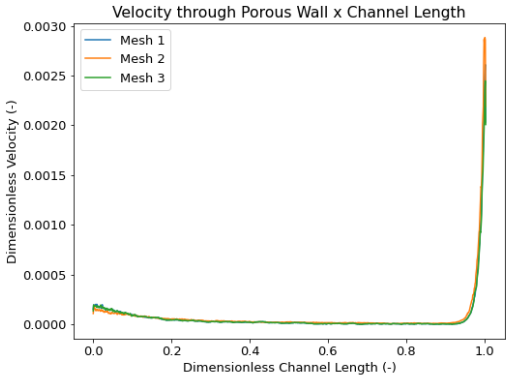

(b) $x_2 = 0.1$

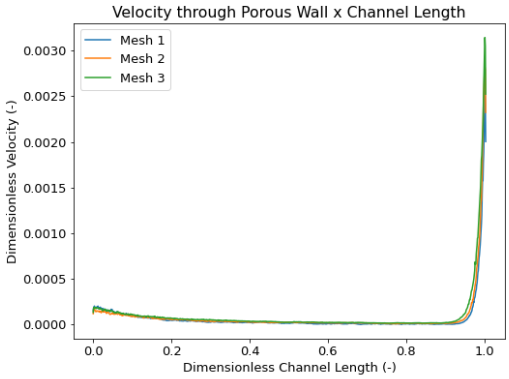

(c) $x_2 = 0.2$

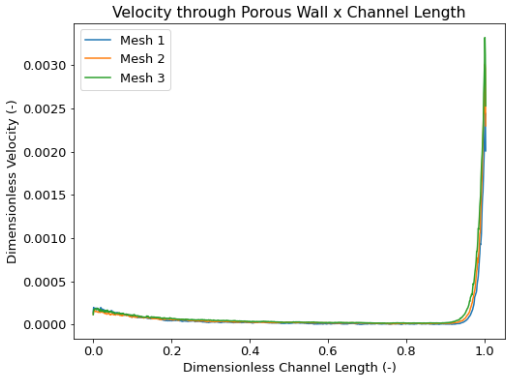

(d) $x_2 = 0.3$

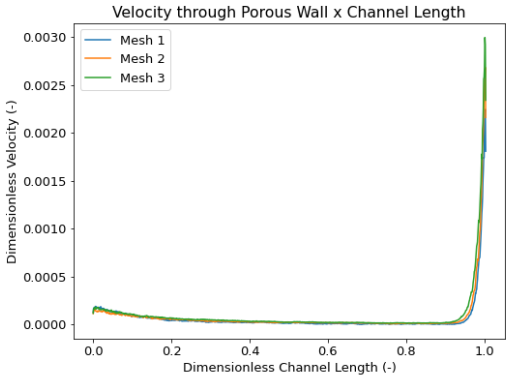

(e) $x_2 = 0.4$

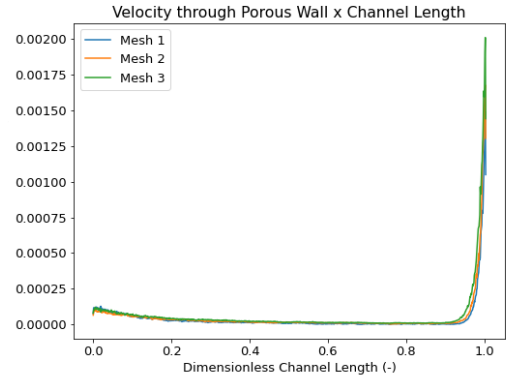

(f) $x_2 = 0.5$

Figure 6.23: Velocity in x_3 direction in the porous wall at different x_2 values.

Mesh 3, which is the most refined mesh. The other meshes' results are presented in the appendix.

Figure 6.24 presents the horizontal velocity field, which was presented in this work as the variable u_1, at the DPF's inlet in the $x_1 - x_2$ plane, which is the DPF's right according to Figure 6.20. In this figure, it is possible to see that the air enters the top channel and its velocity decreases along the channel while it increases in the bottom channel.

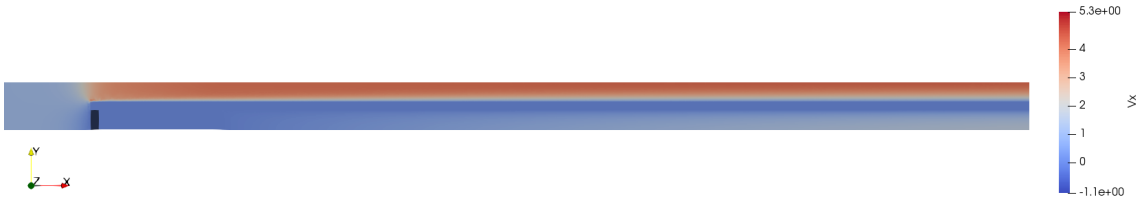

Figure 6.24: Horizontal velocity field at the DPF's inlet plotted in the $x_1 - x_2$ plane.

Figure 6.25 presents the horizontal velocity field at the DPF's outlet in the $x_1 - x_2$ plane, which is the DPF's right according to Figure 6.20. In this figure, it is possible to see that the air in the top had decreased until reached zero in the plug while in the bottom channel it increased.

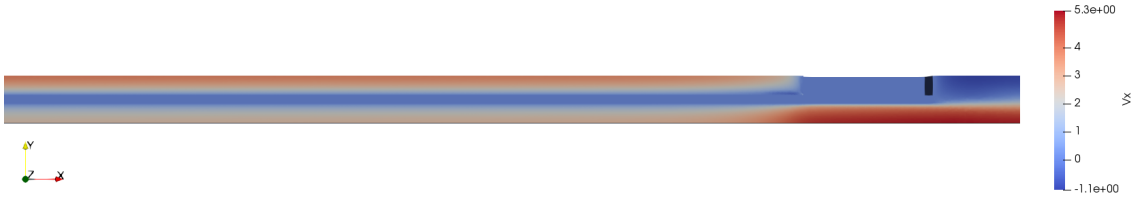

Figure 6.25: Horizontal velocity field at the DPF's outlet plotted in the $x_1 - x_2$ plane.

Figure 6.26 presents the horizontal velocity field at the DPF's inlet in the $x_1 - x_3$ plane, located in the DPF's bottom according to Figure 6.20. It is possible to see that the air enters the bottom left channel, according to Figure 6.20, which is the bottom channel in this figure, and its velocity decreases while the velocity on the other channel increases.

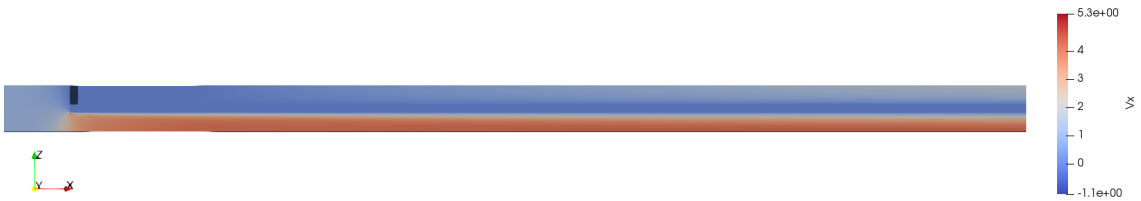

Figure 6.26: Horizontal velocity field at the DPF's inlet plotted in the $x_1 - x_3$ plane.

Figure 6.27 presents the horizontal velocity field at the DPF's outlet in the $x_1 - x_3$ plane, located in the DPF's bottom according to Figure 6.20. It is possible to see

that the air in this figure's bottom channel had decreased until reached zero in the plug while on the other channel it increased.

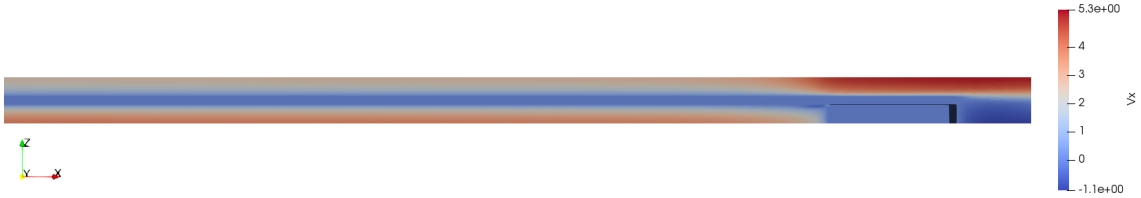

Figure 6.27: Horizontal velocity field at the DPF's outlet plotted in the $x_1 - x_3$ plane.

Figure 6.28 presents the pressure field at the DPF's inlet in the $x_1 - x_2$ plane, which is the DPF's right according to Figure 6.20. It is possible to see how the pressure has higher values in the region before the device.

Figure 6.28: Pressure field at the DPF's inlet plotted in the $x_1 - x_2$ plane.

Figure 6.29 presents the pressure field at the DPF's outlet in the $x_1 - x_2$ plane, which is the DPF's right according to Figure 6.20. It is possible to see how the pressure has lower values after the device, showing that there is a great pressure drop along the DPF caused by the airflow through the porous wall.

Figure 6.29: Pressure field at the DPF's outlet plotted in the $x_1 - x_2$ plane.

Figure 6.30 presents the pressure field at the DPF's inlet in the $x_1 - x_3$ plane in the DPF's bottom according to Figure 6.20. In this figure, it is possible to see again the high pressure values before the DPF.

Figure 6.31 presents the pressure field at the DPF's outlet in the $x_1 - x_3$ plane in the DPF's bottom according to Figure 6.20. Once again, it is possible to see that there is a great pressure drop in the device.

Figure 6.30: Pressure field at the DPF's inlet plotted in the $x_1 - x_3$ plane.

Figure 6.31: Pressure field at the DPF's outlet plotted in the $x_1 - x_3$ plane.

6.2.3 Case 4: Airflow and channels with 20% of its original length

After the Case 3 results analysis, it seems that the convergence of results was not achieved. Then, it was run a case with the same parameters, presented by Table 6.2, but now with 20% of the original channel length, which is equal to 60.96 mm.

Once again, to check the convergence of the results, it was run simulations with three different meshes. All three meshes were formed by tetrahedron MINI elements and were obtained using Gmsh. The number of elements, pressure nodes, and velocity nodes of each mesh is presented in Table 6.6. Finally, it is important to say that Mesh 3 used almost all the computational memory that we have available, making the use of more refined meshes not possible.

Mesh	Elements	Pressure Nodes	Velocity Nodes
Mesh 1	1331883	252679	1584562
Mesh 2	2347943	425833	2773776
Mesh 3	4098324	722834	4821158

Table 6.6: Details of the meshes used in Case 4.

Then, the simulations had been run until they reached a steady state of the flow. Figure 6.32 presents the results obtained using the three presented meshes for the horizontal velocity along a channel with a plug in its exit, an inlet channel, and a channel with a plug in its entry, an outlet channel. Firstly, it is possible to see some instabilities in the results, which may indicate that the meshes were not refined enough to provide accurate results.

Analyzing the results for the inlet channel, it is possible to see that they have similar shapes, but Mesh 2 has lower values in comparison to Mesh 1 and Mesh 3

has lower values in comparison to the other meshes. All the meshes provided results with the velocity staying almost constant along the channel and suddenly decreasing until reached zero at the end of the channel. However, it also can be seen that the velocity decrease seems to become smoother with more refined meshes. Then, this fact may indicate that we have not reached a convergence of results and that more refined meshes would provide results that are more likely to that obtained in Case 1 and in the literature.

Now looking at the results for the outlet channel, it is possible to see that the velocity increases almost linearly until near the channel's end when the flow has suddenly a great increase. Then, as it was observed in the inlet channel, this increase becomes smoother in the most refined mesh. Despite that, it was also observed that Mesh 1 provided higher values and Mesh 3 had lower values.

Another important observation is that the results obtained for mesh 2 and mesh 3 in this case, presented by Figure 6.32, seem to be more distant from each other than the ones obtained in Case 3, presented by Figure 6.21. This observation can imply that the reduction of the channel length did not make the case simpler but had the opposite effect.

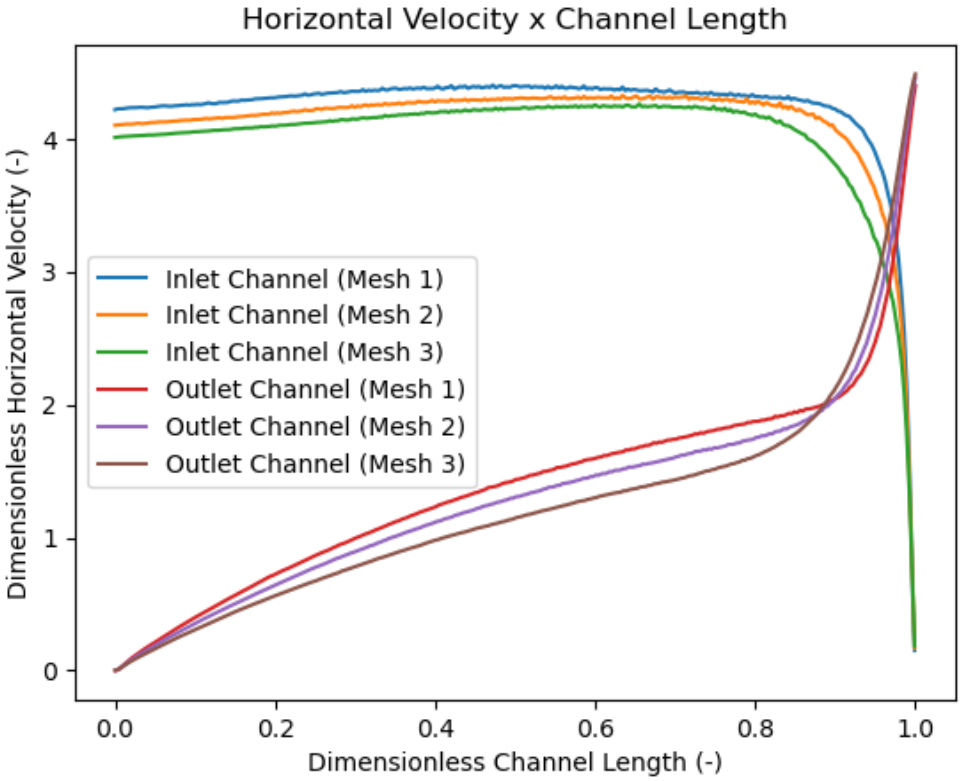

Figure 6.32: Horizontal velocity along the inlet and outlet channels results obtained using three different meshes.

Figure 6.33 presents the results of the velocity in the x_2 direction in the porous

wall between the top right and bottom right channels along the channels for different positions. The positions were taken into account according to the distance from the center of these channels in the x_3 directions.

Firstly, it is possible to see that the results for different distances from the center seem to be similar, except for the results got at a distance of $x_3 = 0.5$ from the center, Figure 6.33f. This may be explained by the fact that at this distance from the center, the flow in the x_3 direction must be higher, affecting the flow in the x_2 direction.

Moreover, it is also possible to see that the results present some instabilities, which may be caused by numerical errors indicating that it has not achieved a convergence of results. This lack of convergence can also be observed in the difference in the results got with each mesh.

Figure 6.34 presents the results of the velocity in the x_3 direction in the porous wall between the top right and top left channels along them for different positions. The positions were taken into account according to the distance from the center of these channels in the x_2 directions.

In this case, the results that are not similar to the rest of them are the ones got at distances from the centers of $x_2 = 0.4$ and $x_2 = 0.5$. Besides that, once more it is possible to see instabilities in all the results, which indicates once more that the results did not converge.

Therefore, it looks like the results have not achieved a convergence when considering 20% of the original channel length and using almost all computational resources that we have available.

It was possible to visualize these results using the Paraview. In Paraview the directions X, Y, and Z, refer, respectively, to the directions x_1, x_2, and x_3. Since the results did not seem to be converged, it is presented the results got with Mesh 3, which is the most refined mesh. The other meshes' results are presented in the appendix.

Figure 6.35 presents the horizontal velocity field, which was presented in this work as the variable u_1, along the channels in the $x_1 - x_2$ plane, which is the DPF's right according to Figure 6.20. In this figure, it is possible to see that the air enters the top channel and its velocity seems to only reduce near the plug, at the end of the channel. On the other hand, the velocity in the bottom channel seems to stay constant along the channel and it only increases at the end of the channel. This velocity behavior is different from what was observed in the two-dimensional case, Case 1, and in the literature, where the velocities were increasing or decreasing almost linearly along the channel.

Figure 6.36 presents the horizontal velocity field, which is the u_1 variable, along the channels in the $x_1 - x_3$ plane, which is the DPF's bottom according to Figure

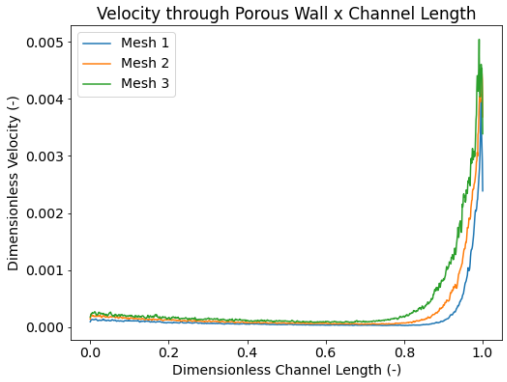

(a) $x_3 = 0.0$

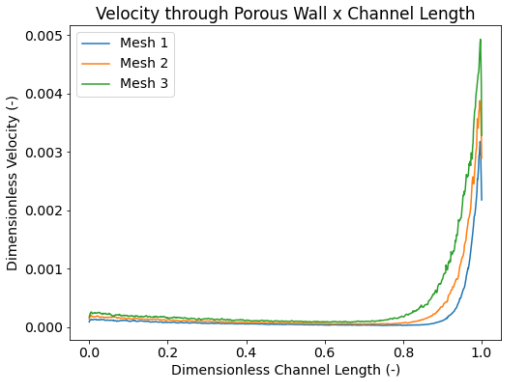

(b) $x_3 = 0.1$

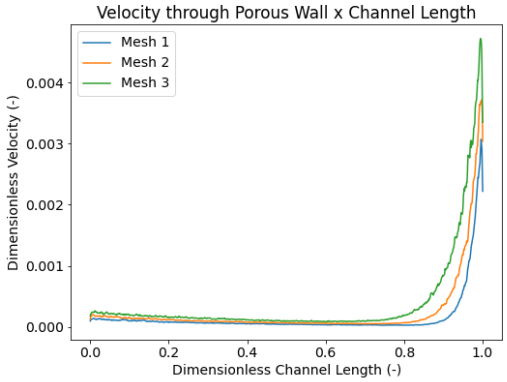

(c) $x_3 = 0.2$

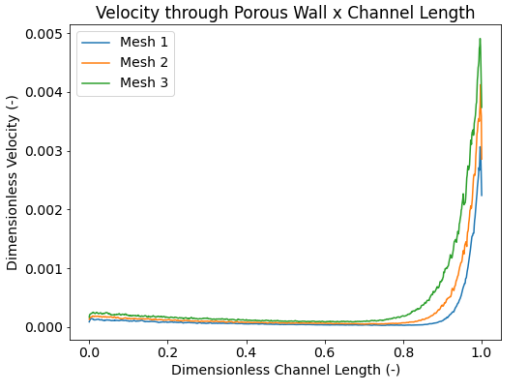

(d) $x_3 = 0.3$

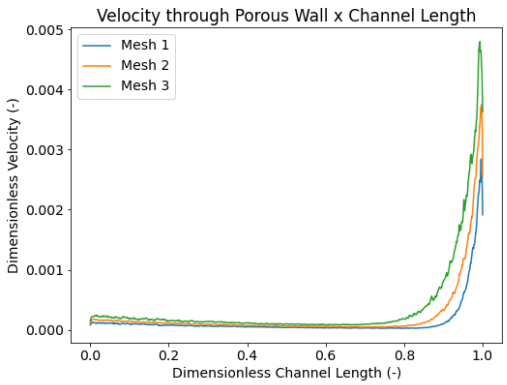

(e) $x_3 = 0.4$

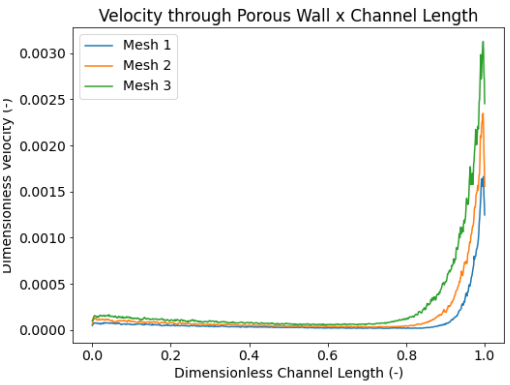

(f) $x_3 = 0.5$

Figure 6.33: Velocity in x_2 direction in the porous wall at different distances from the channels centers.

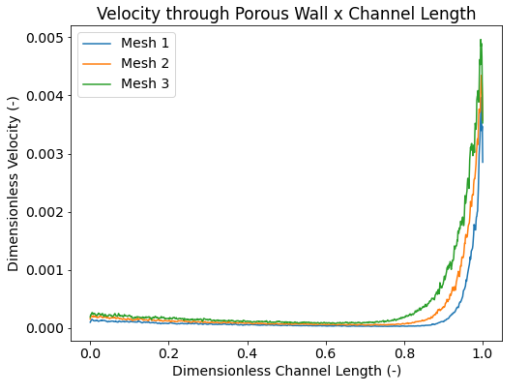

(a) $x_2 = 0.0$

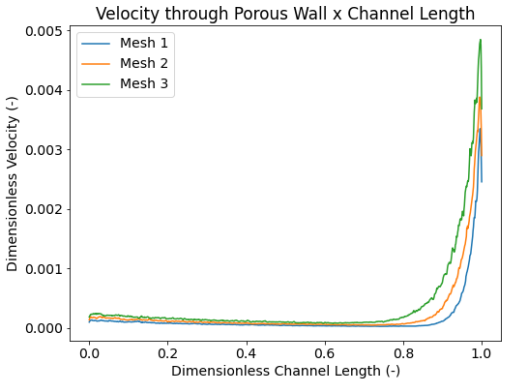

(b) $x_2 = 0.1$

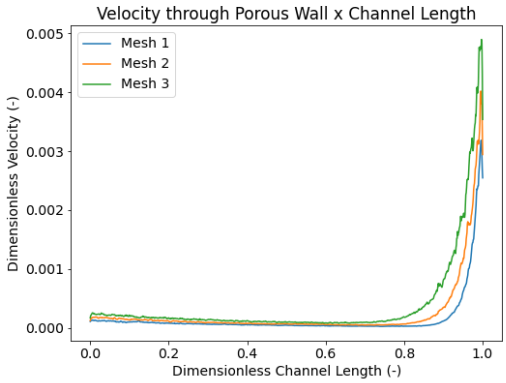

(c) $x_2 = 0.2$

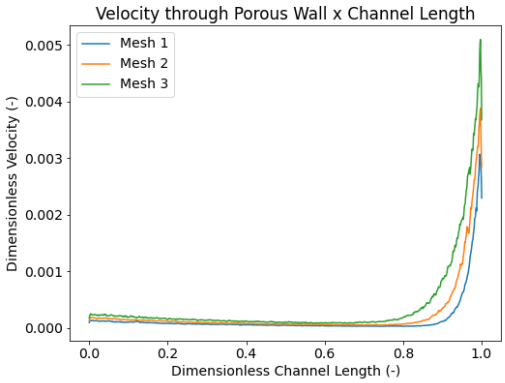

(d) $x_2 = 0.3$

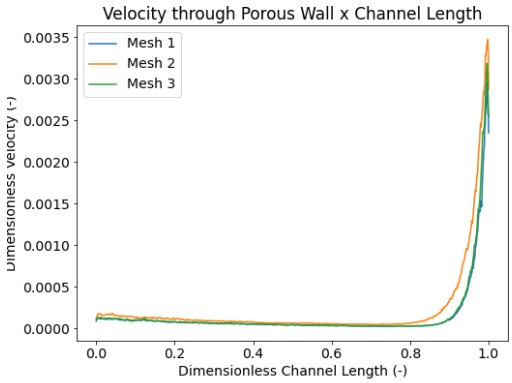

(e) $x_2 = 0.4$

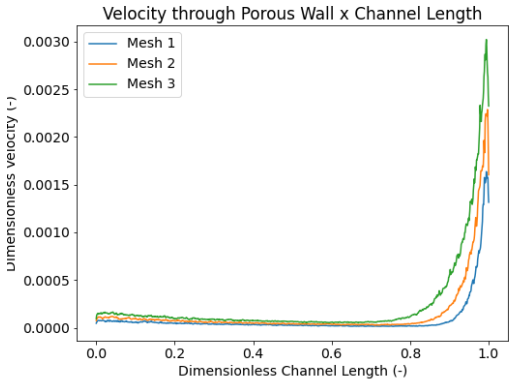

(f) $x_2 = 0.5$

Figure 6.34: Velocity in x_3 direction in the porous wall at different x_2 values.

Figure 6.35: Horizontal velocity field plotted in the $x_1 - x_2$ plane.

6.20. It is possible to see that the air enters the bottom left channel, according to Figure 6.20, which is the bottom channel in this figure, and its velocity seems to stay constant until the end of the channel where it suddenly has a great decrease, while the velocity on the other channel stays constant until it suddenly has a great increase in the same region. Once more, this fact is not observed in Case 1 and in the literature, but only here when the DPF is modeled as three-dimensional.

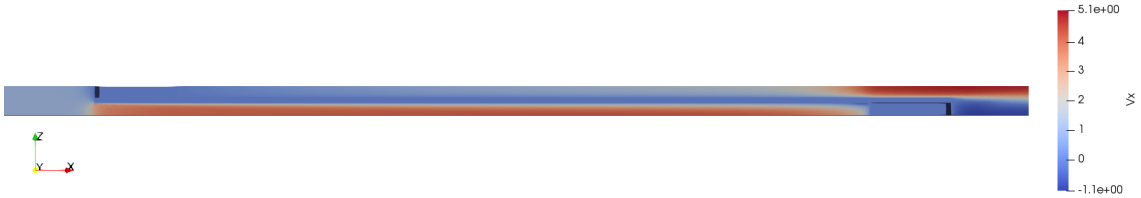

Figure 6.36: Horizontal velocity field plotted in the $x_1 - x_3$ plane.

Figure 6.37 presents the pressure field along the channels in the $x_1 - x_2$ plane, which is the DPF's right according to Figure 6.20. It is possible to see how the pressure has higher values in the region before the device and lower values after the device, showing that there is a great pressure drop along the DPF.

Figure 6.37: Pressure field plotted in the $x_1 - x_2$ plane.

Figure 6.38 presents the pressure field along the channels in the $x_1 - x_3$ plane in the DPF's bottom according to Figure 6.20. In this figure, it is possible to see again the great pressure drop that occurs when the air is going through the DPF.

Figure 6.38: Pressure field plotted in the $x_1 - x_3$ plane.

Chapter 7

Conclusions

The main goal of this work was to develop a methodology to simulate the multiphase flow, constituted by air and particulates formed by the biodiesel combustion, inside a DPF. In order to achieve that, firstly, a methodology was proposed. Then, a computational code based on this methodology was developed from scratch and its implementation was verified. Finally, this code was used to simulate some DPF cases that were found in the literature.

The first case that was simulated modeled the problem as two-dimensional and just considered the airflow inside the device. In this case, we had some differences between this work and the literature results, which could be caused mainly by the different methodologies used by each work or by meshes that are not good enough. However, this work's results are coherent with the literature ones and it is expected that with some improvement on these factors, more accurate results are going to be achieved.

A two-dimensional multiphase flow case, constituted by air and particulates, was simulated. The particulates present in this case have size and density values next to the biodiesel particulates ones. In the same was as the previous case, this work's results had some differences in relation to the literature ones that can be explained by the same reasons presented for the last case. Then, despite that, it is expected that, with some improvements, the presented methodology can be used to simulate the airflow inside a DPF along with the biodiesel particulates, which was the main goal of this work.

Since a three-dimensional model is more compatible with reality, the first case was simulated again but now modeling the problem as three-dimensional. A three-dimensional model is much more complex than the two-dimensional one and demands much more computational resources. Because of that, the case was simulated considering only half of the first case channel length. The results that were obtained in this case were very different from the ones obtained in the 2D case and the reason for that seemed to be the mesh that was not refined enough.

In this scenario, since it used almost all computational resources available, a new case was simulated considering only 20% of the original channel length. Once more the results were very different than expected and the explanation could be not only the mesh again but also the fact that shorter channels make the simulation more complex.

After analyzing these results, it is possible to say, firstly, that the presented methodology seems to work well for two-dimensional cases. Then, it is expected that, after some improvements, it can be used to study in detail the flow inside the DPF, despite its limitation to represent the three-dimensional effects.

Moreover, despite that we have not achieved good results for DPF flow in the three-dimensional cases, it is expected that more refined meshes provide good results since this methodology provided good results for other three-dimensional cases. Then, more computational resources would be needed to do that.

It is suggested for future works to run the three-dimensional case using more refined meshes and to compare the results with the literature and with the two-dimensional results. Besides that, since the computational resources needed may be difficult to find, it is also suggested to study how to reduce the error in the interface between the fluid and porous regions. The error in the results found in this region was observed in Chapter 5 at the Flow over Porous Region problem and to mitigate this problem it may not be necessary to use very refined meshes.

Another suggestion is to use other methodologies to simulate flow with porous mediums and compare them with this one, verifying which one was able to provide the best results using less computational effort. The inclusion of turbulent models in the presented methodology is also strongly recommended for the future.

Finally, it is essential to say that this work has not only presented a methodology that can be used to study in detail the flow inside a DPF in vehicles using biodiesel but also has presented a great basis for further developments in this and similar areas.

References

[1] KNOTHE, G., RAZON, L. F. "Biodiesel Fuels", *Progress in Energy and Combustion Science*, v. 58, pp. 36–59, jan. 2017.

[2] LIN, L., CUNSHAN, Z., VITTAYAPADUNG, S., et al. "Opportunities and challenges for biodiesel fuel", *Applied Energy*, v. 88, n. 4, pp. 1020–1031, abr. 2011.

[3] AGARWAL, A. K. "Biofuels (alcohols and biodiesel) applications as fuels for internal combustion engines", *Progress in Energy and Combustion Science*, v. 33, n. 3, pp. 233–271, jun. 2007.

[4] BART, J. C., PALMERI, N., CAVALLARO, S. *Biodiesel Science and Technology*. 1 ed. Cambridge, Woodhead Publishing, 2010.

[5] RODRIGUES, A. "Policy, regulation, development and future of biodiesel industry in Brazil", *Cleaner Engineering and Technology*, v. 4, jul. 2021.

[6] MOSER, B. R. "Biodiesel production, properties, and feedstocks", *In Vitro Cellular Developmental Biology - Plant*, v. 45, pp. 229—-266, jun. 2009.

[7] MCCORMIC, R. L. "The Impact of Biodiesel on Pollutant Emissions and Public Health", *Inhalation Toxicology*, v. 19, n. 12, pp. 1033–1039, out. 2008.

[8] HOEKMAN, S. K., ROBBINS, C. "Review of the effects of biodiesel on NOx emissions", *Fuel Processing Technology*, v. 96, pp. 237–249, jan. 2012.

[9] GUAN, B., ZHAN, R., LIN, H., et al. "Review of the state-of-the-art of exhaust particulate filter technology in internal combustion engines", *Journal of Environmental Management*, v. 154, pp. 225–258, mar. 2015.

[10] KHAIR, M. K. *A Review of Diesel Particulate Filter Technologies*. SAE Technical Paper 2003-01-2303, 2003.

[11] RODRIGUEZ, J., LAPUERTA, M., SÁNCHEZ-VALDEPEÑAS, J. "Regeneration of diesel particulate filters: Effect of renewable fuels", *Renewable Energy*, v. 104, pp. 30–39, nov. 2016.

[12] SLATTERY, J. C. *Advanced Transport Phenomena.* 1 ed. United States of America, Cambridge University Press, 1999.

[13] CIMOLIN, F., DISCACCIATI, M. "Navier–Stokes/Forchheimer models for filtration through porous media", *Applied Numerical Mathematics*, v. 72, pp. 205–224, jul. 2013.

[14] CROWE, C., SCHWARZKOPF, J., SOMMERFELD, M., et al. *Multiphase Flows with Droplets and Particles.* 2 ed. Boca Raton, CRC Press, 2011.

[15] BALACHANDAR, S., EATON, J. K. "Turbulent Disprsed Multiphase Flow", *Annual Review of Fluid Mechanics*, v. 42, n. 1, pp. 111–133, jan. 2010.

[16] TABAEIKAZEROONI, S. H. *Laminar and turbulent particle laden flows : a numerical and experimental study.* Tese de Ph.D, KTH Royal Institute of Technology, Stockholm, Sweden, 2019.

[17] FERZIG, J. H., PERIC, M. *Computational Methods for Fluid Dynamics.* 3 ed. New York, Springer-Verlag, 2002.

[18] LEWIS, R. W., NITHIARASU, P., SEETHARAMU, K. N. *Fundamentals of the Finite Element Method for Heat and Fluid Flow.* New York, John Wiley & Sons, 2004.

[19] SAMEI, E. *CFD and Experimental Analysis of Diesel Particulate Filter.* M.Sc. dissertation, Chalmers University of Technology, Göteborg, Sweden, 2012.

[20] PISCAGLIA, F., RUTLAND, C. J., FOSTER, D. E. *Development of a CFD Model to Study the Hydrodynamic Characteristics and the Soot Deposition Mechanism on the Porous Wall of a Diesel Particulate Filter.* SAE Technical Paper 2005-01-0963, 2005.

[21] JANISZEWSKI, A., TEODORCZYK, A. "CFD modeling of the regeneration process in diesel particulate filter using FLUENT", *Journal of KONES Powertrain and Transport*, v. 13, n. 3, pp. 109–118, jan. 2016.

[22] DEUSCHLE, T., JANOSKE, U., PIESCHE, M. "A CFD-model describing filtration, regeneration and deposit rearrangement effects in gas filter systems", *Chemical Engineering Journal*, v. 135, n. 1, pp. 49–55, jan. 2008.

[23] PISCAGLIA, F., MONTORFANO, A., ONORATI, A. *Development of a Multi-Dimensional Parallel Solver for Full-Scale DPF Modeling in OpenFOAM.* SAE Technical Paper 2009-01-1965, 2009.

[24] PISCAGLIA, F., ONORATI, A., RUTLAND, C. J., et al. "Multi-Dimensional Modeling of the Soot Deposition Mechanism in Diesel Particulate Filters", *SAE International Journal of Fuels and Lubricants*, v. 1, n. 1, pp. 210–230, 2008.

[25] KONSTANDOPOULOS, A., SKAPERDAS, V., WARREN, J., et al. *Optimized Filter Design and Selection Criteria for Continuously Regenerating Diesel Particulate Traps*. SAE Technical Paper 1999-01-0468, 1999.

[26] DE SOUZA, J. P. I. *Particle-Laden Multiphase Flows: A Finite Element Analysis on Biofuel Particle Emissions*. M.Sc. dissertation, Universidade Federal do Rio de Janeiro, Rio de Janeiro, Brazil, 2021.

[27] SOUZA, J. P. I., ANJOS, G. R. "A finite element analysis of multiphase conjugated flow in diesel and biodiesel-driven engine filtration device", *Journal of the Brazilian Society of Mechanical Sciences and Engineering*, v. 45, n. 375, jun. 2023.

[28] SBRIZZAI, F., FARALDI, P., SOLDATI, A. "Appraisal of three-dimensional numerical simulation for sub-micron particle deposition in a micro-porous ceramic filter", *Chemical Engineering Science*, v. 60, n. 23, pp. 6551–6563, 2005.

[29] BENSAID, S., MARCHISIO, D., FINO, D., et al. "Modelling of diesel particulate filtration in wall-flow traps", *Chemical Engineering Journal*, v. 154, n. 1, pp. 211–218, 2009.

[30] BATCHELOR, G. K. *An Introduction to Fluid Dynamics*. 1 ed. United States of America, Cambridge University Press, 2000.

[31] SQUIRES, K. "Point-particle methods for disperse flows". In: Prosperetti, A., Tryggvason, G. (Eds.), *Computational Methods for Multiphase Flow*, cap. 9, Cambridge, UK, Cambridge University Press, 2007.

[32] ELGHOBASHI, S. "An Updated Classification Map of Particle-Laden Turbulent Flows". In: *IUTAM Symposium on Computational Approaches to Multiphase Flow*, pp. 3–10, Dordrecht, jan. 2006.

[33] OUNIS, H., AHMADI, G., MCLAUGHLIN, J. B. "Brownian diffusion of submicrometer particles in the viscous sublayer", *Journal of Colloid and Interface Science*, v. 143, n. 1, pp. 266–277, abr. 1991.

[34] HUGHES, T. J. R. *The Finite Element Method: Linear Static and Dynamic Finite Element Analysis*. 1 ed. United States of America, Prentice-Hall, Inc., 1987.

[35] CHUNG, T. J. *Computational Fluid Dynamics*. 2 ed. United States of America, Cambridge University Press, 2010.

[36] DOS ANJOS, G. R. *A 3D ALE Finite Element Method for Two-Phase Flows with Phase Change*. Tese de Ph.D, École Polytechnique Fédérale de Lausanne, Lausanne, Switzerland, 2012.

[37] CHAPRA, S. C., CANALE, R. P. *Numerical Methods for Engineers*. 6 ed. New York, McGraw-Hill, 2010.

[38] MARCHI, C., SUERO, R., ARAKI, L. "The Lid-Driven Square Cavity Flow: Numerical Solution with a 1024 x 1024 Grid", *Journal of The Brazilian Society of Mechanical Sciences and Engineering*, v. 31, n. 3, pp. 186–198, jul. 2009.

[39] OWOLABI, B. *Characterisation of turbulent duct flows: experiments and direct numerical simulations*. 1 ed. Switzerland, Springer, 2019.

[40] ÇENGEL, Y. A., GHAJAR, A. J. *Transferência de Calor e Massa - Uma abordagem prática*. 4 ed. Porto Alegre, McGraw-hill,, 2012.

Appendix A

Other Figures

This appendix presents the figures that were not important to be part of the main text, but it is important to be part of this work in the case of some readers interested in checking them.

Figure A.1 presents the results for the horizontal velocity at the inlet region obtained with the quadratic mesh. This result was considered qualitatively similar to Figure 6.4.

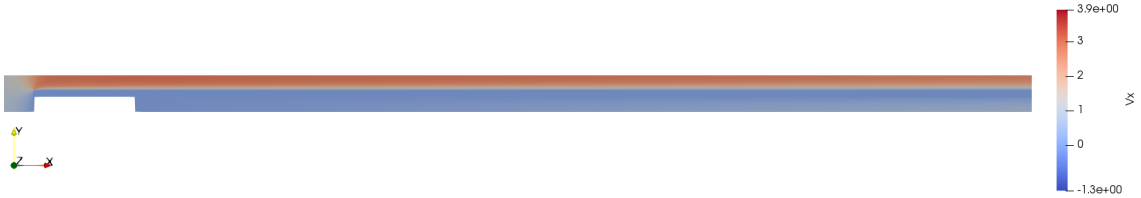

Figure A.1: Horizontal velocity at DPF's inlet in Case 1 obtained with the quadratic mesh.

Figure A.2 presents the results for the horizontal velocity at the outlet region obtained with the quadratic mesh. This result was considered qualitatively similar to Figure 6.5.

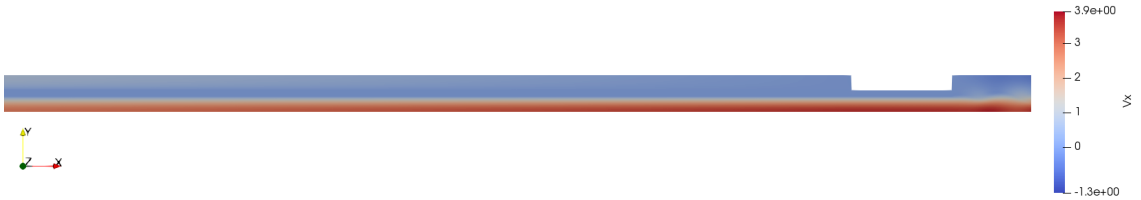

Figure A.2: Horizontal velocity at DPF's outlet in Case 1 obtained with the quadratic mesh.

Figure A.3 presents the results for pressure at the DPF's inlet. This result was considered qualitatively similar to Figure 6.6.

Figure A.4 presents the results for pressure at the DPF's outlet. This result was considered qualitatively similar to Figure 6.7.

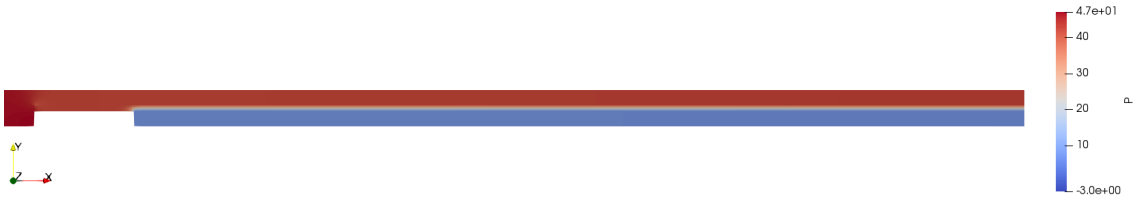

Figure A.3: Pressure at DPF's inlet in Case 1 with the quadratic mesh.

Figure A.4: Pressure at DPF's outlet in Case 1 with the quadratic mesh.

Figure A.5 presents the results for the horizontal velocity at the DPF's inlet using the quadratic mesh. This result was considered qualitatively similar to Figure 6.12.

Figure A.5: Horizontal velocity at DPF's inlet in Case 2 using quadratic mesh.

Figure A.6 presents the results for the horizontal velocity at the DPF's outlet using the quadratic mesh. This result was considered qualitatively similar to Figure 6.13.

Figure A.7 presents the results for the pressure at the DPF's inlet using the quadratic mesh. This result was considered qualitatively similar to Figure 6.14.

Figure A.8 presents the results for the pressure at the DPF's outlet using the quadratic mesh. This result was considered qualitatively similar to Figure 6.15.

Figure A.9 presents the horizontal velocity field at the DPF's inlet in the $x_1 - x_2$ plane using Mesh 1 for Case 3.

Figure A.10 presents the horizontal velocity field at the DPF's outlet in the $x_1 - x_2$ plane using Mesh 1 for Case 3.

Figure A.11 presents the pressure field at the DPF's inlet in the $x_1 - x_2$ plane using Mesh 1 for Case 3.

Figure A.12 presents the pressure field at the DPF's outlet in the $x_1 - x_2$ plane using Mesh 1 for Case 3.

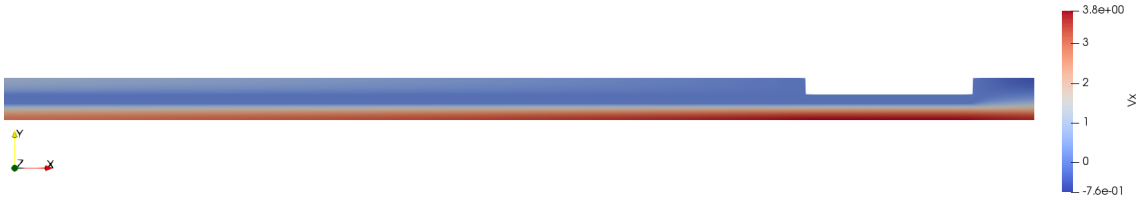

Figure A.6: Horizontal velocity at DPF's outlet in Case 2 using quadratic mesh.

Figure A.7: Pressure at DPF's inlet in Case 2 using quadratic mesh.

Figure A.8: Pressure at DPF's outlet in Case 2 using quadratic mesh.

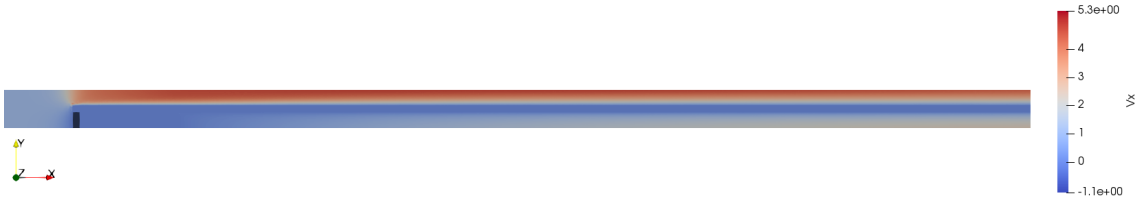

Figure A.9: Horizontal Velocity at DPF's inlet in Case 3 obtained with Mesh 1.

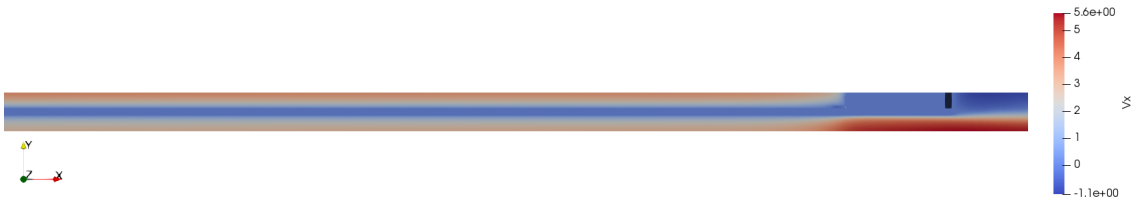

Figure A.10: Horizontal Velocity at DPF's outlet in Case 3 obtained with Mesh 1.

Figure A.11: Pressure at DPF's inlet in Case 3 obtained with Mesh 1.

Figure A.12: Pressure at DPF's outlet in Case 3 obtained with Mesh 1.

Figure A.13 presents the horizontal velocity field at the DPF's inlet in the $x_1 - x_2$ plane using Mesh 2 for Case 3.

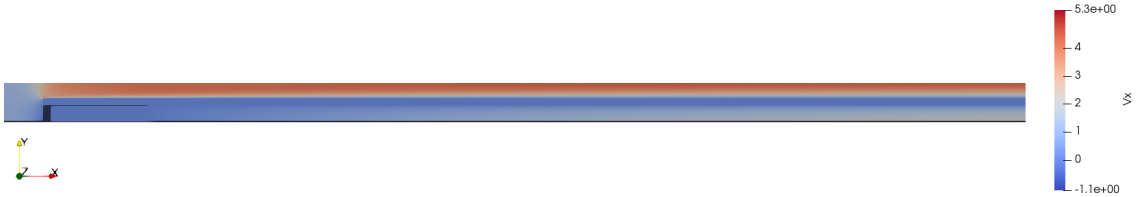

Figure A.13: Horizontal Velocity at DPF's inlet in Case 3 obtained with Mesh 2.

Figure A.14 presents the horizontal velocity field at the DPF's outlet in the $x_1 - x_2$ plane using Mesh 2 for Case 3.

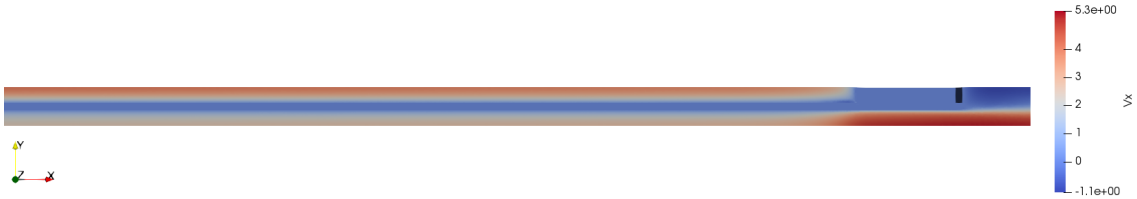

Figure A.14: Horizontal Velocity at DPF's outlet in Case 3 obtained with Mesh 2.

Figure A.15 presents the pressure field at the DPF's inlet in the $x_1 - x_2$ plane using Mesh 2 for Case 3.

Figure A.16 presents the pressure field at the DPF's outlet in the $x_1 - x_2$ plane using Mesh 2 for Case 3.

Figure A.17 presents the horizontal velocity field at the DPF in the $x_1 - x_2$ plane using Mesh 1 for Case 4.

Figure A.18 presents the pressure field at the DPF in the $x_1 - x_2$ plane using Mesh 1 for Case 4.

Figure A.19 presents the horizontal velocity field at the DPF in the $x_1 - x_2$ plane using Mesh 2 for Case 4.

Figure A.20 presents the pressure field at the DPF in the $x_1 - x_2$ plane using Mesh 2 for Case 4.

Figure A.15: Pressure at DPF's inlet in Case 3 obtained with Mesh 2.

Figure A.16: Pressure at DPF's outlet in Case 3 obtained with Mesh 2.

Figure A.17: Horizontal Velocity at DPF in Case 4 obtained with Mesh 1.

Figure A.18: Pressure at DPF in Case 4 obtained with Mesh 1.

Figure A.19: Horizontal Velocity at DPF in Case 4 obtained with Mesh 2.

Figure A.20: Pressure at DPF in Case 4 obtained with Mesh 2.